

ELECTRONIC STRUCTURE AND CHARGE DENSITY WAVES
IN THE RARE EARTH (R) TELLURIDES $R\text{Te}_2$ AND $R_2\text{Te}_5$

A DISSERTATION

SUBMITTED TO THE DEPARTMENT OF APPLIED PHYSICS
AND THE COMMITTEE ON GRADUATE STUDIES

OF STANFORD UNIVERSITY

IN PARTIAL FULFILLMENT OF THE REQUIREMENTS

FOR THE DEGREE OF

DOCTOR OF PHILOSOPHY

Kyungyun Shin

September 2008

© Copyright by Kyungyun Shin 2009

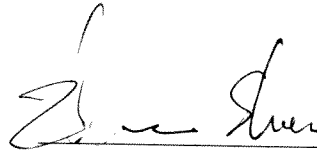
All Rights Reserved

I certify that I have read this dissertation and that, in my opinion, it is fully adequate in scope and quality as a dissertation for the degree of Doctor of Philosophy.



(Ian R. Fisher) Principal Adviser

I certify that I have read this dissertation and that, in my opinion, it is fully adequate in scope and quality as a dissertation for the degree of Doctor of Philosophy.



(Zhi-Xun Shen)

I certify that I have read this dissertation and that, in my opinion, it is fully adequate in scope and quality as a dissertation for the degree of Doctor of Philosophy.



(Martin Greven)

Approved for the University Committee on Graduate Studies.

Abstract

Rare earth (R) telluride compounds have attracted recent attention due to their effective low dimensionality. $R\text{Te}_n$ ($n=2, 2.5, 3$) play host to a charge density wave (CDW) and can be described in terms of a nominally tetragonal structure based on alternating layers of square-planar Te sheets and a corrugated $R\text{Te}$ slab (R =Rare Earth). Band structure calculations for the material indicate a strongly anisotropic two dimensional Fermi surface (FS) of mostly Te $5p$ character with minimal dispersion perpendicular to the Te planes, and a superlattice modulation of the average structure has been observed, which can be understood in terms of optimal nesting of a Fermi surface derived from simple tight-binding arguments. These observations essentially establish the lattice modulation in these materials as a charge density wave (CDW), driven by an electronic instability of the Fermi surface. The structural and electronic simplicity, combined with the large size of the CDW gap, makes these materials particularly attractive for studying CDW formation and its effect on the electronic and crystal structure.

In this study, the results of TEM, high resolution X-ray Diffraction, heat capacity and resistivity measurements of single crystals of two specific families of layered rare earth tellurides, $R\text{Te}_2$ (R =La and Ce) and $R_2\text{Te}_5$ (R =Nd, Sm and Gd) are reported. We have prepared high quality samples in single crystal form using an alternative

self-flux technique, which lends itself to minimizing the risk of contamination by not using a separate flux or transport agent. The CDW in $R_2\text{Te}_5$ ($R=\text{Nd}$, Sm and Gd) was first observed in this study and the measurements provide complementary information about the competing CDW order parameters formed in different Te layers in the crystal. Each of the materials exhibits a complex mixture of incommensurate and commensurate CDW vectors and the origin of the observations are discussed in terms of the electronic structure and the susceptibility. Our results indicate that subtle differences, such as the choice of rare earth and band filling, can substantially affect the superlattice modulation and electronic structure.

Acknowledgement

My research experience in the Fisher group has been full of excitement and I would like to express my sincere gratitude to people for helping me during my graduate study.

I would especially like to thank my adviser, Ian Fisher, for his being supportive all the time. Ian has been a great adviser with enthusiasm throughout my doctoral work and encouraged me to find ways to enjoy every aspect of research activities.

I am also very grateful to every member of the Fisher group for sharing wonderful lab experiences. Yana has been a labmate sitting next to me for years and I thank for her instrumental expertise and experimental insights. It was always a great pleasure to have a conversation with her about various topics. Suchitra has been a person full of great ideas about both scientific and non-scientific activities. Nancy was a scientist with whom I was able to share all the research ideas on CDW materials. Experiments with her at beam lines were an essential part of my research experience in this hard science. Ann, thankfully, always took the initiative in taking care of lab practices and keeping the lab standard high. It was very nice to share lab life with Eric, who has an exceptional understanding of Korean culture. Jiun-Haw inspired me with new interesting experimental results on the CDW materials.

I wish to thank Dr. Mike Toney and Dr. Cathie Condrón at the Stanford Synchrotron Radiation Laboratory for the advice and the kindness. Mike guided me through all the experiments at beam lines with a great scientific enthusiasm and showed me what a senior scientist can be. Cathie never hesitated to share research interests and difficulties as a young scientist. With Nancy, all four of us had a great time during tedious but rewarding research experiments at the SSRL. The identification of interesting properties of CDWs in rare earth tellurides was made possible only with their helps.

It was a great excitement to collaborate with good people all over the places. I would like to express my deep gratitude to Dr. Veronique Brouet and Ruihua He from the Shen Group. It was always exciting to converse with Dr. Brouet and the early discussion with her was a great motivation for me to study charge density waves in rare earth telluride compounds. I had a good time with Ruihua working on ARPES data and preparing APS March meeting together. I thank Dr. Jude Laverock and Prof. Stephen Dugdale for their great work and generous discussions. Hong Yao from the Kivelson group was always there for casual discussions on the theoretical aspects of CDW and it was greatly helpful. My last part of research was greatly assisted by Dr. Wu and Prof. Kramer at the Ames Laboratory. I really enjoyed and appreciate for their beautiful TEM works. I wish to thank Prof. Z.-X Shen, Prof. Martin Greven, Prof. Steve Kivelson and Prof. Ted Geballe for being on my thesis committee.

Corrina, Mark, Larry, Lily and other GLAM community members made GLAM a second home to me filled with warm kindness. TEM techniques I learned from Ann Marshall were essential for my studies and Arturas assisted numerous X-ray measurements. Thanks to Paula and Claire, I was able to come down this long road

since my first arrival at Stanford. I still remember their warm hearted welcome and appreciate for their consistent cares.

I extend many thanks to my friends for sharing good and hard times at Stanford. Culture nights with Arito and Wei, trips with Paul, Yangjin and Hopil, and all other activities with good friends made my life much richer than I ever expected.

Finally, none of this would have been possible without support of my family. My parents were a constant source of enthusiasm and encouragement and I would like to express my warm hearted gratitude to them. I'm also very grateful to my parents-in-laws for their concern and support. Most importantly, I'd like to thank my wife, Jae Yoen for understanding and being always supportive, and my son, Ryan for filling my life with love and joy.

Contents

Abstract	v
Acknowledgement	vii
1 Introduction	1
1.1 Charge Density Waves	3
1.1.1 CDW phase transition	3
1.1.2 Fermi surface nesting structure in CDW	6
1.1.3 CDW T dependence	10
1.1.4 Phonon mode softening and energy instability	11
1.2 CDW Stability	18
2 Rare Earth Tellurides	21
2.1 Crystal Structure	21
2.2 Electronic Structure	25
2.2.1 Simple Tight Binding Model	25
2.2.2 LMTO Band Structure Calculation	29
2.3 $R\text{Te}_3$	34
2.3.1 CDW Superlattice and Electronic structure	34

2.3.2	Temperature Dependence of the CDW	38
2.3.3	Pressure Effects on $R\text{Te}_3$	43
2.4	$R\text{Te}_2$	44
2.5	$R_2\text{Te}_5$	45
3	Experimental Methods	48
3.1	Single Crystal Sample Preparation	48
3.1.1	Crystal Growth: $R\text{Te}_2$	49
3.1.2	Crystal Growth: $R_2\text{Te}_5$	53
3.2	Transmission Electron Microscopy	55
3.3	High Resolution X-ray Diffraction	57
3.4	Thermodynamic and Transport Properties	57
4	Charge Density Waves in $R\text{Te}_2$ ($R=\text{La, Ce}$)	59
4.1	Introduction	59
4.2	Experimental Results	63
4.2.1	Transmission Electron Microscopy	63
4.2.2	ARPES	68
4.2.3	Heat Capacity	74
4.2.4	Resistivity	76
4.3	Discussion	79
4.4	Conclusion	81
5	Charge Density Waves in $R_2\text{Te}_5$ ($R=\text{Nd, Sm, Gd}$)	83
5.1	Introduction	84
5.2	Experimental Results: TEM	85
5.3	Discussion	90

5.3.1	Electron-Phonon Coupling, Lindhard susceptibility and CDW Formation	90
5.3.2	Origin of the <i>On-axis</i> Lattice Modulation	94
5.3.3	Origin of the <i>Off-axis</i> Lattice Modulation	96
5.4	Conclusion	101
6	Multiple charge density wave transitions in Gd_2Te_5	102
6.1	Introduction	102
6.2	Experimental Results	103
6.2.1	Transmission Electron Microscopy at High Temperatures . . .	103
6.2.2	High Resolution X-ray Diffraction at High Temperatures . . .	107
6.3	Discussion	111
6.4	Conclusion	114
7	Conclusion	115
A	Magnetic properties of $R_2\text{Te}_5$	119
B	Transport property of $R_2\text{Te}_5$	124
C	X-ray Diffraction for Gd_2Te_5 at room temperature	127
	Bibliography	131

Chapter 1

Introduction

The charge density wave (CDW) is a ground state with spontaneously broken translational symmetry, specific to anisotropic low dimensional materials. The phase transition to the CDW ground state is accompanied by the development of commensurate/incommensurate periodic lattice distortions and the opening of energy gaps (order parameter) at the Fermi level. While competing with the thermal and quantum fluctuations intrinsic to low dimensional electron systems, such tendency to symmetry breaking is strongly enhanced by Fermi surface (FS) nesting, and the delicate interplay of the electron-phonon couplings [1]. Since FS nesting plays an essential role, extensive experimental efforts have been made in order to affect the FS topology and tune the CDWs in various materials by, for example, chemically doping the hosting materials [2] and applying pressure [3–5].

Low dimensional materials typically have a crystal structure with rigid bonds only either along one direction or in a plane, which provide easy conduction channels for electrons and result in a strong anisotropic electronic structure. Such materials include NbSe_3 , $\text{K}_{0.3}\text{MoO}_3$, $(\text{TaSe}_4)_2\text{I}$ and KCP or $\text{K}_2\text{Pt}(\text{CN})_4\text{Br}_{0.3}\cdot 3.2\text{H}_2\text{O}$, which have

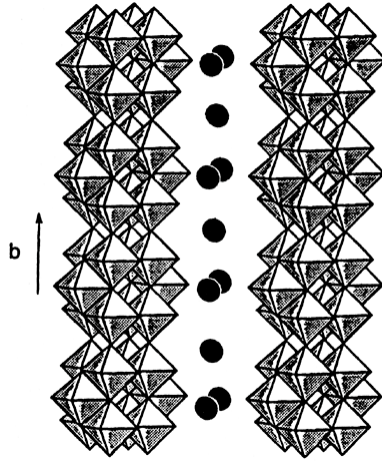


Figure 1.1: The chain structure of $K_{0.3}MoO_3$. Figure from reference [1].

a chain structure [6–10]. For example, $K_{0.3}MoO_3$ in Figure 1.1 has a one dimensional chain structure with the units of MoO_3 octahedra, rigidly sharing corners along the long b axis direction and it forms an easy conduction channel for the electrons donated by the alkaline ions. The material undergoes a CDW phase transition at 180K with an incommensurate lattice distortion along the one dimensional chain direction and various experimental investigations have been performed [8, 10, 11].

Compared to the one dimensional materials, CDW states in two dimensional systems are particularly interesting, partly because of the novel effects coming from the multiple possible nesting wave vectors and competing order parameters added by the extra dimensionality. In this thesis, I describe the results of experiments probing CDW formation in two closely related families of quasi 2D materials: RTe_2 and R_2Te_5 , where R is a rare earth element. These results appear in Ref. [12] and Refs. [13, 14]. Additional collaborative works not described in this thesis appear in Refs. [5, 15–18].

1.1 Charge Density Waves

In physical systems, there are two forms of energetically equilibrium states, either a stable equilibrium state such as a ball at the bottom of a bowl or an unstable equilibrium state such as a ball on top of a dome. Usually, the stable equilibrium state is robust and remains so up to small fluctuations, while the unstable equilibrium state is very sensitive to external or internal perturbations. In many circumstances, a stable ground state becomes unstable by various changes in the physical conditions and, then, the physical system tries to find a totally new stable state - the transition from a normal state to CDW state is a good example.

1.1.1 CDW phase transition

The charge density wave(CDW) instability of a one dimensional electron gas was first proposed by Fröhlich in 1954 [19] and by Peierls in 1955 [20], and has been experimentally witnessed in various forms of (quasi-)one dimensional materials since then [1]. One dimensional materials are characterized by strongly anisotropic electronic structure. The sections of Fermi surfaces(FSSs) are parallel to each other and provide an optimal condition for nesting to induce electron energy instability and hence a phase transition to a novel ground state - the charge density wave (CDW) state.

Within the framework of linear response theory, the perturbed electric potentials induce electron charge redistribution. The rearrangement of electronic charge is described by the following linear approximation,

$$\phi(\vec{r}) = \int_q \phi(\vec{q}) e^{i\vec{q}\cdot\vec{r}} d\vec{q}, \quad \rho^{ind}(\vec{r}) = \int_q \rho(\vec{q})^{ind} e^{i\vec{q}\cdot\vec{r}} d\vec{q},$$

$$\rho^{ind}(\vec{q}) = \chi(\vec{q})\phi(\vec{q}), \quad (1.1)$$

where $\phi(\vec{q})$ and $\rho^{ind}(\vec{r})$ refer to a perturbed potential and the induced (electron) charge density respectively. The linear response function $\chi(\vec{q})$ in Equation 1.1 is called the Lindhard susceptibility and is defined by

$$\chi(\vec{q}) = -\frac{1}{(2\pi)^d} \int_{1BZ} d\vec{k} \frac{f(\vec{k} + \vec{q}) - f(\vec{k})}{\epsilon_{\vec{k}+\vec{q}} - \epsilon_{\vec{k}}}, \quad (1.2)$$

where $f(\vec{k})$ represents the Fermi function ¹ and $\epsilon_{\vec{k}}$ denotes the free electron energy at the momentum \vec{k} . The electron charge redistribution, in return, generates additional perturbations to the electric potential. Both of the induced potentials and charge density redistributions should meet the following self-consistent relations through Poisson's equation

$$\phi^{ind}(\vec{q}) = -g'\rho^{ind}(\vec{q}). \quad (1.3)$$

The equilibrium condition from Equation 1.1 and Equation 1.3 gives

$$\phi(\vec{q}) = \phi^{ext}(\vec{q}) + \phi^{ind}(\vec{q}), \quad (1.4)$$

$$\rho^{ind}(\vec{q}) = \chi(\vec{q})(\phi^{ext}(\vec{q}) + \phi^{ind}(\vec{q})), \quad (1.5)$$

$$\rho^{ind}(\vec{q}) = \frac{\chi(\vec{q})\phi^{ext}(\vec{q})}{1 + g'\chi(\vec{q})}. \quad (1.6)$$

¹The Fermi function has the values $f(\vec{k})=1$ for electrons and $f(\vec{k})=0$ for holes at T=0K

An important instability condition based on the free electron model was derived in Equation 1.6 for $g' < 0$. When the electrons are strongly coupled to the potential with a large coupling constant $|g'|$, the instability condition becomes $1 + g'\chi(\vec{q}) = 0$ for enhanced $\chi(\vec{q})$ maximum and the induced charge distribution diverges (Equation 1.6). In such a case, the self-consistent linear response approximation breaks down and a phase transition to a new ground state occurs. As such, the CDW phase transition depends on the enhancement structure in $\chi(\vec{q})$, from which it is possible to build more insights on this new ground state.

The Fermi function $f(\vec{k})$ in the definition of the Lindhard susceptibility in Equation 1.2 indicates that only ‘electron-hole’ pairs at \vec{k} and $\vec{k}+\vec{q}$ contribute to the development of the CDW states, since $f(\vec{k} + \vec{q}) - f(\vec{k}) \neq 0$ only for $(f(\vec{k} + \vec{q}), f(\vec{k})) = (1,0)$ and $(0,1)$. This is in contrast to BCS superconductivity, which is induced by the electron-electron pairs. The peak structure of $\chi(\vec{q})$ tends to be more closely associated with ‘selected’ \vec{q} vectors that give the smallest denominator, $\epsilon_{\vec{k}+\vec{q}} - \epsilon_{\vec{k}} \approx 0$ or $\epsilon_{\vec{k}+\vec{q}} \approx \epsilon_{\vec{k}}$ (Figure 1.2), over ‘larger regions’ in \vec{k} space available for the integration. The electron-hole pairs (e - h pairs) nested by such a wavevector \vec{q} have a relatively high density of states at the Fermi level and the CDW phase transition is dominated by the energy states close to the Fermi energy, E_F . Thus, since the contribution from the actual *number of the e - h pair states* at E_F becomes important in the integration in Equation 1.2 for optimal nesting, $\chi(\vec{q})$ peak structures strongly depend on the topology of the FS of the hosting materials. As it will be discussed in later sections, anisotropic low dimensional materials have more regions of FS parallel to each other, which give more density of states available for nesting, and are more strongly susceptible to the electron energy instability and CDW phase transition. This often allows a simple graphical interpretation of Fermi surface(FS) nesting as the origin of the

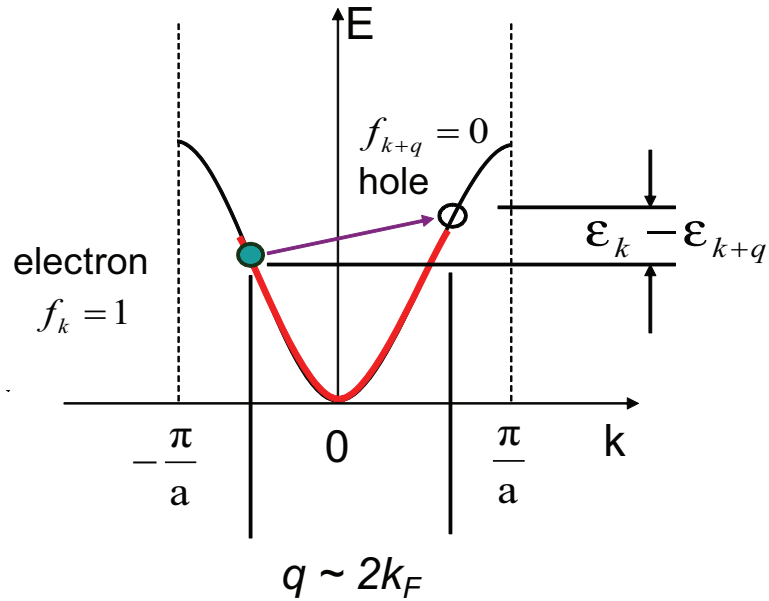


Figure 1.2: Electron-hole pairing.

CDW and, thus, the CDW instability is driven by the electronic structure and the FS topology. Indeed, FS nesting has provided a powerful tool to understand various examples of the CDW states observed in many low dimensional materials for many years [21, 22].

1.1.2 Fermi surface nesting structure in CDW

The e - h pair nesting structures for free electron gases in different conditions are depicted in simplified diagrams in Figure 1.2 and Figure 1.3. A well defined single wavevector at $q = 2k_F$ characterizes the CDW state of the 1D electron gas, ideally nesting the entire regions of FS (Figure 1.3 (a)). In contrast, the 2D or 3D free electron gas does not have such an ideal nesting vector (Figure 1.3 (b) and (c)). Meanwhile, the warped FS depicted in Figure 1.3 (d) shows how the FS nesting can deviate from the ideal nesting, as the topology of the FS changes (the wavevector \vec{q}

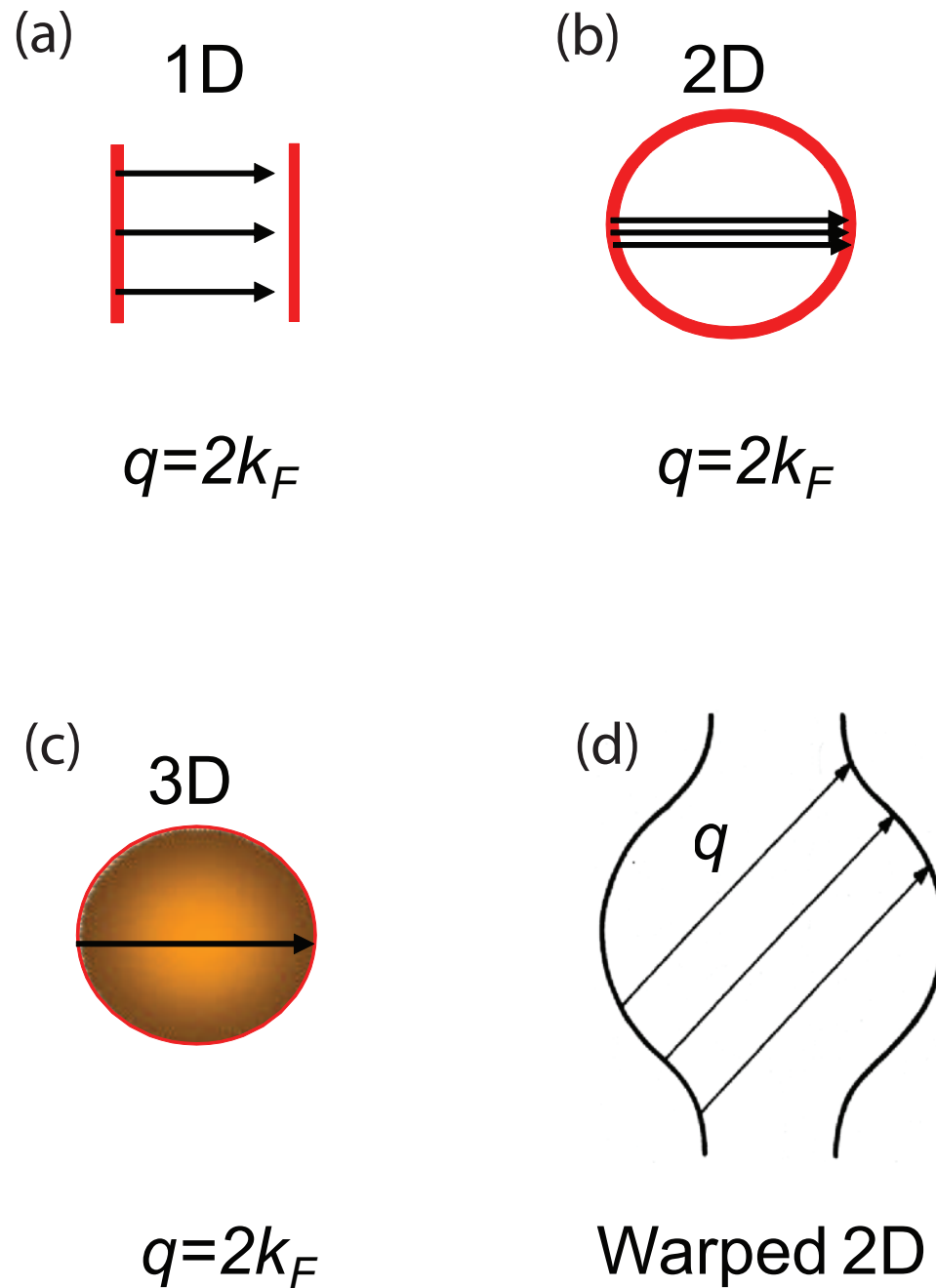


Figure 1.3: FS nesting in (a)1D, (b)2D, (c)3D and (d)warped 1D FS. Figure (d) from reference [1].

$\chi(\vec{q})$ in 1D	$\chi(\vec{q}) = e^2 n(\epsilon_F) \ln \left \frac{q+2k_F}{q-2k_F} \right $
$\chi(\vec{q})$ in 2D	$\chi(\vec{q}) = e^2 n(\epsilon_F) \text{ for } q < 2k_F,$ $\chi(\vec{q}) = e^2 n(\epsilon_F) \left[1 - \sqrt{1 - \left(\frac{2k_F}{q} \right)^2} \right] \text{ for } q \geq 2k_F$
$\chi(\vec{q})$ in 3D	$\chi(\vec{q}) = -e^2 n(\epsilon_F) \left[1 + \frac{1-x^2}{2x} \ln \left \frac{1+x}{1-x} \right \right]$

Table 1.1: $\chi(\vec{q})$ in 1D, 2D and 3D band structures. $x = q/2k_F$. A linearized dispersion relation $\epsilon = \epsilon_F \pm v_F(k - k_F)$ was used for the 1D free electron gas for computational simplicity [1, 23].

now lies off the k_x direction, but still nests the FS extremum, keeping the maximal e - h pair density available for nesting). The number of nested e - h pairs can actually be considered as a measure of FS nesting in a heuristic sense. In terms of the degree of nesting, the warped FS is somewhere between the case of the ideal 1D and the 2D electron gases, and is likely to be more susceptible to the phase transition than is the ideal the 2D free electron gas.

The explicit $\chi(\vec{q})$ formula calculated for free electrons in one (1D), two (2D) and three (3D) dimensions at T=0K are shown in Table 1.1. The graphs in Figure 1.4 give good guides to the examples, revealing qualitative characteristics of $\chi(\vec{q})$ functions in different dimensions and nesting conditions. The computational difficulties caused by the singularity structures due to the FS nesting, for example, in $\chi(\vec{q})^{2D}$, can be handled by using dynamic structure functions and real and imaginary parts of the dynamic susceptibilities in the w - k plane [23]. The 1D free electron gas develops a

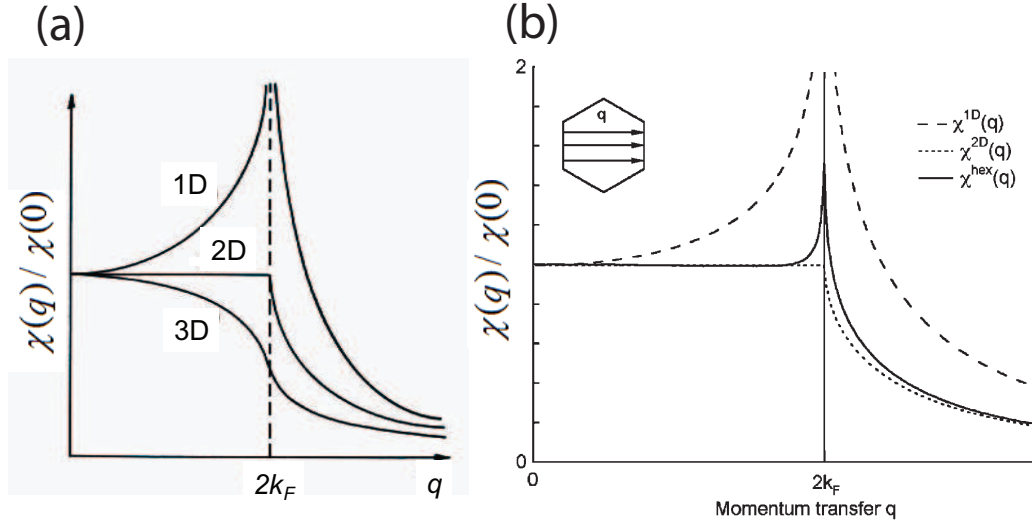


Figure 1.4: (a) Lindhard susceptibility for one, two and three dimensional free electrons, from reference [1]. (b) Numerical calculation of the Lindhard susceptibility for a hexagonal FS, appropriate for elemental Bi [24]. $\epsilon^{\text{hex}}(\vec{k}) \propto k^2 \cos \left[\left| \varphi - \text{Int} \left(\varphi / \frac{\pi}{3} \right) \frac{\pi}{3} \right| - \frac{\pi}{6} \right]$, from reference [24].

logarithmic divergence singularity at $q = 2k_F$, as expected from the high degree of the nesting, while $\chi(\vec{q})$ for 2D and 3D free electrons does not have such a divergent structure, besides the singularities in the first order derivatives at $q = 2k_F$ (Figure 1.4). Pure 2D and 3D free electron systems, therefore, do not suffer from CDW instabilities. The degree of divergence in $\chi(\vec{q})$ is determined by the curvature of the nested FS and the 2D free electron gas can to some extent be considered as being on the edge of the $\chi(\vec{q})$ peak development. An example of the enhanced nesting by changing the 2D FS topology can be given by the hexagonal FS, describing the known CDW in Bi(111) [24]. As in Figure 1.4 (b), the hexagonal FS has more flat regions available for the optimal nesting and, thus, $\chi(\vec{q})^{\text{hex}}$ has a divergent peak structure at $q = 2k_F$, which is weaker in intensity than $\chi(\vec{q})^{1D}$, but still quite considerable. $\chi(\vec{q})^{\text{hex}}$ also converges to $\chi(\vec{q})^{2D}$ for $q \ll 2k_F$ and $q \gg 2k_F$ and the hexagonal electronic

structure is, indeed, in between the 1D and 2D free electrons.

1.1.3 CDW T dependence

The finite temperature dependence of $\chi(\vec{q})$ can be obtained by calculating the grand canonical ensemble of the structure function as in Ref. [23] or, equivalently, using the Fermi function for $T \neq 0$ in Equation 1.2 and, therefore, Equation 1.7.

$$\chi(\vec{q} = 2k_F, T) = -e^2 n(\epsilon_F) \int_0^{\epsilon_0/2k_B T} \frac{\tanh x}{x} dx, \quad (1.7)$$

where $x = \frac{\epsilon}{2k_B T}$ and ϵ_0 is an cutoff energy of the integration, typically in the order of Fermi energy. A straight forward calculation gives $\chi(q = 2k_F, T)$ at the peak for 1D free electrons (Equation 1.8), which shows that the peak is logarithmically divergent as $T \rightarrow 0$.

$$\chi(q = 2k_F, T) = -e^2 n(\epsilon_F) \ln \left| \frac{1.14\epsilon_0}{k_B T} \right| \quad (1.8)$$

Since the peak diverges for low enough temperatures, the ideal 1D free electrons are always susceptible to the CDW phase transition at T_{MF} , even with a very small coupling constant $|g'|$, by the instability condition $1 + g'\chi(\vec{q} = 2k_F, T_{MF}) = 0$. It gives a BCS-like mean field CDW transition temperature T_{MF} defined in Equation 1.9.

$$k_B T_{MF} = 1.14\epsilon_0 \exp \left(-\frac{1}{g'n(\epsilon_F)} \right) \quad (1.9)$$

The transition temperature T_{MF} is proportional to the energy scale ϵ_0 close to the Fermi energy $E_F \sim 10^5$ K. Consequently, the mean field CDW transition temperature T_{MF}^{CDW} is much higher in magnitude than the mean field transition temperature of the

CDW material	T ^{CDW} (K)	BCS superconductor	T ^{BCS} (K)
NbSe ₃	145, 59	Zr	0.546
KCP	189	Al	1.2
K _{0.3} MoO ₃	189	In	3.408
TaS ₃	215	Hg	4.153

Table 1.2: Transition temperatures observed in CDW materials and BCS superconductors.

BCS superconductors, which is proportional to the phonon mode cut-off energy $k_B\theta \sim 200\text{-}500\text{K}$. The observed CDW transition temperature T^{CDW} s are indeed typically much greater than T^{BCS} but by a factor of 10-30, rather than a factor of 1000. This is due to the suppression of the CDW transition by fluctuations, which have particularly dominant effects in low dimensional systems [17].

Examples of the observed transition temperatures for several CDW materials and BCS superconductors are listed in Table 1.2.

1.1.4 Phonon mode softening and energy instability

CDW transitions driven by the electronic structure are accompanied by order parameter developments and other various changes in the hosting materials, such as periodic lattice distortion or phonon mode softening. The interaction between electrons and phonons in CDW materials is described by the second quantized Hamiltonian proposed by Fröhlich [19], as given in Equation 1.10

$$\begin{aligned}
 H &= \sum_k \epsilon_k a_k^\dagger a_k + \sum_k \hbar\omega_q b_k^\dagger b_k + \sum_{k,q} g_q a_{k+q}^\dagger a_k (b_{-q}^\dagger + b_q), \\
 g_q &= i \left(\frac{\hbar}{2M\omega_q} \right)^{\frac{1}{2}} |q|V_q,
 \end{aligned} \tag{1.10}$$

where a_k^\dagger and b_q^\dagger are electron and phonon creation operators respectively [1]. g_q is a microscopic electron-phonon coupling constant that depends on the momentum transfer V_q and will be approximated to be independent of q , $g_q \approx g$, for simplicity. The atomic displacement from the equilibrium position is given in terms of the phonon mode creation operators by

$$Q_q = \left(\frac{\hbar}{2M\omega_q} \right)^{\frac{1}{2}} (b_k^\dagger + b_k). \quad (1.11)$$

The ionic potentials are perturbed by phonon modes (i.e. lattice vibrations), and the induced potential, $\phi(q)$, is proportional to Q_q as in the classical sense, giving the following relation

$$\phi(q) = g \left(\frac{2M\omega_q}{\hbar} \right)^{\frac{1}{2}} Q_q. \quad (1.12)$$

The phonon modes in the crystal, therefore, directly explain the ionic potential fluctuations and affect the electron density fluctuations through Equation 1.1. The dynamics of the lattice vibrations for small amplitudes are straightforwardly described by

$$\hbar^2 \ddot{Q}_q = -[[Q_q, H], H], \quad (1.13)$$

giving the effective phonon mode equation,

$$\ddot{Q}_q \approx -\omega_q^2 Q_q - g \left(\frac{2\omega_q}{M\hbar} \right)^{1/2} \rho_q. \quad (1.14)$$

The electron movements also dress the ionic motion, as all the constituent entities in a quantum many body system mutually interact with each other. The second term in Equation 1.14 can be ascribed to the renormalization of the ionic motion by electrons. The induced ionic potentials, then, can be considered to originate from the self-consistent linear response to the electron charge density fluctuations, $\rho_q = \sum_k a_k^\dagger a_k$. The second quantized linear response of the charge fluctuation reads

$$\rho_q = \chi(q, T)\phi(q) = \chi(q, T)g \left(\frac{2M\omega_q}{\hbar} \right)^{\frac{1}{2}} Q_q. \quad (1.15)$$

The equation of motion for the dressed phonon modes then becomes

$$\ddot{Q}_q = - \left(\omega_q^2 - \frac{2g^2\omega_q}{M\hbar} \chi(q, T) \right) Q_q, \quad (1.16)$$

giving the renormalized dispersion relation,

$$\omega_{ren}^2(q) = \omega_q^2 - \frac{2g^2\omega_q}{M\hbar} \chi(q, T). \quad (1.17)$$

The renormalized dispersion relation clearly shows that the electronic property $\chi(\vec{q})$ affects the ionic motion and the interaction slows down the phonon mode oscillation frequency, which is somewhat analogous to the effect of a viscous fluid on the motion of an object.

The Lindhard susceptibility $\chi(q, T)$ for 1D electrons has a divergent maximum for decreasing temperatures, and Equation 1.17 implies that the ionic motion actually

freezes at $q = 2k_F$ when $T = T_{\text{MF}}$, such that $\chi(2k_F, T_{\text{MF}}) = e^2 n(\epsilon_F) \ln \left| \frac{1.14\epsilon_0}{k_B T_{\text{MF}}} \right|$,

$$\begin{aligned} \omega_{ren}^2(2k_F) &= \omega_{2k_F}^2 - \frac{2g^2\omega_{2k_F}}{M\hbar} \chi(2k_F, T_{\text{MF}}) \\ &= \omega_{2k_F}^2 - \frac{2g^2\omega_{2k_F}}{M\hbar} \left[e^2 n(\epsilon_F) \ln \left| \frac{1.14\epsilon_0}{k_B T_{\text{MF}}} \right| \right] = 0, \end{aligned} \quad (1.18)$$

The phonon mode freezing condition determines the microscopic mean field transition temperature

$$k_B T_{\text{MF}} = 1.14\epsilon_0 \exp(-1/\lambda), \quad (1.19)$$

where $\lambda = \frac{g^2 n(\epsilon_F)}{M\hbar\omega_{2k_F}}$, and the CDW transition accompanies the broken-translational symmetry with the ‘frozen’ phonon modes or the periodic lattice distortions at $q = 2k_F$.²

The phonon mode renormalization by the electron charge fluctuations is stronger in 1D electronic structure and, yet, there are still significant renormalization effects in some 2D electron systems, where electron density fluctuations develop strongly enhanced maximum peaks in $\chi^{2D}(\vec{q})$ by nesting considerable amounts of sections of 2D FS, as, for example, the hexagonal FS shown in Figure 1.4 (b). The new superlattice periodicity $q = 2k_F$ is purely determined by the ‘electronic structure’ and it can be commensurate or incommensurate to the underlying crystal lattice, depending on the topology of the FS.

²It is interesting to compare the microscopic coupling constant g with g' in the Poisson’s condition (Equation 1.3) using the derived mean field transition temperatures T_{MF} in Equations 1.9 and 1.19. The relation between the two coupling constants is given by

$$g' = \frac{g^2}{M\hbar\omega_{2k_F}},$$

and it relates the semiclassical and the microscopic quantum mechanical parameters.

Meanwhile, the new electron ground states can be accessed by diagonalizing the Fröhlich Hamiltonian in Equation 1.10 utilizing the mean field approximation and Bogoliubov transformation, like in the BCS theory. The new CDW ground state is defined in this mean field approximation by

$$\begin{aligned}
|\phi_0\rangle &= \left(\prod_{|k| < k_F} \gamma_{1,k}^\dagger \gamma_{2,k}^\dagger \right) |0\rangle, \\
\gamma_{1,k} &= U_k a_{1,k} - V_k^* a_{2,k}, \\
\gamma_{2,k} &= V_k a_{1,k} + U_k^* a_{2,k}, \\
|U|^2 + |V|^2 &= 1,
\end{aligned} \tag{1.20}$$

where $|0\rangle$ refers to the vacuum state and $a_{1,k}^\dagger$ and $a_{2,k}^\dagger$ represent the electron creation operators on each side of the nested FS sections respectively. $\gamma_{1,k}^\dagger$ and $\gamma_{2,k}^\dagger$ are single particle excitation operators, similar to BCS theory, and the diagonalized mean field Hamiltonian for the new CDW ground state is then given by

$$\begin{aligned}
H &= \sum_k \epsilon_k a_k^\dagger a_k + \sum_k \hbar\omega_q \langle b_k^\dagger b_k \rangle + \sum_{k,q} g_q a_{k+q}^\dagger a_k \langle b_{-q}^\dagger + b_q \rangle \\
&= \sum_k E_k \left(\gamma_{1,k}^\dagger \gamma_{1,k} + \gamma_{2,k}^\dagger \gamma_{2,k} \right) + \frac{\hbar\omega_{2k_F} \Delta^2}{2g^2},
\end{aligned} \tag{1.21}$$

$$E_k = \epsilon_k + \text{sign}(k - k_F) \left[\hbar^2 v_F^2 (k - k_F)^2 + |\Delta|^2 \right]^{1/2}, \tag{1.22}$$

$$\Delta = g \left(\langle b_{2k_F} \rangle + \langle b_{-2k_F}^\dagger \rangle \right). \tag{1.23}$$

It is indicated by Equation 1.22 that the electron density of states has disappeared

in the CDW ground state and there is a single particle excitation energy gap $|\Delta|$ opened at the Fermi level, $\epsilon = \epsilon_F$. The 1D CDW materials become an insulator upon the transition by the gap opening, while the 2D CDW materials remain metallic down to T=0K due to the ungapped remaining FS [11,25]. The gap opening lowers energies of the filled electron states below the Fermi level, providing electron energy gain and hence a driving force for the phase transition from the normal state to the CDW state. The electron energy gain by the energy gap is obtained from Equation 1.22 to be

$$E_{el} = \frac{n(\epsilon_F)}{2} \left\{ \epsilon_F^2 - \left[\epsilon_F(\epsilon_F^2 + \Delta^2)^{1/2} + \Delta^2 \log \frac{\epsilon_F + (\epsilon_F^2 - \Delta^2)^{1/2}}{\Delta} \right] \right\}, \quad (1.24)$$

which should be larger than the potential energy increase by the lattice distortion at the onset of the CDW transition.³

The charge density modulation can be obtained by calculating the expectation value of the electron density field operator $\Psi(x) = \sum_k (a_{1,k} e^{ik_F x} + a_{2,k} e^{-ik_F x})$ with respect to the CDW ground state, and it is given by

$$\begin{aligned} \rho(x) &= \langle \phi_0 | \Psi^\dagger(x) \Psi(x) | \phi_0 \rangle \\ &= \rho_0 \left[1 + \frac{\Delta}{\hbar v_F k_F \lambda} \cos(2k_F x + \phi) \right]. \end{aligned} \quad (1.25)$$

³The lattice distortion amplitude is

$$\begin{aligned} \langle u(x) \rangle &= \left(\frac{\hbar}{2NM\omega_{2k_F}} \right)^{1/2} \left\{ i(\langle b_{2k_F} \rangle + \langle b_{-2k_F}^\dagger \rangle) e^{i2k_F x} + c.c. \right\} \\ &= u_0 \cos(2k_F x + \phi), \quad u_0 = \left(\frac{2\hbar}{2NM\omega_{2k_F}} \right)^{1/2} \frac{|\Delta|}{g}, \end{aligned}$$

and the potential energy increase is given by

$$E_{pot} = \frac{N}{2} M \omega_{2k_F}^2 \langle u(x) \rangle^2 = \frac{\hbar \omega_{2k_F} |\Delta|^2}{2g^2} = \frac{|\Delta|^2 n(\epsilon_F)}{\lambda}.$$

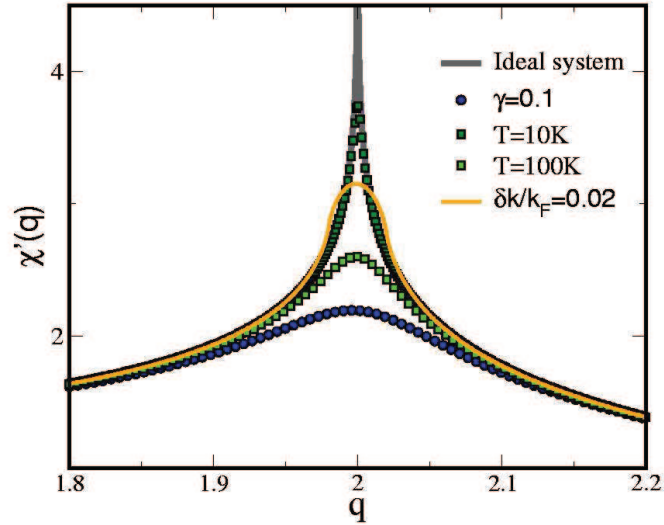


Figure 1.5: A comparison of $\chi(q)$ under ideal 1D conditions with perfect nesting at $T=0$ to $\chi(q)$ under various non-ideal conditions. The divergence at $q = 2k_F$ is reduced to relatively weak height. Figure by Johannes from the reference [26].

The new ground state, indeed, has a charge density modulation with the same periodicity $q = 2k_F$ as the superlattice distortions - the name of ‘charge density wave’ came from this electron charge density modulation.

Since the CDW ground state can be described by Fröhlich Hamiltonian in Equation 1.10 within exactly the same BCS frame work and mathematical tools, the temperature dependence of the CDW gap can be shown to have the same BCS gap equation,

$$\frac{1}{\lambda} = \int_0^{\epsilon_0} \tanh\left(\frac{\epsilon_k}{2k_B T}\right) \frac{d\epsilon_k}{(\epsilon_{2k_F}^2 + |\Delta(T)|^2)} \quad (1.26)$$

and the temperature dependence of the CDW gap or the CDW order parameter, $|\Delta(T)|$, can be numerically evaluated (Figure 1.5).

1.2 CDW Stability

The concept of CDW formation is based on the notion that the enhanced peaks in the Lindhard susceptibility due to the FS nesting results in the CDW transition. There has been an attempt to discuss the stability of the CDW states against thermal broadening, incoherent electron scattering and, particularly, imperfectly nested FS in an ideal 1D electron gas by Johannes *et al.*, extending the arguments to the real 2D systems [26].

On the outset, the effects of the electron scattering and thermal broadening are considered. When the incoherent scattering rate γ of the electrons are considered, the Lindhard susceptibility for the 1D free electrons with a nominally perfect nesting wave vector $q = 2k_F$ is modified to Equation 1.27,

$$\chi(q) = \frac{1}{2q} \ln \left| \frac{\gamma^2 + q^2(q - 2k_F)^2}{\gamma^2 + q^2(q + 2k_F)^2} \right|. \quad (1.27)$$

The logarithmic divergence at $q = 2k_F$ have reduced by the scattering to a simple enhancement of $\chi(2k_F)/\chi(0) \approx \ln \left(1 + \frac{64E_F^2}{\gamma^2} \right) / 4$, which shows an enhancement by a factor of 2-2.5 for typical values of $\gamma=0.1\text{eV}-0.2\text{eV}$. Similar reduction in the peak strength by the thermal broadening, even without the electron scattering, was also estimated to a factor of 4, for typical Fermi energies and transition temperatures, meanwhile the geometric deviation from the perfect nesting by 5%, due to the FS warping, also have a comparable effect (Figure 1.5).

Such a reduction of the $\chi(q)$ peak height, even for the nominally perfect nesting, is inherent in all the real CDW systems and the concurrent lattice modulations should be able to constructively sustain the electron energy gains via self-consistent electron-phonon coupling, in order to make the transition robust. The first principle



Figure 1.6: One dimensional chain of Na ions. CDW occurs only when the transverse distortion is allowed. Figure from the reference [26].

calculation of the real materials, indeed, confirmed this in the same literature [26], where it was shown that NbSe₂ hosts the electron charge modulation only if the lattice distortion follows. Moreover, it was seen by the same calculation on a fictitious model system of a one dimensional Na chain, illustrated in Figure 1.6, that the CDW state is not stable and does not create the expected gap at the Fermi level, when only longitudinal ionic distortion is allowed alone - the CDW has to concur with transverse lattice distortion in the 1D Na ionic chain. It suggests that the CDW state favors not only the nesting wave vectors from the peak in $\chi(q)$ but also the specific phonon modes particularly relevant to these wave vectors, which, in turn, affect the actual realization of the CDW wave vectors in the materials.

The simple graphical interpretation of FS nesting and the calculation of the Lindhard susceptibility $\chi(q)$ have been ascribed to the origin of the CDW transitions and widely used for various materials by many authors [2, 12, 17, 18, 27]. Since it was shown that the CDW state results from the self-consistent interaction between the electronic system and the lattice, such an analysis should not be read alone too much in a predictive sense, and has to be supported by additional information on the lattice distortion structures in the CDW materials in order to identify the cause of the CDW. Nonetheless, it still has to be emphasized that the actual CDW distortions tend to occur at the nesting wave vectors in the range suggested by the peak structures in $\chi(q)$ for a wide range of materials, and it provides a solid ground for further

understanding of the CDW forming mechanism.

Chapter 2

Rare Earth Tellurides

This thesis describes the results of experiments probing CDW formation in two relatively new families of quasi 2D materials based on square-planar Te layers; $R\text{Te}_2$ and $R_2\text{Te}_5$, where R is a rare earth ion. In this chapter, I briefly introduce these materials, including the related compound $R\text{Te}_3$.

2.1 Crystal Structure

The families of layered compounds $R\text{Te}_2$, $R\text{Te}_3$ and $R_2\text{Te}_5$ (R =rare earth elements) have a layered crystal structure based on single or double Te layers, separated by $R\text{Te}$ block layers. Their electronic structure is especially simple, being determined by $5p$ orbitals in the nominally square Te planar layers. It is possible to experimentally tune the properties of the CDW states, and various measurements have been performed. Since the $4f$ levels of the rare earth ions are positioned deep in the energy core, the role of the rare earth ions in CDW formation seems to be minor in CDW formation, only contributing extra electrons to the Te p bands and affecting the lattice parameter via the Lanthanide contraction (“chemical pressure”). However, systematic studies on

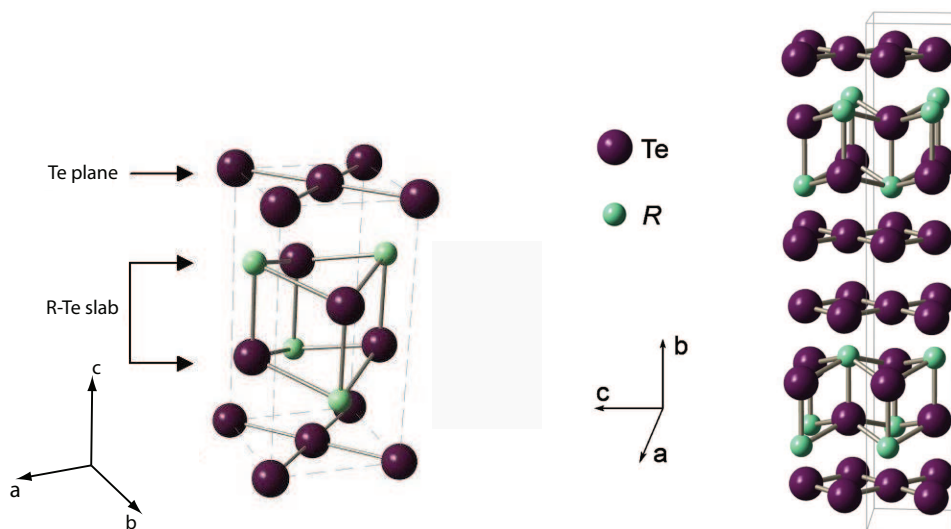


Figure 2.1: (a) The average (unmodulated) crystal structure of $R\text{Te}_2$. Dashed lines show the tetragonal unit cell, in which the c -axis is vertical. (b) The average (unmodulated) crystal structure of $R\text{Te}_3$. Dashed lines show the orthorhombic unit cell, in which the b -axis is vertical. Figure (b) from reference [25].

the rare earth telluride compounds have shown that these effects are not trivial.

$R\text{Te}_2$ has the simplest crystal structure among the rare earth telluride families. Figure 2.1 shows the average (unmodulated) crystal structure, which can be described in terms of a tetragonal Cu_2Sb -type structure ($P4/nmm$) based on alternating single layers of square-planar Te sheets and a corrugated $R\text{Te}$ slab stacked along the long c direction perpendicular to the basal plane. In-plane tetragonal lattice parameters observed from the diffraction patterns are $a=4.55\text{\AA}$ for LaTe_2 and $a=4.52\text{\AA}$ for CeTe_2 and the longer ' c -axis' lattice parameter is 9.22\AA [12].

$R\text{Te}_3$ has a similar crystal structure to $R\text{Te}_2$, but with double layers of (nominally) square-planar Te sheets instead of the single Te square planes in $R\text{Te}_2$. The average crystal structure is orthorhombic, with the $Cmcm$ space group. In contrast to the tetragonal $P4/nmm$ space group, where the short a and ' b ' lattice parameters

are labeled *in* the basal plane, the long ‘*b* axis’ is *perpendicular* to the Te square planar sheet in this orthorhombic *Cmcm* space group setting. The shorter *a* and *c* lattice parameters lie in the Te planes and are almost equal in length [28]. The orthorhombicity of this bilayer compound arises from the way in which the *R*Te₂ units are stacked perpendicular to the Te planes. In the *Cmcm* space group, there exists a glide plane at $y = \frac{b}{2}$ (i.e. between the two Te planes), which gives a reflection symmetry, when upper half of the atoms are translated by $\Delta z = \frac{c}{2}$ only in the *c* direction, not in the *a* direction. Since *a* and *c* lattice parameters differ only slightly in length and such an orthorhombicity structure is very subtle especially in the layered crystals, *R*Te₃ is often termed to be “weakly orthorhombic” or “nominally tetragonal” in many experimental and theoretical literatures for simplicity [17, 18, 25].

The other title compound, *R*₂Te₅, also has a weakly orthorhombic structure (*Cmcm*) as illustrated in Figure 2.2. As for *R*Te₃, the *b* axis is along the long lattice parameter. The material is intermediate between the two better-known families *R*Te₂ and *R*Te₃ described above, consisting of alternating single and double Te layers, separated by the same *R*Te blocks. High resolution transmission electron microscope (HRTEM) image is shown for Gd₂Te₅ single crystal along [101] direction in Figure 2.2 (b), which clearly shows *R*Te block as vertically aligned two white spots, separating alternating single and double Te layers. As we will show in later sections, the electronic structure and the FS of this material are reminiscent of the single and double layer variants, essentially comprising sheets associated with each of the Te layers separately.

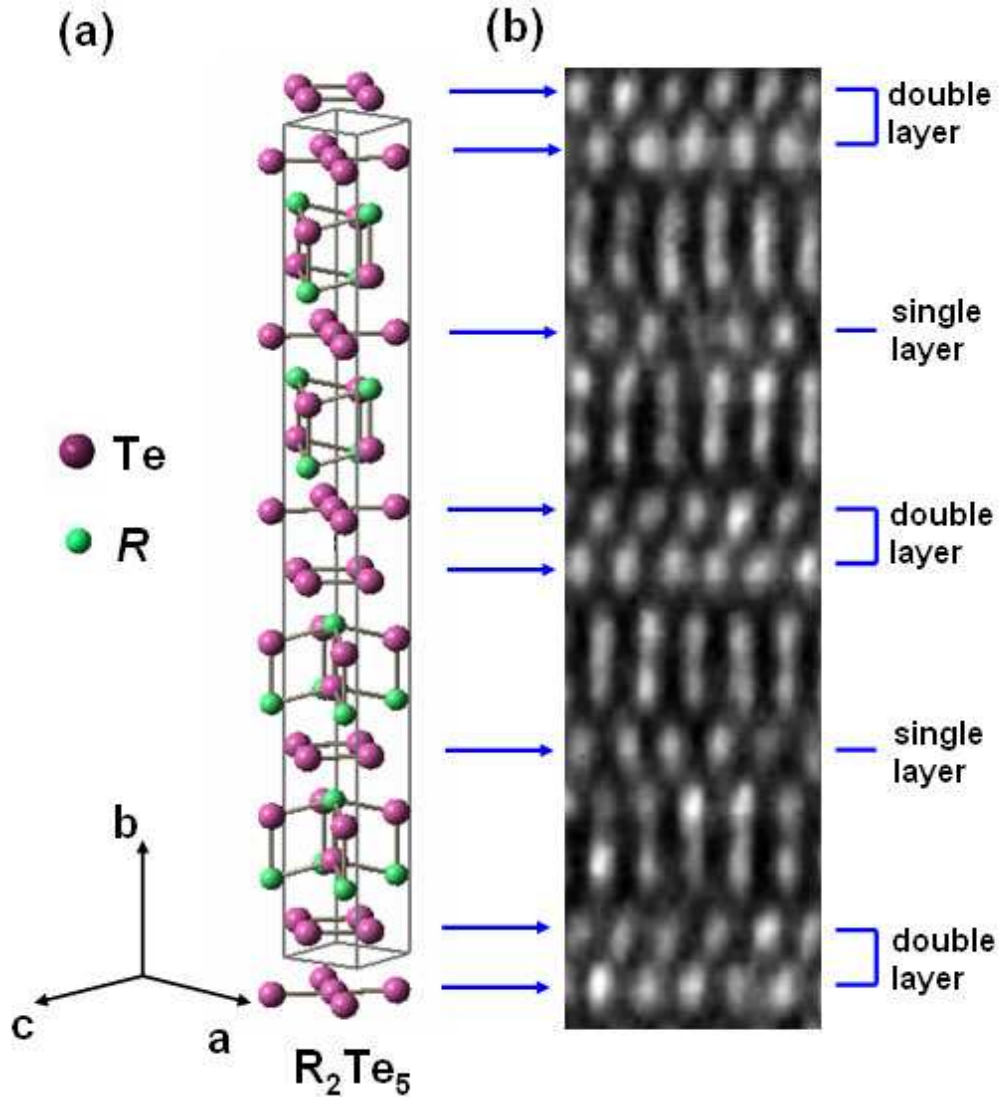


Figure 2.2: (a) Schematic diagram showing the average (unmodulated) crystal structure of R_2Te_5 . b -axis is vertical in the figure. Solid grey lines indicate unit cell. (b) High resolution TEM of Gd_2Te_5 along $[101]$ direction, showing alternating single and double Te layers (HRTEM image provided by M.J. Kramer, Ames National Laboratory).

2.2 Electronic Structure

2.2.1 Simple Tight Binding Model

Previously, DiMasi and co-workers related the commensurate $0.5a^*$ lattice modulation that they observed for LaTe_2 (see section 2.4) to a nesting condition of a model Fermi surface constructed using a simple tight-binding approach for square Te planes [2]. They showed that tuning the band filling in this model resulted in changes in the nesting wavevector, and indeed observed changes in the modulation wavevector for Sb-doped single crystals. The same simple model has also been exploited in the discussion of other experimental results, including a description of the FS of CeTe_3 observed via Angle Resolved Photoemission Spectroscopy (ARPES) by Brouet *et al* [18]. In addition, Yao *et al* addressed the relative stability of unidirectional vs. bidirectional CDW formation within the Ginzburg-Landau framework, using this simple model for the electronic structure [29]. In a similar vein, we use the same simple tight model in order to provide an easy tool to systematically understand the electronic structures and FS nesting of these families of rare earth tellurides, $R\text{Te}_2$ and $R_2\text{Te}_5$.

It has been argued by the first principle band calculations that the conduction bands in rare earth tellurides are especially simple, being determined by $5p_x$ and $5p_y$ orbitals in the nominally square Te planar layer of $R\text{Te}_2$ ($5p_x$ and $5p_z$ for $R\text{Te}_3$ and $R_2\text{Te}_5$) [30, 31]. The layered crystal structure of the rare earth tellurides allows an assumption that the couplings among the layers are negligible and the dispersion along the longer b -axis is ignored. The real space representation of the p_x and p_y orbitals is demonstrated in Figure 2.3. The p_x and p_y orbitals in Te atoms on the

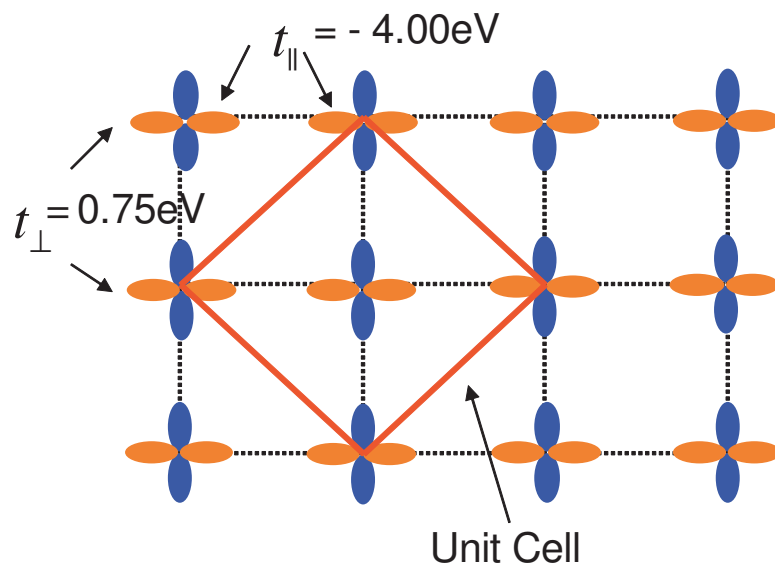


Figure 2.3: Real-space representation of a square-planar Te sheet, indicating p_x and p_y orbitals used in the tight binding model calculation.

Te square planes form conduction $5p$ bands (bonding-antibonding).¹ In the tight-binding calculation, the transfer integrals are calculated by the overlap between the two atomic orbitals. The two transfer integrals $t_{\parallel} = -4.00\text{eV}$ and $t_{\perp} = 0.75\text{eV}$ ² between the nearest-neighbor Te p orbitals [18,30] are denoted in Figure 2.3 and the resulting energy band equations are given in Equation 2.1 after straightforward algebra. For computational simplicity, 2D Te lattice was rotated by 45° in the Te square plane and this new coordinate was used in the matrix diagonalization. The band equations in Equation 2.1 were obtained by rotating back by -45° to properly consider the 3D

¹LMTO calculations confirm that p_z orbitals are pushed below E_F by crystal field effects.

²These values are obtained by fitting ARPES data of CeTe_3 single crystals to the tight binding model as described in reference [18] and successfully described experimental observation of the electronic structure and the CDW FS reconstruction.

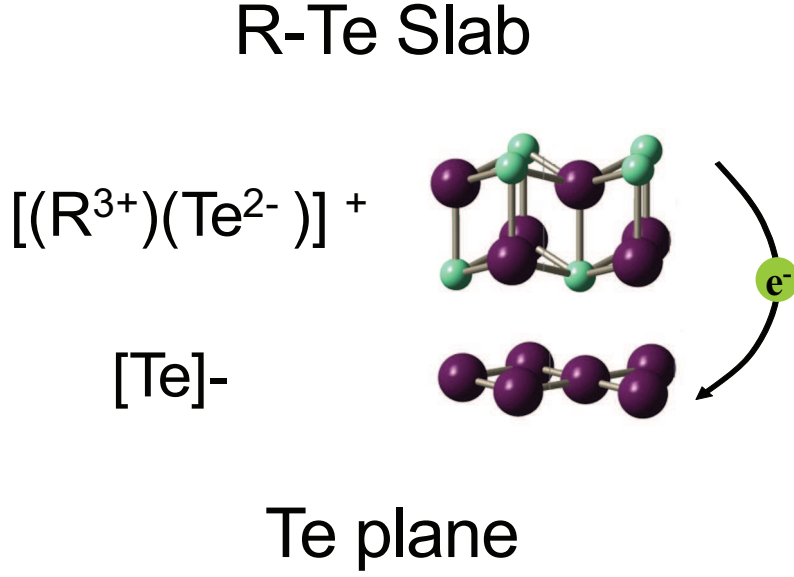


Figure 2.4: Schematic representation of the charge transfer. One R -Te slab contributes one electronic charge to the p orbitals of Te atoms in the square plane. There are one and two Te planes per R -Te slab in RTe_2 and RTe_3 respectively, which gives different band fillings in the conduction bands.

crystal unit cell lattice in the k_x - k_y plane.

$$\begin{aligned}
 E_k^1(k_x, k_y) &= -2t_{\parallel} \cos \left[\frac{(k_x + k_y)a}{2} \right] + 2t_{\perp} \cos \left[\frac{(k_x - k_y)a}{2} \right], \\
 E_k^2(k_x, k_y) &= -2t_{\parallel} \cos \left[\frac{(k_x - k_y)a}{2} \right] + 2t_{\perp} \cos \left[\frac{(k_x + k_y)a}{2} \right], \quad (2.1)
 \end{aligned}$$

Using this rigid band picture, band filling in each family of rare earth tellurides can be understood in a simple way. Rare earth ions and tellurium ions in R -Te blocks are strongly bonded and in the oxidation states of R^{3+} and Te^{2-} , which becomes a block state of $[R-Te]^{1+}$. Each R -Te pair donates one electron to the Te planes nearby, providing excess electrons that fill the bands given in Equation 2.1, which is

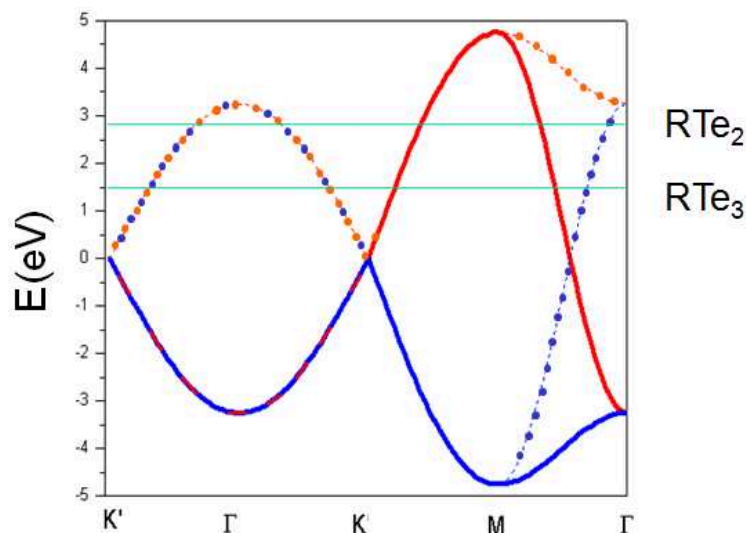


Figure 2.5: Band structure for the model, showing band filling corresponding to $R\text{Te}_2$ at $E_F=2.8\text{eV}$ and $R\text{Te}_3$ at $E_F=1.5\text{eV}$.

shown in Figure 2.5 for $R\text{Te}_2$ and $R\text{Te}_3$.³ Since each family of rare earth tellurides has different number of Te planes per R -Te block, the band fillings are different, but still can systematically be accessed by a proper electron density counting in the conduction bands. For example, $R\text{Te}_2$ compounds have one Te plane (two Te atoms in one plane) per one R -Te block (two R -Te pairs in one R -Te block) in a unit cell, while $R\text{Te}_3$ has two Te planes available for each R -Te block. Thus, if n is the number of electrons in both p_x and p_y orbitals from the two Te atoms, $R\text{Te}_2$ and $R\text{Te}_3$ have $n=6.0$ and $n=5.0$ in the conduction bands respectively.⁴

The resulting FS is represented in Figure 2.6 for $R\text{Te}_2$ compounds in the extended

³ $\text{Te}^{2-}:[\text{Kr}]4d^{10}5s^25p^6$

⁴ $n=5\frac{1}{3}$ in $R_2\text{Te}_5$ in the conduction bands when uniform charge distribution is assumed. However, this turned out to be incorrect, because this simple model is oversimplified for this compound, ignoring band crossings and splittings too much (Figure 2.7). $R_2\text{Te}_5$ has a very long unit cell along the b axis and FS splittings differ for single and double Te planar layers, due to the R -Te block positions along the b axis [13].

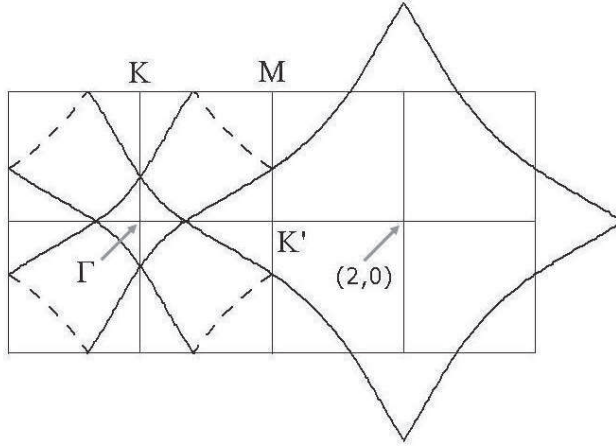


Figure 2.6: Resulting Fermi surface for $R\text{Te}_2$, neglecting hybridization between p_x and p_y orbitals. Solid lines indicate bands in the extended zone scheme and show sections we identify as the *inner* and *outer FS* centered at Γ and $(2,0)$ respectively. Dashed lines represent the bands folded into the reduced zone according to the periodicity of the unit cell, as shown in Figure 2.3.

and the reduced zone in reciprocal lattice space. The *outer* FS, a square centered at $(k_x, k_y) = (2, 0)$ in solid line, can be translated back to the 1st BZ, giving the smaller *inner* FS in solid and dashed lines, centered around the Γ point. $R\text{Te}_3$ has a *inner* FS around the Γ point larger than the *inner* FS in $R\text{Te}_2$ [12, 18]. The differences in the FS size and topology between $R\text{Te}_2$ and $R\text{Te}_3$ can be simply explained by the Fermi level difference due to the higher charge carrier density in $R\text{Te}_2$ (Figure 2.5) in this tight-binding rigid band model.

2.2.2 LMTO Band Structure Calculation

The electronic band structures for the families of the rare earth tellurides have been calculated using the linear muffin-tin orbital (LMTO) method within the atomic sphere approximation including combined-correction terms, as described in Refs. [31]

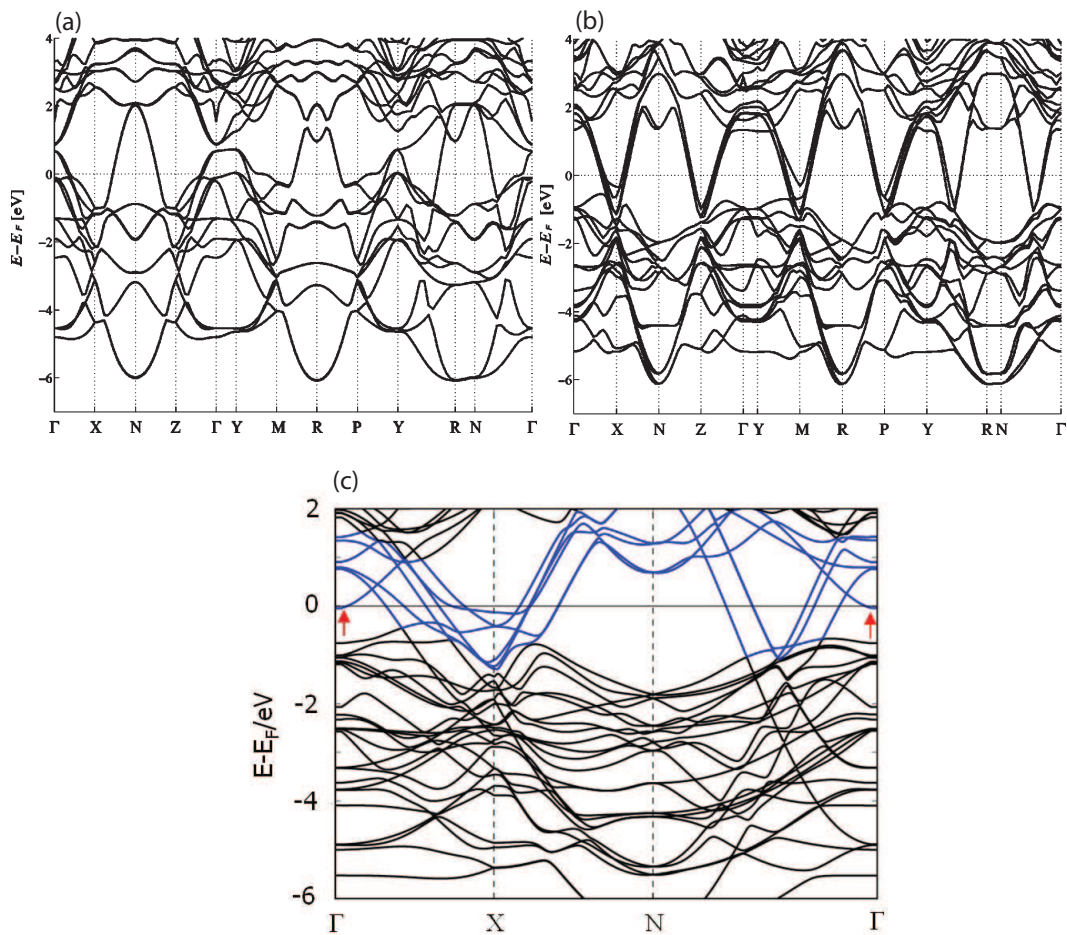


Figure 2.7: Band structures for (a) LuTe₂, (b) LuTe₃ [31] and (c) Lu₂Te₅ [13] calculated by LMTO from the references indicated above. Conduction bands are mainly formed by 5p orbitals from Te square planes. The conduction band splittings at the FS are relatively smaller in LuTe₃ than in Lu₂Te₅ (blue lines in (c)). The red arrow in (c) indicates a small electron pocket due to the hybridization with a Lu *d*-state above E_F for Lu₂Te₅.

and [32] and the results are shown in Figure 2.7 specifically for $R=\text{Lu}$ (chosen to avoid the complications associated with the description of (band) f -electrons within the local density approximation). The slight difference in lattice parameters originating from the structural orthorhombicity was ignored in the calculation [13,31]. Since the FS is comprised of Te $5p$ states originating from the Te atoms in the square planar layers, the general *topology* of the FS is relatively insensitive to the particular choice of rare earth atom, and indeed to changes in the lattice parameter of $\sim 5\%$, allowing us to interpret these results as prototypical for all of the other rare earth compounds. All calculations included a basis of s , p , d and f states, and self-consistency was achieved at 1280 k-points in the irreducible $(1/8)^{\text{th}}$ wedge of the BZ (corresponding to a mesh of $30 \times 8 \times 30$ in the full BZ).

Bands formed by $5p$ orbitals from Te square planes were observed to cross the Fermi level (in Figure 2.7) and the corresponding FSs at $k_z = 0$ for LuTe_2 and $k_y = 0$ for LuTe_3 and Lu_2Te_5 are depicted in Figure 2.8. The arrows in each FS diagram in Figure 2.8 indicates the CDW nesting wave vectors observed in each family of compounds [2,13,17]. The Fermi surfaces for LuTe_2 and LuTe_3 are in good accordance with the ones calculated from the simple tight binding model, while such a simple model for Lu_2Te_5 doesn't seem to approximate the FS properly due to the trilayer splittings and the complex band mixings. As in $R\text{Te}_2$ and $R\text{Te}_3$ [31], the electronic structure for $R_2\text{Te}_5$ is two dimensional and has minimal dispersion perpendicular to the Te planes(Figure 2.8(c)).

In the tritelluride compounds, the inequivalence of the two Te atoms in the double square planar layer breaks the degeneracy of these bands, and the resulting bilayer splitting has been observed directly in ARPES studies [18,33]. For $R_2\text{Te}_5$, in addition

to this double Te sheet, there is an additional single Te layer, and the band structure reflects this via a triple splitting of its Te states. The splitting between states originating from the double layer is weak and of a similar magnitude to the bilayer splitting in the tritelluride compounds, whereas the splitting between either of these double layer states and the state due to the single layer is more significant [31].

In addition, a small circular electron pocket due to the hybridization with a Lu d -state above E_F for Lu_2Te_5 (indicated by red arrows in Figure 2.7 (c)) was observed around the Γ point. Details of this hybridization are sensitive to the rare earth involved in the calculation, unlike the other Te $5p$ bands, and hence we might expect that the presence and exact volume of this pocket varies, as we progress through the lanthanide series. This in turn may vary the precise location of E_F within the Te $5p$ bands, although small fluctuations of the electron pocket volume do not seem to significantly impact interactions between $5p$ electrons in the Te square planes.⁵

Even with the same a and c lattice parameters used in the calculation, the orthorhombicity due to the relative orientation of R -Te slabs in different layers is reflected in the electronic structure of both $R\text{Te}_3$ and $R_2\text{Te}_5$ and produced unequal electron pockets centered at X and Z (Figure 2.8). The directional difference in the electronic structure, in turn, suggests that the band splitting at the Fermi level partially depends on the relative geometry and interactions between Te atoms in square planes and rare earth atoms in the R -Te slabs, even though the interplanar interaction is believed to be small.

Nevertheless, the overall topology of the FS of $R_2\text{Te}_5$ is surprisingly similar to the individual sections of mono- and bi-layer FS structures of $R\text{Te}_2$ and $R\text{Te}_3$ (Figure 2.8

⁵The topology of this small circular section does not contribute any appreciable peak structure to the susceptibility, leading us to put less emphasis on it in the subsequent analysis of $\chi(\vec{q})$ in the sections following.

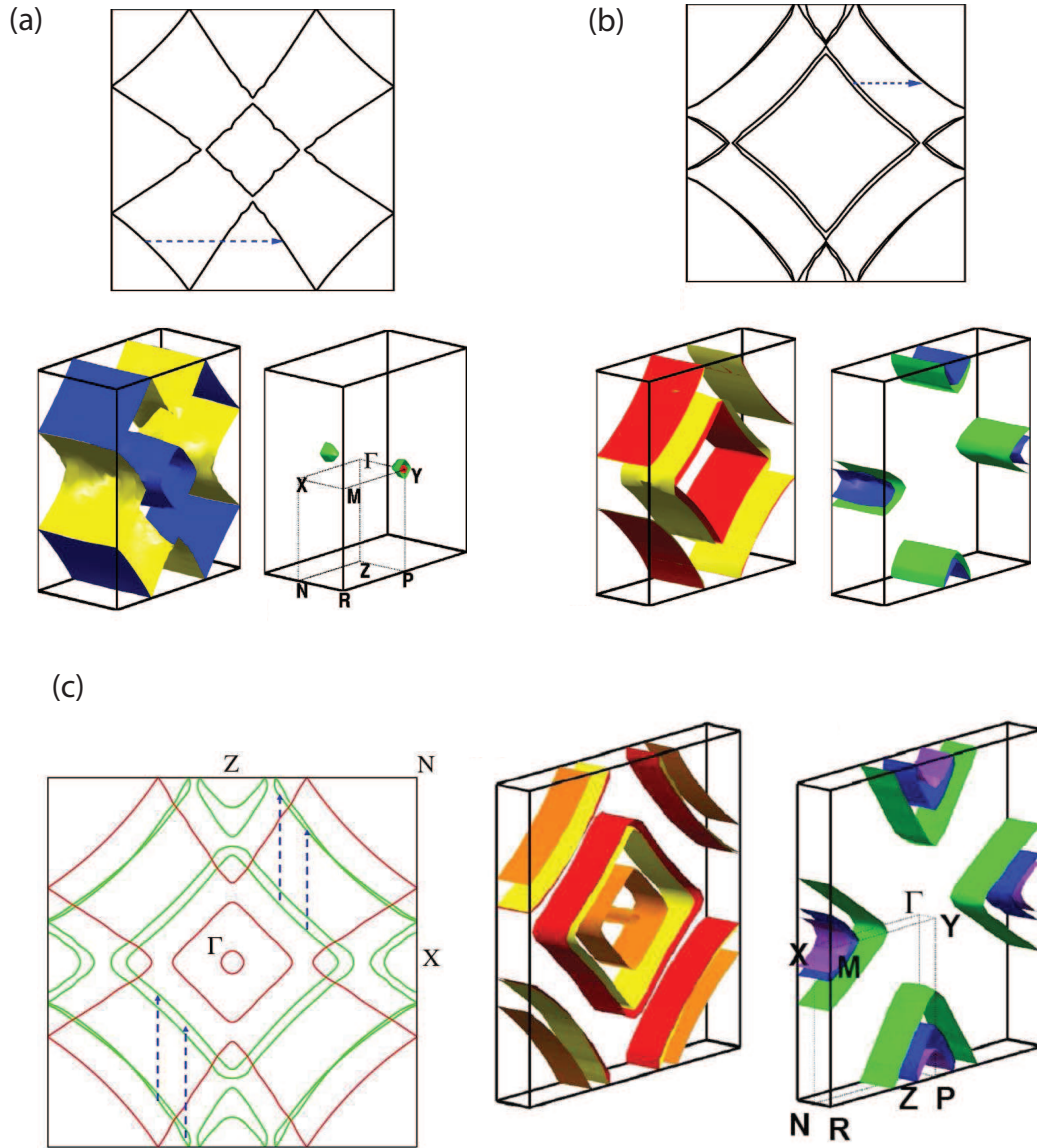


Figure 2.8: The FS of LuTe_2 , LuTe_3 and Lu_2Te_5 calculated by LMTO in (a),(b) (from the reference [31]) and (c)(from the reference [13]) respectively. The surfaces shown for FS at $k_y = 0$ in (c) illustrate the trilayer splitting that arises due to coupling between the three Te planes. Arrows indicate the on-axis lattice modulation $\vec{q} \sim (2/3)c^*$ observed in SADP for Nd_2Te_5 , Sm_2Te_5 and Gd_2Te_5 .

(a) and (b)) and thus can be approximated by superposing the corresponding Fermi surfaces of those two materials with only minor changes to account for differences in band filling. A close investigation of the character of the wavefunction at each point supports this view and revealed that the origin of the individual FS sections can mostly be attributed to $5p$ atomic orbitals in either the ditelluride-like single Te planar layer or the tritelluride-like double Te planar layers respectively (red and green lines in Figure 2.8 (c)), if the strong orbital hybridization or orbital mixing is ignored near the band crossings at the Fermi level. This is somewhat as expected, considering that the orthorhombic structure of $R_2\text{Te}_5$ is intermediate of $R\text{Te}_2$ and $R\text{Te}_3$ with very close ac parameters and alternating single and double Te layers along the $[010]$ direction.

In the following sections, I briefly review experimental observations for each of these 3 families of compounds separately. At the time of this research, more was known about the tritellurides $R\text{Te}_3$ than the other two compounds, so I describe these first.

2.3 $R\text{Te}_3$

2.3.1 CDW Superlattice and Electronic structure

Due to the simplicity of the crystal structure and the CDW modulations, the family of the bi-layer compound $R\text{Te}_3$ forms an ideal model system to explore CDW formation and has been extensively studied. The incommensurate superlattice modulations in rare earth tritellurides were first observed using TEM diffraction technique by DiMasi and coworkers [34]. In Ref. [34], SADPs for $R\text{Te}_3$ ($R=\text{La, Sm, Gd, Tb, Dy, Ho, Er, Tm}$) have shown that the lattice modulation is stable against chemical pressure and

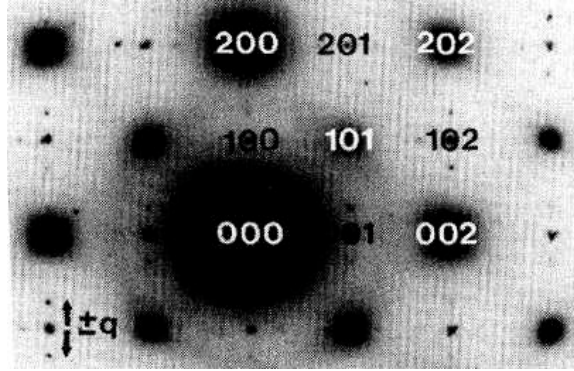


Figure 2.9: SADP from TEM on SmTe_3 single crystal at 273K from the reference [34]. In the figure, the superlattice wave vector, $q = (2/7)c^*$, is indicated.

stays very close to $q \approx (2/7)c^*$ along the c axis at or below room temperature across the rare earth series. Ru *et al.* recently found consistent results for single crystals grown via different technique [17]. In both of the measurements, the origin of the observed superlattice was ascribed to the CDW driven by the electronic structure and the nesting of the quasi 2D FS.

While the SADP measurement from TEM is limited to $k = 0$ plane, high resolution X-ray diffraction is more versatile for probing the lattice distortions in the nominally entire reciprocal lattice space and additional information on the CDW satellite peak intensities can be gained. Use of a synchrotron source (in our case, SSRL) is advantageous for observing weak intensity satellite peaks. Ru *et al.* recently reported extensive the high resolution X-ray diffraction studies on several rare earth tritellurides measured at the Stanford Synchrotron Radiation Laboratory (SSRL) and an example of X-ray diffraction scan for TbTe_3 at room temperature is illustrated in Figure 2.10 for (1 1 L) and (2 4 L) planes [17]. The representative data clearly show very sharp incommensurate satellite peaks at $q=0.296c^*$ (or equivalently, $c^* - q=0.704c^*$) and the correlation length ξ calculated from the full width at half maximum (FWHM)

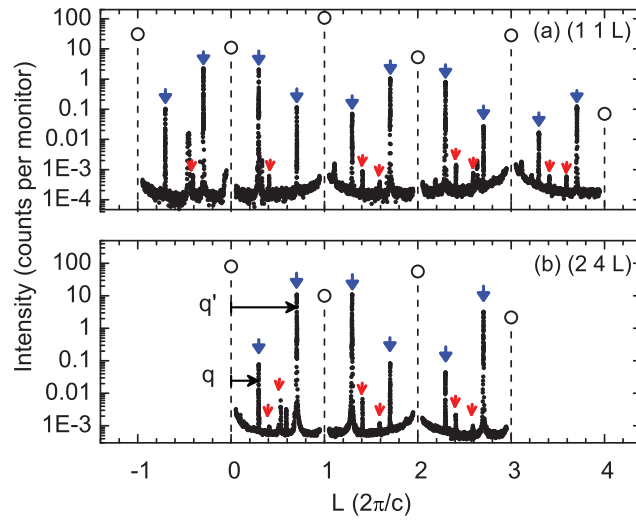


Figure 2.10: X-ray diffraction scan for TbTe_3 along the in-plane L direction from reference [17]. Arrows indicate CDW superlattice peaks. Circles indicate Bragg peaks from the average structure.

is over $1.8\mu\text{m}$ in the ac plane and $0.5\mu\text{m}$ perpendicular to the plane. These values are macroscopically long and correspond to the CDW extending more than thousand times of the unit cell in the Te planes and more than hundred times of the long b lattice parameter perpendicular to the Te plane. The high intensity of the X-ray beam allows the observation of the higher harmonic of the modulations and Figure 2.10 reveals the second harmonic wave vector, $2q=0.592c^*$, of the incommensurate modulations at a much reduced intensity.⁶

The simple tight binding model proposed in the previous section was successful in identifying electron susceptibility enhancement structure for $R\text{Te}_3$ as well as $R\text{Te}_2$ [12]. Figure 2.11 shows Lindhard susceptibility functions for $R\text{Te}_3$, calculated from the simple tight binding model [35] and an ab initio band structure calculation [26]. Considering the simplicity of the tight binding model, the resultant $\chi(q)$ functions are surprisingly similar to each other and both of the calculations effectively illustrates a sharp peak developed at $q \approx (2/7)c^*$ on c axis, which corresponds to the nesting wave vector shown in Figure 2.8 (b).

Angle resolved photoemission spectroscopy (ARPES) is a powerful tool to directly probe filled electron bands, and experimentally shows the FS topology and FS gap features. Rare earth tellurides have huge energy gaps, ranging from 280meV for SmTe_3 [33], 400meV for CeTe_3 [18] to 600meV for CeTe_2 [12]. A recent measurement of the spectral weight of CeTe_3 in ARPES is shown in Figure 2.12. The simple tight binding model was utilized to fit the actual bands and the corresponding FS measured in ARPES, which is, indeed, quite successful in grasping the underlying physics without losing the essential nesting features [18]. The sections of FS nested by wavevector $q \sim (2/7)c^*$ are indicated by an arrow in the figure, and exhibit a

⁶The existence of the second harmonic may suggest either non-sinusoidal CDW modulations or simply the high order harmonics of the X-ray diffraction.

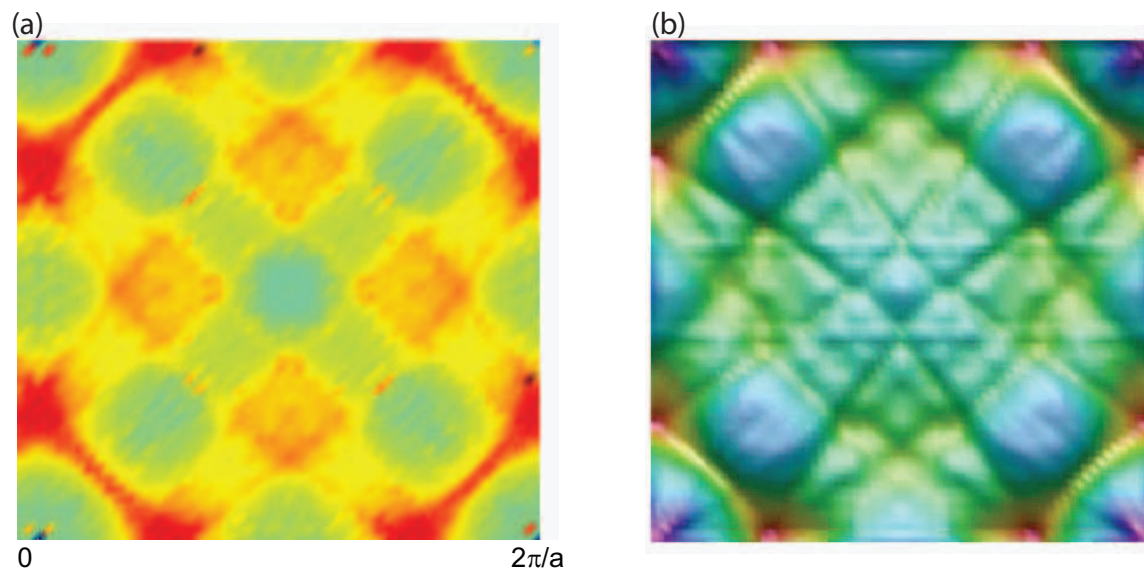


Figure 2.11: Lindhard susceptibility function $\chi(q)$ of $R\text{Te}_3$ for (a) simple tight binding model (Shin, (unpublished)) and (b) ab initio band structure calculation from reference [26]. Color scale: High in red and low in blue.

substantial gap, while the remaining FS is ungapped contributing electrons to charge carrier conduction. CDW formation in CeTe_3 does not change the material from a metallic into a non-conducting state and such a coexistence of the gapped and ungapped FS symbolizes the characteristics of the imperfect nesting in 2D CDW materials, in sharp contrast to the 1D CDW.

2.3.2 Temperature Dependence of the CDW

Extensive resistivity measurements on the rare earth tritellurides were recently reported by N. Ru *et al* [17] and Figure 2.13 (a) shows a representative temperature dependence of the resistivity in TbTe_3 up to 400K for currents along and perpendicular to the long b -axis direction. The resistivity is strongly anisotropic as expected for the quasi 2D materials [25, 36]. There is a clear anomaly at 336K for TbTe_3 without

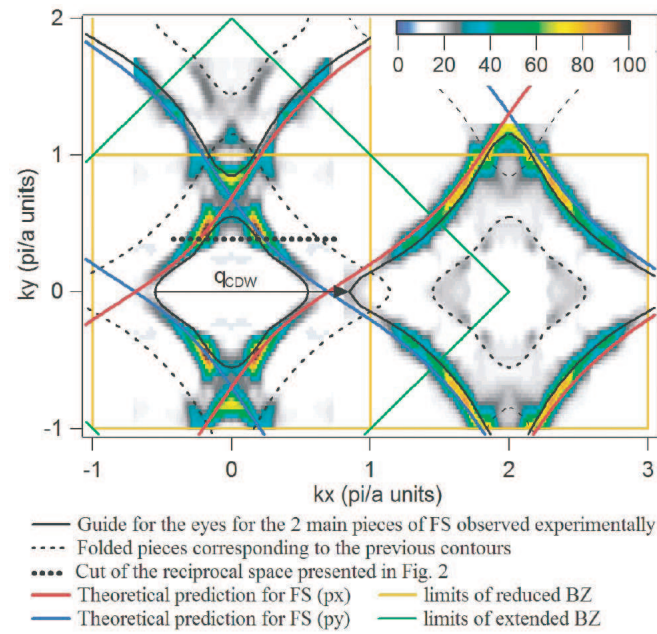


Figure 2.12: FS in CeTe_3 obtained by ARPES at 25 K, with photon energy $h\nu=55\text{eV}$ from reference [18]. The spectral weight is integrated between E_F and $E_F-200\text{meV}$.

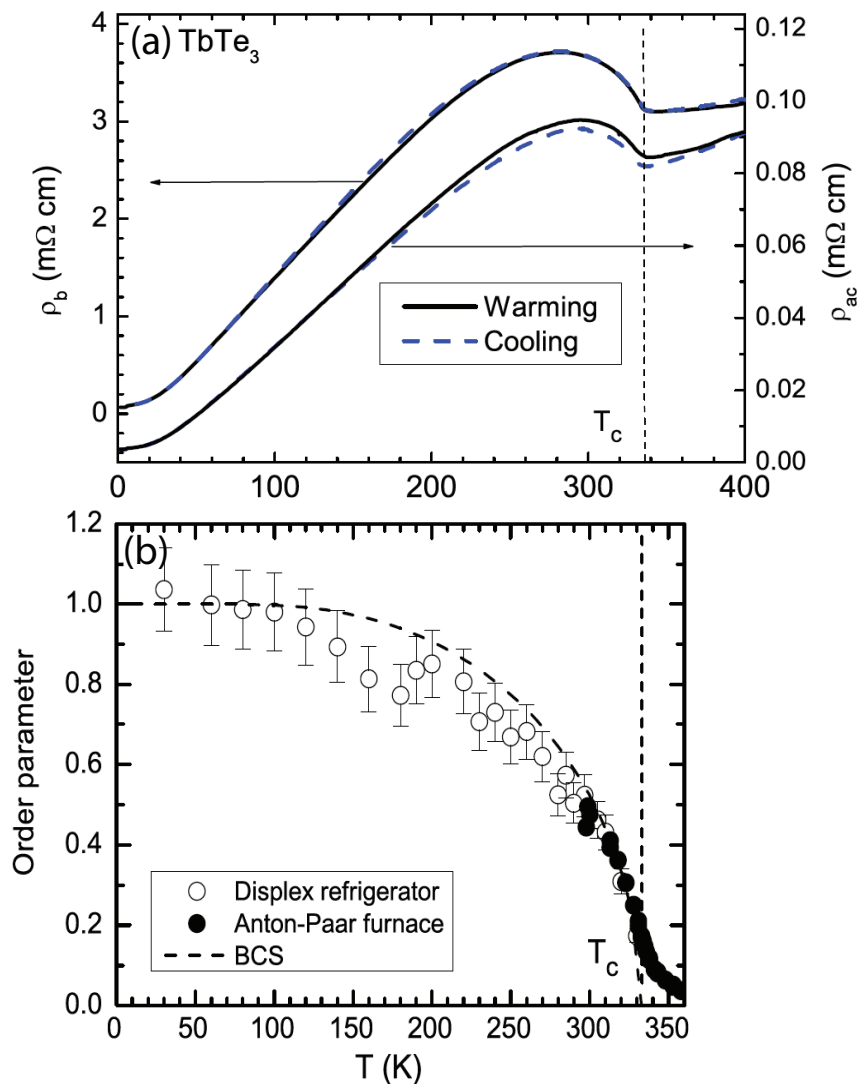


Figure 2.13: (a) The temperature dependence of the resistivity and (b) the CDW order parameter in TbTe_3 , from reference [17]. The resistivity data have been measured for currents along and perpendicular to the b -axis in Figure (a), ρ_b and ρ_{ac} respectively, and show a clear anomaly at $T_C=336$ K. The order parameter is measured from the square root of the integrated intensity of X-ray diffraction satellite peak at $(1\ 1\ q)$ and the transition temperature is inferred from the feature in the resistivity.

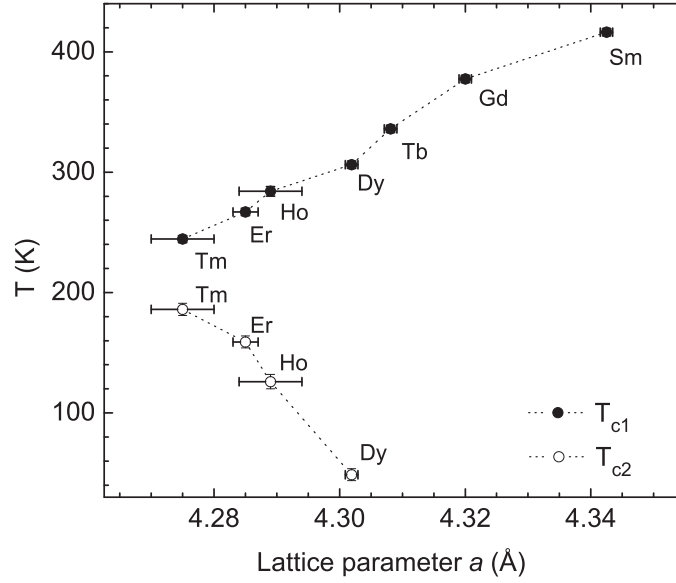


Figure 2.14: CDW transition temperatures in $R\text{Te}_3$ across the rare earth series, from reference [17]. A second transition temperature T_{c2} has been identified for heavier rare earths.

hysteresis upon heating and cooling, suggesting a second order CDW transition at this temperature [17]. The actual transition temperatures are significantly lower than the simple mean field temperatures estimated from the maximum energy gaps in ARPES data [18]⁷, which has been ascribed to the CDW transition substantially suppressed by the imperfect nesting and low dimensional fluctuations [17]. Figure 2.13 (b) shows the temperature dependence of the CDW order parameter, estimated from the square root of the integrated intensity of the CDW peak at $(1\ 1\ q)$, along with the standard BCS curve [17]. The intensity of the satellite peak rapidly decreases down to the transition temperature $T_C=336\text{K}$ and there remain weak scattering intensities due to fluctuations above T_C . The excellent fit to the BCS curve within the experimental limit suggests that the CDW can be treated in the weak coupling limit.

⁷Simple estimate of the mean field transition from the energy gap 400meV for CeTe_3 is 2600K. It is above the melting temperature of the material itself.

Transition temperatures for other rare earths are identified from similar features in resistivity and shown in Figure 2.14 with T_{c1} decreasing for heavier rare earths from 416K for SmTe_3 to 244K for TmTe_3 [17]. Meanwhile, the figure also shows the emergence of a second CDW transition at the lower T_{c2} increasing for heavier rare earths upon progressing from DyTe_3 to the heavier TmTe_3 , i.e. with the decreasing chemical pressure. It is, in general, extremely difficult to theoretically calculate the actual phase transition temperature, especially for the imperfectly nesting 2D CDW materials. However, useful insights can still be provided, in some extent, by understanding how the most relevant parameters vary upon tuning the physical properties. In the literature Ref. [17], it was theoretically argued that the decreasing chemical pressure due to the lanthanide contraction principally reduces the density of the states near the FS without varying the effective band fillings too much. Since the mean field estimate of the transition temperature is exponentially proportional to the density of states at the Fermi level (Equation 1.9), T_{c1} monotonically decreases on crossing to the heavier rare earths as in Figure 2.14. ARPES measurements on $R\text{Te}_3$ ($R=\text{Ce}$, Sm and Er) have provided experimental evidences that rare earth tritelluride compounds actually have diminishing area of gapped FS and smaller maximum gap values for the first CDW on traversing from lighter Ce to heavier Er , which, in turn, gives more of the remaining regions of ungapped FS readily available for second CDW nesting [17].

The diffraction peaks in high quality ErTe_3 single crystals were investigated at temperatures below room temperature, and X-ray measurements indeed revealed a new additional CDW ordered state with $q_2 \approx (1/3)a^*$ ($a^* = 2\pi/a$), emerging below $T_{c2} \approx 185\text{K}$ [17]. Furthermore, low temperature ARPES data on ErTe_3 have shown that an additional gap develops in the ungapped regions of the FS at this wave vector.⁸

⁸R. Moore *et al.*, private communication.

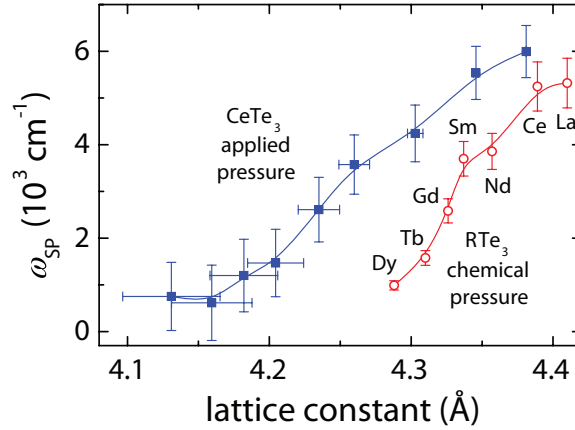


Figure 2.15: Single particle excitation energy ω_{SP} at room temperature as a function of the lattice constant a for CeTe_3 under applied pressures and for the $R\text{Te}_3$ series. Solid lines are guides to the eye from reference [4].

It explains the competing CDW states and is in accordance with the changes in the two sets of transition temperatures.

2.3.3 Pressure Effects on $R\text{Te}_3$

Optical conductivity spectroscopy measures the response of the electrodynamic interaction with the charge carriers and recent experiments by Sacchetti and coworkers addressed the questions on the tuning effects of chemical and hydrostatic compression in $R\text{Te}_3$ [4, 15, 16]. The single particle (SP) excitation energy, ω_{SP} , is particularly interesting, since it gives estimates of the average CDW gap values and, therefore, can be related to the CDW transition temperatures. The weighted average of ω_{SP} over the entire FS have been used as a guide for the comparison between the compounds [4]. The authors discovered that ω_{SP} is reduced upon chemical compression by the rare earth series [3] and the effect of chemical pressure can be reproduced in CeTe_3 [4] by

externally applying the hydrostatic pressures (Figure 2.15).⁹

The effect of chemical compression on the energy gap is similar to the progressive change in the CDW transition temperature T_{c1} and they seem to result from the same origin previously discussed. But it can hardly be conjectured that these experimental observations are a sole effect of the subtle variations in the electronic structure without the phonon mode interaction. Moreover, such an ionic substitution changes the relative ratios of the atomic masses of the constituent elements, R/Te , more than 20% from 1.09 for Ce to 1.32 for Tm. This is likely to affect the phonon mode dynamics and the electron-phonon coupling and, yet, similarity in trend between the two sets of data from CeTe_3 under the applied pressure and rare earth tritelluride series is still very remarkable and the impacts of the varying density of states is believed to dominate the CDW transition phenomenon.

2.4 $R\text{Te}_2$

CDW formation at $q \approx \frac{1}{2}a^*$ was first observed by DiMasi and coworkers in LaTe_2 [2]. Since then, there have been efforts to tune the electron band fillings or the size of the FS, while minimizing the impacts on the electron bands. DiMasi *et al* reported from transmission electron microscopy (TEM) diffraction measurements that the band filling in LaTe_2 is continuously decreased and CDW modulations get modified accordingly, with essentially no changes in the LaTe_2 band structure, as the Te atoms are substituted by Sb atoms [2]. The system has a wide band width of $\sim 5\text{eV}$ with no or very few band crossings near the FS, which allows a relatively smooth change of the FS by charge carrier doping. Sb doping to the nominally LaTe_2 single crystal, using an alkali halide flux method, replaces the Te atoms in the Te square plane and

⁹Similar results can be found for LaTe_2 in references [16] and [15].

contributes hole carriers to the $5p$ conduction bands (the square hole pocket in the center becomes larger upon Sb doping in Figure 2.16).

The selected area diffraction patterns (SADP) from TEM show the evolution of the observed distortion wavevectors upon Sb doping in a range from $LaTe_2$ to $LaTe_{1.2}Sb_{0.7}$ [2]. It is noticeable that the hole doped compounds do not make the composition stoichiometric, for example, $LaTe_{1.6}Sb_{0.3}$, due to the presence of Te vacancies in the Te planes [37–39]. The distortion wave vectors, $q = (1/2)a^*$ for $LaTe_2$, $q = (2/3)a^*$ for $LaTe_{1.6}Sb_{0.3}$ and $q = 0.763a^*$ for $LaTe_{1.2}Sb_{0.7}$, are all *on-axis* along the a^* direction, while $q = 0.672a^* + 0.078b^*$ for $LaTe_{1.6}Sb_{0.3}$ is slightly *off* the a^* axis.¹⁰ Figure 2.16 demonstrates the progressive change of the FS, modified by the varied band fillings due to Sb doping and all of the CDW modulations are shown to be still at the geometrically plausible nesting wavevectors for each of the doped compounds. The simple FS nesting partly explains the most plausible CDW instabilities (Equation 1.6) But more rigorous studies are still required to demonstrate whether the suggested distortions are actually the most energetically favorable. Part of such a study has been performed in the configuration space of the various CDW modulation structures in the rare earth tritellurides by Yao and the coworkers [29]. Nonetheless, the correspondence between the experimental and the theoretical observations is remarkable and considerable insight into the favored CDW modulations can be gained.

2.5 R_2Te_5

Compared to the relatively well known rare earth di- and tritellurides, the family of R_2Te_5 is much less investigated. Although crystals of R_2Te_5 have previously been grown from an alkali halide flux and their average structure was reported [36, 40], no

¹⁰In contrast to the RTe_3 and R_2Te_5 , the basal plane is formed by a and b axis in $LaTe_2$ structure.

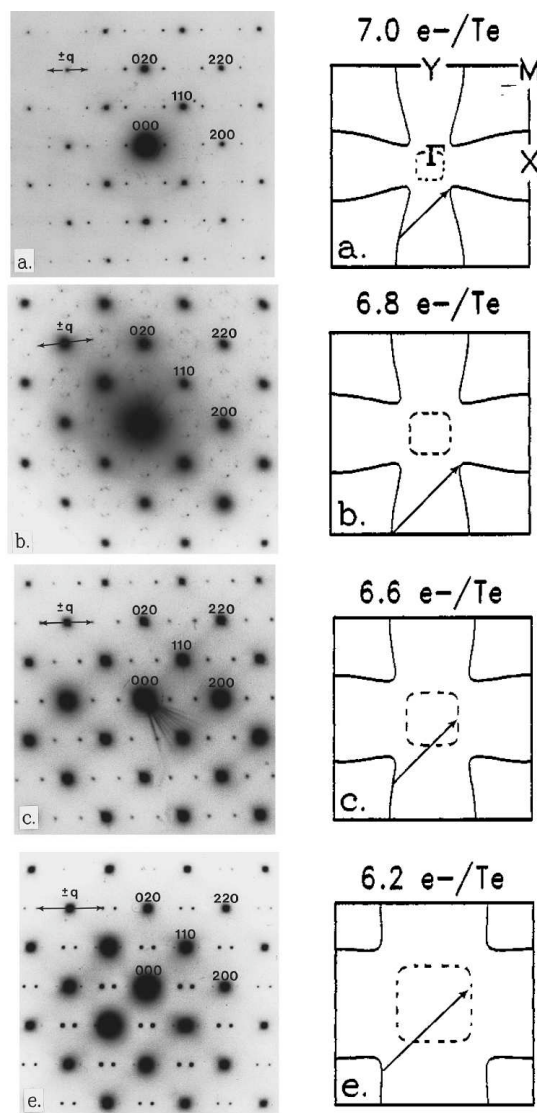


Figure 2.16: Variation in the nesting wave vectors upon the hole doping in LaTe_2 from reference [2]. SADPs for $\text{LaTe}_{2-x}\text{Sb}_x$ along the (001) zone axis. Bragg peaks ($hk0$) for $h + k = \text{even}$ are indexed. Satellite peaks at (a) $q \approx (1/2)a^*$ for LaTe_2 , (b) $q = 0.672a^* + 0.078b^*$ for $\text{LaTe}_{1.6}\text{Sb}_{0.3}$, (c) $q \approx (2/3)a^*$ $\text{LaTe}_{1.6}\text{Sb}_{0.3}$ and (d) $q = 0.763a^*$ for $\text{LaTe}_{1.2}\text{Sb}_{0.7}$ along with the FS nesting wave vectors observed in TEM for each stoichiometry. The carrier concentrations are expressed in terms of the number of electrons in s and p orbitals per Te for each doped compound from 7.0 for LaTe_2 to 6.2 for $\text{LaTe}_{1.2}\text{Sb}_{0.7}$.

superlattice modulation had been identified for this material and the CDW had never been explored experimentally. In this study, we describe an alternative method to grow high quality single crystals of R_2Te_5 from the binary melt, and use transmission electron microscopy (TEM) and high resolution X-ray diffraction to probe the lattice modulation for three representative members of the series, Nd_2Te_5 , Sm_2Te_5 and Gd_2Te_5 . We find that all three compounds R_2Te_5 ($R=Nd, Sm, Gd$) exhibit a modulation wavevector oriented along the c axis with a magnitude close ($R=Nd, Gd$) or equal ($R=Sm$) to $2/3c^*$, similar to that of the tritelluride compounds. In addition, each compound exhibits at least one further set of superlattice peaks oriented away from the c^* axis. Calculations of the Lindhard susceptibility show that contributions to $\chi(q)$ enhancements arise from sections of the Fermi surface associated separately with the single and double Te planes and indicate that these different wavevectors, at least for $R=Sm$ and Gd , originate from CDW formation in the double and single Te planes respectively. We also show for the representative member of the series, Gd_2Te_5 , that the *on*- and *off*-axis CDWs suffer separate CDW transitions and are not completely independent.

Chapter 3

Experimental Methods

3.1 Single Crystal Sample Preparation

Single crystals typically provide the highest levels of purity, and enable exploration of the anisotropic properties of a material. Consequently, it is always preferred in a variety of experiments that probe both macroscopic and microscopic scales. The most important experimental measurements on the condensed matter systems, such as de Haas-van Alphen effects, angle resolved photoemission spectroscopy, high resolution elastic and inelastic scattering, and scanning tunneling microscopy, can only be effective on the best single crystalline samples [13, 18, 41–43], and substantial efforts have been made in order to optimize the growth techniques for the materials described in this thesis.

Here we describe a self-flux technique that we favor since it produces crystals with the highest levels of purity without the use of a third-element flux or a chemical transport agent [12, 44]. This technique is possible because both compounds have an

exposed liquidus in the binary alloy phase diagram. Furthermore, by using a hot-decanting technique to remove the flux (i.e. excess Te) before it solidifies, we are able to minimize strain in the resulting crystals.

3.1.1 Crystal Growth: $R\text{Te}_2$

Previously, single crystals of $R\text{Te}_{2-\delta}$ have been grown via chemical vapor transport [45,46], from an alkali-halide flux [2], via mineralization of a nominally stoichiometric binary mixture of elements [47], and via a high-temperature Bridgman method [48, 49]. However, the growth materials generally have to be processed at enormously high temperatures or high vapor pressures in these techniques, which often causes experimental complications in, for example, maintaining the protective environment for the entire growth process and limits the usefulness of the techniques. [50]

With reference to the binary phase diagrams of Ce-Te and La-Te [37], it is clear that single crystals of $R\text{Te}_2$ ($R=\text{La}, \text{Ce}$) can be grown from a binary melt. Our experiments indicate that the exact position of the liquidus in the published phase diagrams is not entirely accurate, but nevertheless they are a good starting point. Previously we have prepared single crystals of CeTe_3 by this technique, slowly cooling a Te-rich melt [18]. The growth of $R\text{Te}_2$ requires a greater relative concentration of the rare earth element, and substantially higher temperatures, but is otherwise very similar.

Elements in the molar ratio from $\text{Ce}_{0.14}\text{Te}_{0.86}$ to $\text{Ce}_{0.18}\text{Te}_{0.82}$ and from $\text{La}_{0.15}\text{Te}_{0.85}$ to $\text{La}_{0.18}\text{Te}_{0.82}$ were put into alumina crucibles and vacuum sealed in quartz tubes. The quartz tubes have been flushed with Ar gas at least three times and the pressure has been kept below 50mmHg before the sealing. Two alumina crucibles sized by ϕ

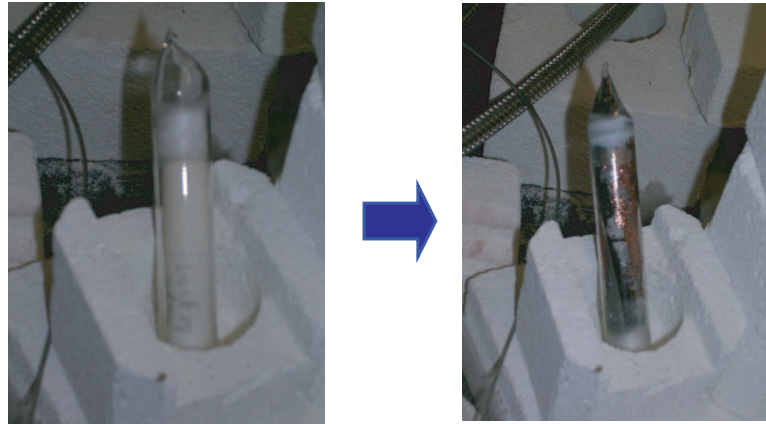


Figure 3.1: Growth quartz tube. Quartz wool protects the tube during decanting in the centrifuge.

Crystal	Melt Composition (at.%Te)	Temperature Profile
LaTe_{2-x}	82.00%-85.00%	1150°C→1000~975°C
CeTe_{2-x}	82.00%-86.00%	1150°C→1040~975°C

Table 3.1: Crystal growth condition for $R\text{Te}_2$ ($R=\text{La}, \text{Ce}$)

1cm \times 3cm (i.e. 2mL volume) were used. The bottom crucibles contained the elemental materials and the top crucibles were filled with clean quartz wool. During the decanting, the top quartz wool separates out the grown crystals from the remaining liquid and additional quartz wool above and below the crucibles protected the quartz tube (Figure 3.1). A drilled firebrick was used as a container in order to safely place the sealed quartz tube in the furnace during the heating and to provide an isothermal environment.

The mixtures were heated to 1150°C and slowly cooled over a period of 3-5 days to end temperatures in the range of 900-1060°C.¹ Such high temperatures are possible

¹Te boils at around 1000 °C at 1 atm

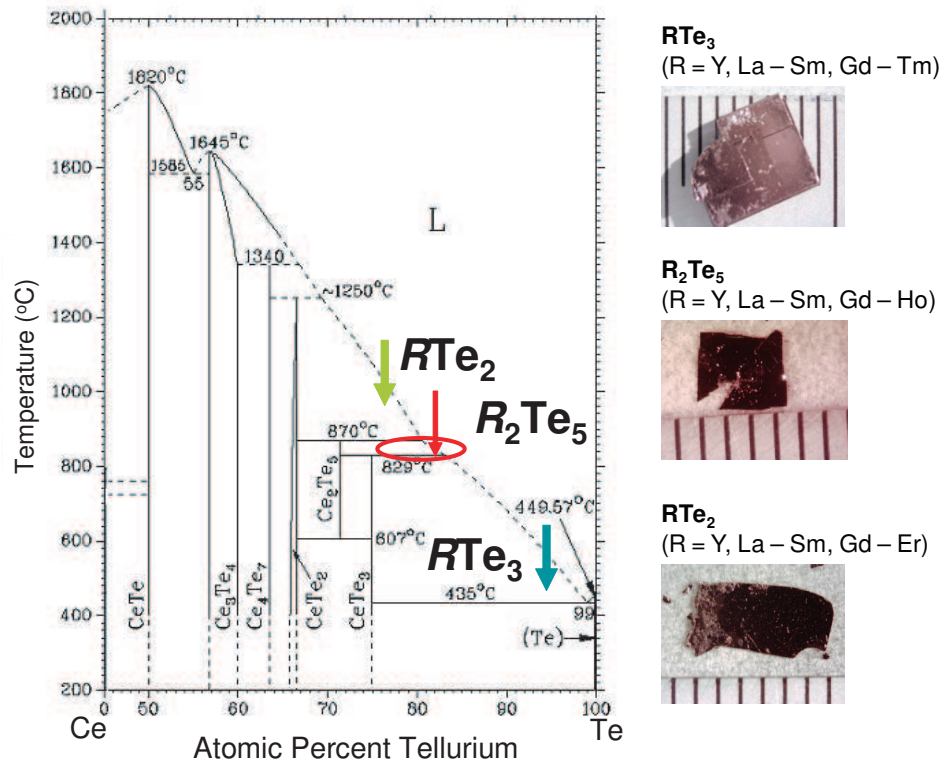


Figure 3.2: Binary Phase diagram, particularly shown for Ce-Te elements (from Masalski, [37]). Crystal growth of CeTe₂, Ce₂Te₅ and CeTe₃ is possible from a binary melt because of the exposed liquidus. Photographs of representative crystals, shown on a mm scale, are presented on the right of the diagram.

for this growth because the substantial fraction of rare earth element reduces the Te vapor pressure, but nevertheless care must be taken that the quartz tubes are well sealed. Resulting crystals were separated from the remaining melt by decanting in a centrifuge rotating up to 2000rpm. This last process must be done rapidly after removal from the furnace, even though the firebrick serves to increase the thermal inertia. After decanting in the centrifuge, the quartz tubes were allowed to cool down to room temperature upside down in the fume hood before opening. The crystals were shaped in the form of dark, shiny, somewhat brittle platelets, with dimensions up to 10mm×10mm×1mm, with the c -axis perpendicular to the plane of the crystal plates. The mass of the collected crystals were measured to provide an estimate of the liquidus phase boundary for the growth condition, which is very useful since the published R -Te phase diagrams [37] are inaccurate or even incomplete for several members of the rare earth series.

Recently, competing superconductivity state has been observed at $T_c=2.7\text{K}$ in $\text{CeTe}_{2-\delta}$, only in a sample with $\delta = 0.08$ [51]. The results indicate that the physical properties of the rare earth ditellurides strongly depend on the Te deficiency and, thus, we have made a particular effort to produce stoichiometric, or as close to stoichiometric as possible, single crystals of $R\text{Te}_{2-\delta}$. With reference again to the binary phase diagrams [37], there exists width of formation of the rare earth telluride crystals $R\text{Te}_2$ ($R=\text{La}, \text{Ce}$) and a smaller Te deficiency, δ , is possible for melts that have a larger Te content, requiring lower growth temperatures (Figure 3.2).

Composition of the resulting crystals was determined by electron microprobe analysis using elemental standards, and showed that we are able to produce stoichiometric crystals of $\text{CeTe}_{2.00}$ by this technique, with an uncertainty of ± 0.03 in the Te content.

However, all attempts to produce stoichiometric LaTe_2 failed, and the highest composition achieved by this technique was $\text{LaTe}_{1.95}$, which is only just sub-stoichiometric within the resolution of our measurements. Published data for crystals grown via the mineralization technique of Ref. [47] indicate a Te deficiency of $\delta = 0.15 - 0.18$. In comparison, the self-flux technique produces crystals with a much smaller Te deficiency $\delta = 0.00$ ($R = \text{Ce}$) - 0.05 ($R = \text{La}$). The Bridgman technique described in Ref. [48] and Ref. [49] reportedly produces stoichiometric crystals, though the high temperature used for this growth implies a larger Te deficiency than the lower temperatures that we employ. According to published work, both the alkali-halide flux [2] and chemical vapor transport [45, 46] techniques also produce crystals with a very small Te deficiency, though in general we favor a self-flux since it minimizes the possibility of contamination from additional elements.

3.1.2 Crystal Growth: $R_2\text{Te}_5$

High quality single crystals of $R_2\text{Te}_5$ ($R=\text{Nd,Sm,Gd}$) were also grown by slow cooling a binary melt. Inspection of the equilibrium binary alloy phase diagrams [37] reveals that $R_2\text{Te}_5$ has a much narrower exposed liquidus than does either $R\text{Te}_2$ or $R\text{Te}_3$, corresponding to a temperature range of less than 50°C and a melt composition that varies by less than 3 at.%. Hence, for each rare earth it has been necessary to carefully determine the precise melt composition and temperature profile to achieve the optimal growth conditions that avoid the appearance of second phases. For this reason, we have focused on just three members of the rare earth series, Nd_2Te_5 , Sm_2Te_5 and Gd_2Te_5 .

Elemental starting materials of rare earth metal (Ames MPC, 99.50% for Sm and 99.80% for Nd and Gd) and tellurium (Alfa Aesar, 99.9999%) were cut and placed in

Crystal	Melt Composition (at.%Te)	Temperature Profile
Nd ₂ Te ₅	92.50%	1050→880°C
Sm ₂ Te ₅	90.00%	1000→920°C
Gd ₂ Te ₅	92.00%	1050→900°C

Table 3.2: Optimal Crystal growth condition for R_2Te_2 (R =Nd, Sm and Gd)

alumina crucibles and sealed in evacuated quartz tubes. The ampoules were placed in a furnace and ramped to 1050°C before slowly cooling to an end temperature (Table 3.2) at which they were removed from the furnace and the remaining flux separated from the crystals by decanting in a centrifuge, as described above. The optimal melt composition and temperature profile varied even for the three closely spaced members of the rare earth series studied here, and are listed in Table 3.2. The resulting crystals were gold in color, forming thin, malleable and micaceous plates.

Single crystal X-ray diffraction was used to confirm the phase of the crystals (Figure 3.3). θ - 2θ scans along the $(0k0)$ direction revealed clear peaks for even k with the appropriate lattice parameter, for example, $b = 43.6\text{\AA}$ for Gd₂Te₅, indicating well formed single crystalline phase of R_2Te_5 . In the measurement, it was observed that some crystals showed weak RTe_3 peaks mixed with very strong R_2Te_5 peaks. The RTe_3 peaks could be reduced in magnitude or even caused to totally disappear by removing the surface layers of the crystals using adhesive tape. This thin layer of RTe_3 forms on the surface of the R_2Te_5 crystals during the rapid cooling, while the remaining melt is removed by centrifuge, and is essentially a consequence of applying this growth technique to a material with such a small exposed liquidus in the phase diagram [37].

The composition of the crystals was examined by electron microprobe analysis

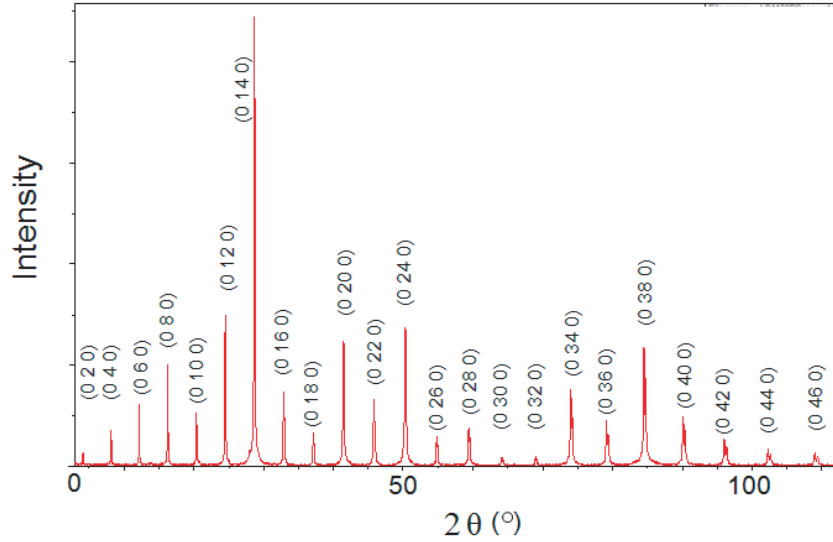


Figure 3.3: X-ray diffraction peaks from $(0k0)$ planes for Gd_2Te_5 . The peaks for $k=\text{even}$ can be indexed for $b = 43.6\text{\AA}$ and show no mixing of GdTe_3 phase in the crystal.

(EMPA), for Sm_2Te_5 and Gd_2Te_5 . In both cases, tellurium content was determined to be 72 ± 1 at.%, consistent with the value anticipated for $R_2\text{Te}_5$ ($5/7 = 71.4\%$).

3.2 Transmission Electron Microscopy

High resolution transmission electron microscopy (HRTEM) technique was used to investigate Gd_2Te_5 single crystals in real space. For HRTEM, cross-sectional TEM samples were prepared using a “sandwich method”: a small, plate-like Gd_2Te_5 single crystal ($\sim 2 \times 2 \times 0.1$ mm) was placed in between a small stack of spacers cleaved from a single crystal silicon wafer that snugly fit inside a 3mm diameter quartz tube. The open spaces were in-filled using Epoxy (EPO-TEK 353ND) to hold the stack together. A disk with a thickness about 0.5 mm was cut from the quartz tube using a diamond saw. The Gd_2Te_5 single crystal was oriented such that the b -axis lay in the plane

of the disk and the [101] direction was close to the disk normal. The disk then was ground and polished to about 30~50 μm thickness. A VCR dimpler was used to further thin the disk center area to less than 30 μm . The final thinning of the TEM sample was performed at room temperature using a Fischione Model 1010 ion-miller. The milling with an initial setting of the Ar ion guns condition started at 23°, 5 kV and 5 mA, at room temperature till perforation, then followed with 3 kV and 3 mA, 15° for 15 min, and final with 2 kV, 3 mA, 10° for 20 min. A Tecnai G² F20 STEM (point-to-point resolution: 0.25 nm) operated at 200 kV was also employed to do the microstructure investigation. High resolution TEM (HRTEM) simulation was done using the National Center Electron Microscopy simulation program which employs the multi-slice approximation. Real space images showed very few macroscopic defects, which could be easily avoided (Figure 5.1).

Selected area diffraction pattern(SADP) measurements were utilized to probe the CDW lattice modulation. For SADP measurements at room temperature, thin crystals with thickness less than 30 μm were carefully selected and mounted on copper grids. To achieve optimal thickness for the measurement, a small hole was made in the middle of the crystals by ion-milling in vacuum for 2 hours using a liquid nitrogen cooling stage which prevents the samples from being damaged by overheating. The crystals were illuminated on the edge of the hole and selected area diffraction patterns (SADPs) were obtained using a Philips CM20 FEG-TEM operating at 200kV in vacuum. The electron beam was aligned normal to the Te plane in [001] zone axis for $R\text{Te}_2$ and [010] zone axis for $R_2\text{Te}_5$. For SADP measurements at the elevated temperatures, a Philips CM 30 operating at 300keV in vacuum was used with Gatan double tilt heating stage and double copper washers were utilized to improve thermal contact. It was observed that the samples drifted due to the thermal expansions of

the sample stages, and every effort was tried to stay in the same spatial area within less than a microns apart at the most.

3.3 High Resolution X-ray Diffraction

Gd₂Te₅ single crystals sized upto 4mm×4mm×40μm were carefully selected and glued on the surface of the metallic sample stage using Leitsilber 200 silver paint from Ted Pella. High resolution X-ray diffraction measurements were carried out in a reflection geometry for photon energies 9.35keV and 12.70keV at the Stanford Synchrotron Radiation Laboratory (SSRL) on Beam Lines 11-3 and 7-2 at various temperatures. A Ge(111) crystal analyzer or either 1 or 2 milliradian slits were selected depending on the measurement alignments. The samples were kept in a helium gas flow during the entire measurements in order to minimize oxidation and the temperature was actively controlled by an Anton-Paar furnace up to 550 K. Diffraction peaks at a wide range of angles were carefully inspected in order to select regions of minimal structural defects. Samples had to be realigned at each temperature due to the thermal expansion of the sample stage and the Bragg peaks near to the satellite peaks were centered at the maximum intensities.

3.4 Thermodynamic and Transport Properties

The heat capacity of single crystal samples was measured using a relaxation time technique. Crystals with a mass of approximately 5 - 10 mg were prepared with a flat surface for good thermal contact with the sample platform. Data for LaTe_{1.95} were used to obtain estimates of the lattice and electronic contributions to the heat capacity. Similar measurements were also made for LaTe₃ single crystals for comparison.

The electrical resistivity was measured using geometric bars cut and cleaved from the larger as-grown crystals. Electrical contact was made using Dupont 4929 silver epoxy on sputtered or evaporated gold pads, with typical contact resistances of 1.0-2.5 Ω . Resistivity measurements were made at 16 Hz and with current densities of approximately 0.03 A/cm². In-plane measurements were made for arbitrary current directions along the Te plane, using a standard 4 point contact geometry. The out-of-plane resistivity was measured using a modified Montgomery geometry, with one current and one voltage contact on the top face of the plate-like crystal, and the other voltage and current contacts on the bottom face. Several measurements were made for crystals from each growth batch.

Chapter 4

Charge Density Waves in $R\text{Te}_2$ ($R=\text{La}, \text{Ce}$)

In this chapter, results are presented of complementary measurements that probe the electronic structure and charge density wave (CDW) modulation in the quasi-2D compounds $\text{LaTe}_{1.95}$ and CeTe_2 . Transmission electron micrographs show that the CDW modulation wave vectors are different for the two materials and incommensurate with the underlying lattice. These wavevectors are shown to correspond to nesting features of a simplified model of the Fermi surface. These results appear in Ref. [12]. Results of additional collaborative experiments not described in this thesis appear in Ref. [15] and Ref. [16].

4.1 Introduction

$R\text{Te}_{2-\delta}$ ($R=\text{La}, \text{Ce}, \delta = 0 \sim 0.18$) compounds have attracted recent attention due to their effective low dimensionality and the materials play host to a charge density wave (CDW) [2,52] in a nominally ‘tetragonal’ structure. Band structure calculations

for the stoichiometric material indicate a strongly anisotropic Fermi surface(FS) of mostly Te $5p$ character with minimal c-axis dispersion, large regions of which are nested [30,31]. A substantial anisotropy in the electrical resistivity confirms the quasi-2D character of the charge carriers [47, 48, 53], and a superlattice modulation of the average structure has been observed via transmission electron microscopy(TEM) [2] and x-ray diffraction [45, 46]. DiMasi et al previously showed that the modulation wave vectors can be tuned by Sb substitution in $\text{LaTe}_{2-x}\text{Sb}_x$, and that these wave vectors can be understood in terms of optimal nesting of a Fermi surface derived from simple tight-binding arguments [2]. These observations essentially establish the lattice modulation in $R\text{Te}_2$ as a CDW, driven by an electronic instability of the Fermi surface. More recently, tunneling measurements on $R\text{Te}_{2-\delta}$ for both $R = \text{La}$ and Ce clearly reveal a well developed gap, further supporting the idea of CDW formation [52]. Here the Ce is trivalent and the $4f$ states do not appear to contribute to the Fermi surface [54], ordering antiferromagnetically below 6 K [49, 55]. No clear electronic phase transitions are observed below 300 K, and the material appears to be deep in the CDW state even at room temperature, similar to the related bilayer material $R\text{Te}_3$ ($R = \text{Y}, \text{La-Sm}, \text{Gd} - \text{Er}$) [18, 33, 34]. The structural and electronic simplicity of $R\text{Te}_2$ and $R\text{Te}_3$, combined with the large size of the CDW gap, makes these particularly attractive materials for studying the effect of CDW formation on the electronic structure of layered materials. In particular, Angle Resolved Photo Emission Spectroscopy(ARPES) has enabled direct measurement of the electronic structure in the CDW state of $R\text{Te}_3$ [18, 33], and we show here that it is also possible in $R\text{Te}_2$. $R\text{Te}_{2-\delta}$ compounds have a substantial width of formation [37] corresponding to a tendency towards significant Te vacancies on the Te(1) square planar site [38, 39]. In contrast, the related bilayer rare earth tellurides $R\text{Te}_3$ form

as stoichiometric compounds without significant Te deficiency [34, 36]. Reports of transport properties for $R\text{Te}_{2-\delta}$ ($R=\text{La}, \text{Ce}, \delta = 0 \sim 0.18$) vary widely [47, 48], which presumably can be related to differences in Te deficiency between samples produced via different crystal growth techniques. Recently, pressure-induced superconductivity at $T_c = 2.7\text{K}$ has been reported in non-stoichiometric $\text{CeTe}_{1.82}$ [51]. These data indicate a possible coexistence of CDW, superconducting and antiferromagnetic phases at low temperature, though the origin of the superconductivity is as yet not clear. Similar high pressure measurements have not been made for other rare earths in this family of compounds, but the authors report that the superconductivity in $\text{CeTe}_{2-\delta}$ is very sensitive to δ [51], suggestive of an intimate link to the electronic structure and CDW modulation. In an attempt to explain the mechanism of the superconductivity, a new band structure calculation has been performed which models the effects of Te deficiency and assumes specific commensurate distortions of the host lattice [56], though as we argue below, these assumptions may be too simplistic.

In the following sections, we describe the results of TEM and ARPES measurements of single crystals of CeTe_2 and $\text{LaTe}_{1.95}$. The measurements provide complementary information about the lattice modulation and the electronic structure and Fermi surface topology for the two compounds. We have prepared the materials in single crystal form using an alternative self-flux technique, which lends itself to minimizing Te deficiency while reducing the risk of contamination by not using a separate flux or transport agent. The Ce compound is stoichiometric to within the resolution of our compositional analysis, but the La compound is found to have a small Te deficiency that is barely measurable within the resolution of the microprobe technique. Neither material exhibits a simple commensurate CDW corresponding to doubling of the unit cell (though both show wave vectors very close to this), but

rather have a complex series of incommensurate wave vectors that are different to previously published data for crystals grown by alternative techniques. The CDW distortion is different for the two compounds, which is also reflected in a more dramatic difference in the electronic structure as revealed by the ARPES measurements. Our results indicate that subtle differences, such as the choice of rare earth or relatively minor changes in Te deficiency and band filling, can substantially affect the superlattice modulation and electronic structure of $R\text{Te}_{2-\delta}$. These results imply that to understand the pressure-induced superconductivity in $\text{CeTe}_{1.82}$ will require more than a simple extrapolation from the electronic structure and CDW modulation of the stoichiometric compounds.

4.2 Experimental Results

4.2.1 Transmission Electron Microscopy

TEM samples were prepared as described in Section 3.2. SADPs taken at room temperature for $\text{LaTe}_{1.95}$ and CeTe_2 single crystals are shown in Figure 4.1. The undistorted tetragonal $P4/nmm$ structure produces strong $(hk0)$ peaks in reciprocal space where $h + k = \text{even}$ and no peaks where $h + k = \text{odd}$.

In-plane tetragonal lattice parameters obtained from the observed patterns are $a=4.55 \pm 0.02 \text{ \AA}$ for LaTe_2 and $a=4.52 \pm 0.02 \text{ \AA}$ for CeTe_2 , which agree within the uncertainty with published values of $a=4.52 \text{ \AA}$ for LaTe_2 [2] and $a=4.47 \text{ \AA}$ for CeTe_2 [55] obtained from X-ray diffraction measurements. Both diffraction patterns shown in Figure 4.1 also have faint spots at the $h + k = \text{odd}$ forbidden peak positions, the presence of which have previously been attributed to the combination of sample bending and/or stacking disorder [34]. In the case of $\text{LaTe}_{1.95}$ these additional spots also appear to be slightly split, but the origin of this effect is unclear.

Additional superlattice peaks in the SADPs for both compounds indicate the presence of a modulation from the simple Cu_2Sb structure. These patterns were reproduced for several crystals of each rare earth element. In both cases the diffraction patterns exhibit a four-fold rotational symmetry, rather than the simpler two-fold symmetry that was previously observed for nominally stoichiometric LaTe_2 [2]. No measurements showed a simple two-fold symmetry, including measurements of different sections of the same crystals, which leads us to think that this is an intrinsic symmetry of the material, although we cannot completely rule out the possibility of some kind of micro-twinning. Positions of the various satellite peaks in the first quadrant are listed in Table 4.1 for both compounds ($a^*=2\pi/a$ etc). Those in other

Crystal	α	β
LaTe _{1.95}	0.484±0.002	0.000±0.005
	0.601±0.002	0.201±0.002
CeTe _{2.00}	0.473±0.003	0.0000±0.003
	0.572±0.002	0.067±0.003
	0.715±0.002	0.035±0.003
	0.396±0.002	0.219±0.002
	0.487±0.002	0.354±0.003

Table 4.1: CDW wavevectors $\vec{q} = \alpha\vec{a}^* + \beta\vec{b}^*$, α and β in the first quadrant formed by (000), (100) and (010)

quarters are mapped by reflection and the four-fold symmetry of the lattice.

LaTe_{1.95} has the simpler diffraction pattern of the two compounds, and the lattice modulation can be characterized by two independent wavevectors after taking account of the four-fold symmetry, neither of which can be easily related to the periodicity of the underlying lattice. One of the two vectors is close but not equal to the commensurate wavevector $0.5a^*$, which would correspond to doubling the unit cell, and which was previously observed for the nominally stoichiometric LaTe₂ crystals [2] described above. The other vector was not previously observed at all (although we note that LaTe_{1.8}Sb_{0.2} was found to have a modulation wave vector $q = 0.672a^* + 0.078b^*$) [2]. The four-fold symmetry and additional modulation vectors may simply reflect the difference in Te content of crystals grown by the two techniques, or it might be related to the synthesis conditions themselves (which can affect strain, stacking order etc).

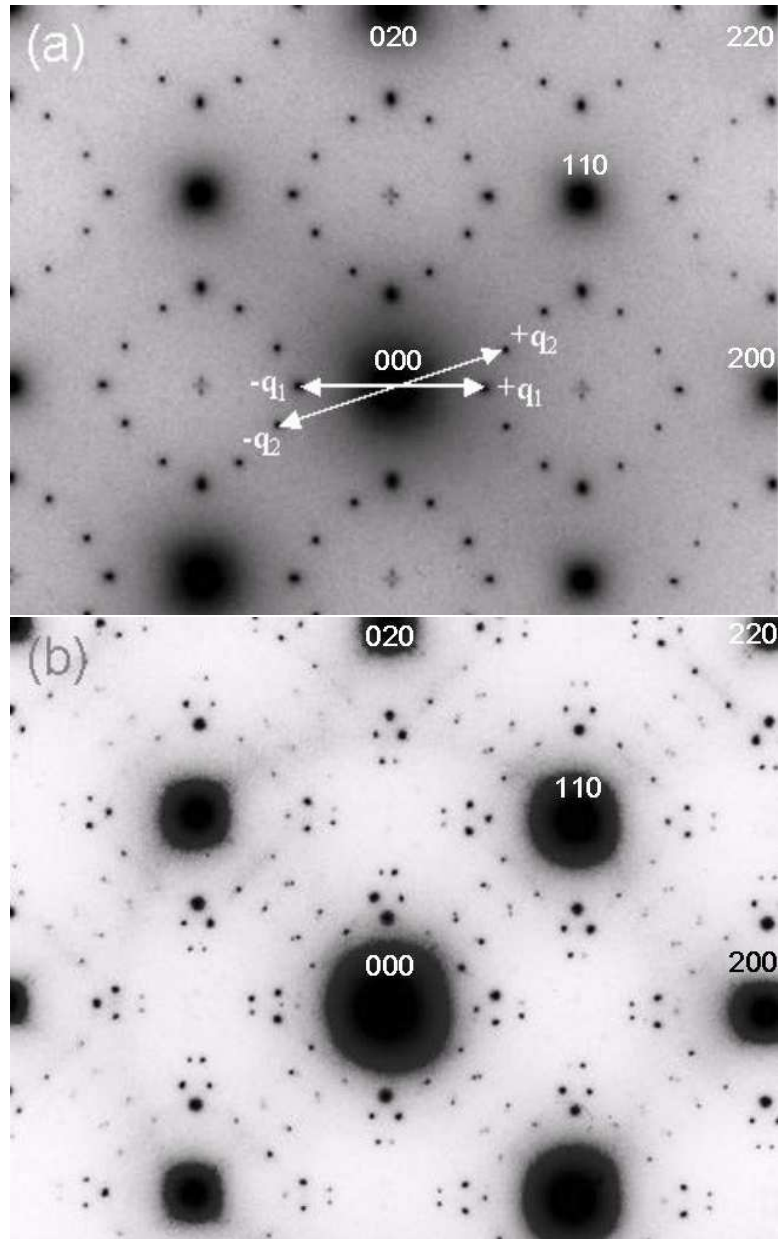


Figure 4.1: Select area diffraction patterns of (a) $\text{LaTe}_{1.95}$ and (b) CeTe_2 in $[001]$ zone axis. Most intense diffraction peaks correspond to $h + k = \text{even}$

In contrast to $\text{LaTe}_{1.95}$, the diffraction pattern for CeTe_2 is much more complex. As for $\text{LaTe}_{1.95}$, one of the observed wavevectors is close but not equal to the commensurate case of $0.5a^*$. To the best of our knowledge this is the first published TEM diffraction pattern for CeTe_2 , despite the large amount of interest that this compound has recently received. The difference between the diffraction patterns of CeTe_2 and $\text{LaTe}_{1.95}$ may be due to the difference in Te deficiency, or might be related to the subtle Lanthanide contraction. Whatever the cause, we can anticipate that the electronic structure of the two compounds will be somewhat different.

We use the simple tight binding model described in Chapter 2 to illustrate that the observed lattice modulations, at least for $\text{LaTe}_{1.95}$, can be understood in terms of the electronic structure. We do this by calculating the Lindhart susceptibility $\chi(q)$ for the same toy model of a single square-planar Te sheet, illustrated in Figure 2.3. We choose values of t_{\parallel} and t_{\perp} that give results that closely approximate more careful band calculations by Kikuchi [30], but we neglect the effect of hybridization between the p_x and p_y orbitals. The resulting tight-binding band structure and Fermi surface are shown in Figures 2.5 and 2.6 for a band-filling corresponding to stoichiometric composition ($\delta = 0$). Comparison with the results of full band calculations for undistorted LaTe_2 [30, 31] show that this model, though extremely simplistic, does in fact capture the essence of the electronic structure of $R\text{Te}_2$, reflecting the simplicity of the material. The Lindhart susceptibility calculated by summing over all bands and all energies for this model is shown as a color-scale plot in Figure 4.2(a). We have used a band filling that closely approximates the observed Fermi surface for $\text{LaTe}_{1.95}$ (corresponding to a Fermi energy $E_F = 3.1\text{eV}$; see following section), consistent with the small Te deficiency which acts to donate electrons. On the same figure we show the observed lattice modulation wave vectors for this compound taken from Table

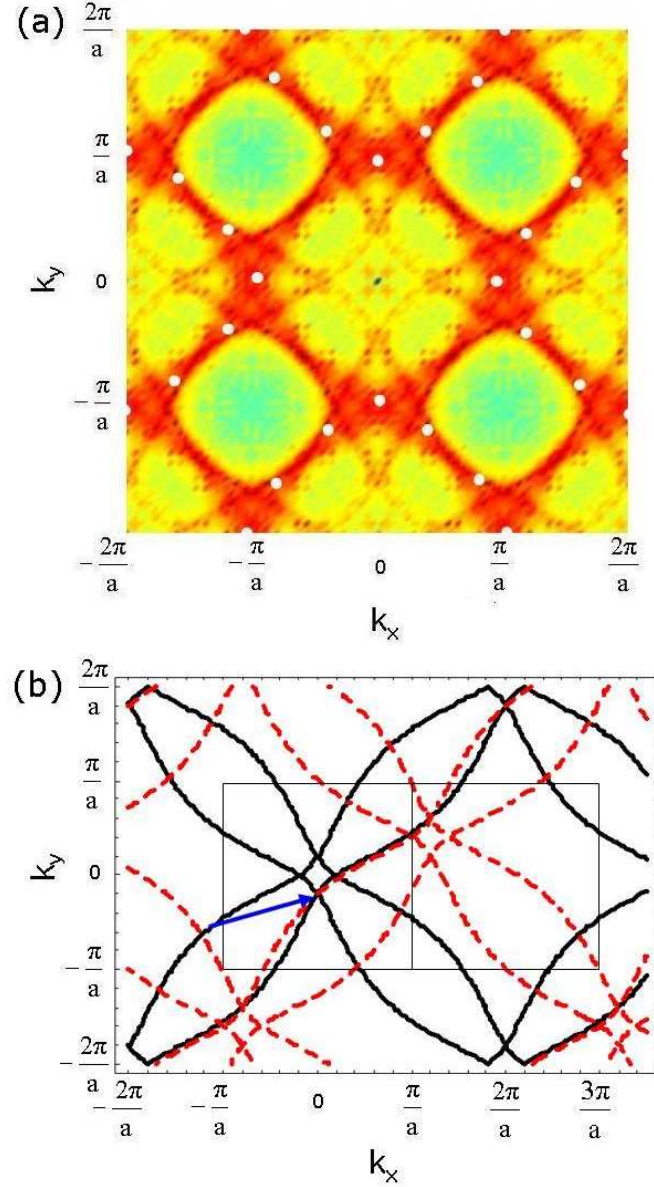


Figure 4.2: (a) Generalised susceptibility $\chi(q)$ on a color scale for the model shown in Figure 2.5 and Figure 2.6 for $E_F = 3.1$ eV (red = high, green = low). Values of q are shown from $-a^*$ to a^* . The observed lattice modulation vectors for $\text{LaTe}_{1.95}$ are shown as white spots. (b) Fermi surface for the same band filling (solid lines), showing CDW replica (dashed lines) translated by $q_{CDW} = (0.601a^*, 0.201a^*)$, indicated by arrow.

4.1. It is clear from Figure 4.2(a) that $\chi(q)$ does not have a simple single peak corresponding to $q = 0.5a^*$, but rather has a tendency to have a range of maxima corresponding to nesting of different regions of the Fermi surface.¹ Even so, the observed lattice modulation vectors for $\text{LaTe}_{1.95}$ certainly lie in regions of Figure 4.2(a) for which $\chi(q)$ has a large value. For comparison, in Figure 4.2(b) we show the Fermi surface corresponding to this particular band filling together with a CDW replica that has been translated by $q_{CDW} = (0.601a^*, 0.201a^*)$, one of the two wave vectors observed for $\text{LaTe}_{1.95}$. As can be seen, this wave vector almost nests an extended region of the model Fermi surface, which would presumably be the driving force for the resulting lattice modulation. Although this model clearly lacks a number of details which can be very significant in determining finer behavior of $\chi(q)$, the calculation is useful in that it suggests that this quantity does not have a simple single peak, and that relatively subtle effects may therefore favor one wave vector over another. This is in direct contrast to $R\text{Te}_3$, for which a similar calculation reveals a very well defined maximum in $\chi(q)$ [35]. Since the nesting wave vector is so much better defined in $R\text{Te}_3$ than $R\text{Te}_2$, the resulting charge density wave is also much more stable against perturbation, changing only modestly in magnitude across the entire rare earth series [34].

4.2.2 ARPES

ARPES experiments were performed by V. Brouet in collaboration with the author. Results are included here since they contribute to our understanding of CDW formation in these materials. ARPES data were collected at 25K on BL 10 of the Advanced

¹This behavior is directly linked to the curvature of the bands at the given band filling. E_F in $R\text{Te}_2$ is larger than in $R\text{Te}_3$ (Figure 2.5) and the Fermi level is closer to the top of the conduction bands, where small changes in q cause the sections of the FS to deviate from the optimal nesting more significantly.

Light Source, with the beam polarization nearly perpendicular to the sample surface, photon energy between 30 eV and 50 eV, and an energy resolution of ~ 20 meV. $R\text{Te}_2$ does not cleave as easily as $R\text{Te}_3$. In $R\text{Te}_3$, the natural cleavage plane is between Te layers, which reveals the Te sheets, whereas in $R\text{Te}_2$ it is most likely between Te layers and the $R\text{Te}$ slab, giving only a 50% chance to observe directly the Te sheets. Samples were glued with Torr-Seal epoxy and electrically connected to the ground by graphite. No electrical charging of the sample surface occur in these conditions during the measurement.

Figure 4.3 displays Fermi surfaces of $\text{LaTe}_{1.95}$ and CeTe_2 measured by ARPES at photon energies of 30 and 52 eV respectively. These maps were obtained by integration of the spectral weight between $E_F - 50$ meV and $E_F + 50$ meV and data were symmetrized with respect to $x=2$ and $y=0$ (except for CeTe_2 in the first BZ). We have checked that the different photon energy and data symmetrization do not change the qualitative features of these maps. Similar results were reproduced in another $\text{LaTe}_{1.95}$ sample and three other CeTe_2 samples.

The regions of high intensity in Figure 4.3 correspond to places where Te p_x and p_y bands approach the Fermi level (either crossing it or leaving a small gap). As described in the previous section, and also found for $R\text{Te}_3$ [18, 33], there are two different pieces of FS : a small square centered at Γ (referred to as the *inner* FS) and a larger square centered at $(2,0)$ and equivalent points that we will call the *outer* FS in the following discussion. The small *inner* square does not appear on Figure 4.3 because it is entirely gapped, as will be discussed later. The *outer* FS is folded in the first BZ (parts of these reflections are clearly seen in $\text{LaTe}_{1.95}$) but with a weaker intensity that sometimes makes it undetectable (for details, see Ref. [18]). Comparison with Figure 2.6 shows that this FS is in total agreement with the simple

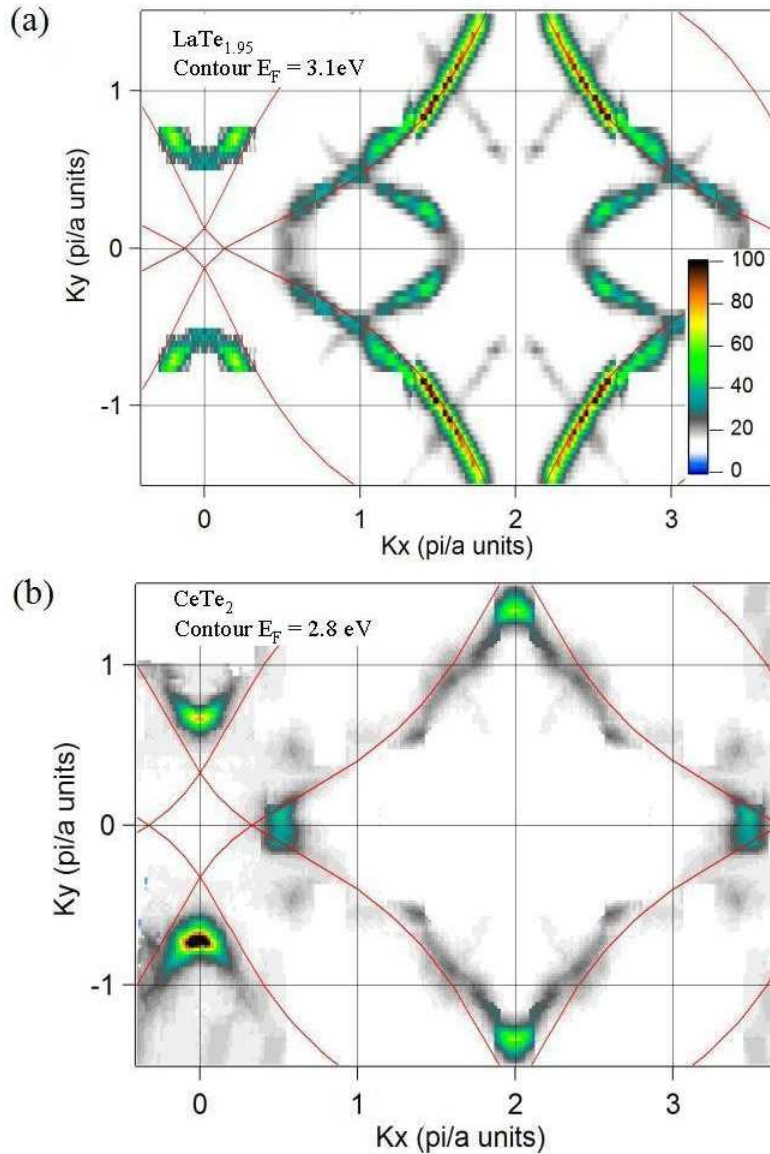


Figure 4.3: ARPES data at $T=20\text{K}$ showing the Fermi surface of (a) $\text{LaTe}_{1.95}$ with $h\nu=30\text{ eV}$ and (b) CeTe_2 with $h\nu=52\text{ eV}$, obtained by integration of the electronic structure in a 100 meV window around E_F (see text). Red lines show results of the tight binding model described in section 4.2.1 for the given Fermi energies in the extended zone scheme.

tight-binding model based only on Te bands presented in the previous section. In addition, we note that we do not observe a small pocket around Γ which was predicted in some calculations to be formed by La $5d$ bands [45].

In this simple tight binding approach, the size of the *outer* FS is simply determined by the position of the Fermi level, i.e. the band filling. In the absence of Te deficiency, the band filling is expected to be the same for all rare earth members of the series, as we have previously found for the tritelluride $R\text{Te}_3$ [35]. In contrast, for the ditellurides we find that the size of the *outer* FS appears significantly larger in $\text{LaTe}_{1.95}$ compared to CeTe_2 . Qualitatively, the larger *outer* FS in $\text{LaTe}_{1.95}$ is consistent with the presence of Te vacancies, which would increase the average number of electrons per Te (see Figures 2.3, 2.5 and 2.6). If n is the number of electrons in p_x and p_y orbitals (we assume that p_z is filled), one expects $n=3$ for stoichiometric $R\text{Te}_2$ from which $E_F = 2.8\text{eV}$. Quantitatively, the best fit of the data to the tight binding model for $\text{LaTe}_{1.95}$ is indicated in Figure 4.3 by the red lines, and gives $E_F = 3.1 \text{ eV} \pm 0.1\text{eV}$, from which we obtain $n = 3.1 \pm 0.07$. Within an ionic picture, the finding of $n > 3$ can be explained by the charge transfer from a small number of vacancies $\delta = 0.1 \pm 0.05$, consistent with the measured value of $\delta = 0.05 \pm 0.03$. In CeTe_2 , the fitting is less accurate because a large part of the *outer* FS is gapped (as will be discussed below) and the intensity is concentrated at the corners, where the real data deviates from the tight binding model (these corners are rounded by the interaction between p_x and p_y that was neglected in the calculation) [18]. Therefore, we just show the theoretical contour for $E_F = 2.8\text{eV}$, which appears correct or slightly too large, demonstrating the contrast with $\text{LaTe}_{1.95}$. This also implies that we can find the right size of FS by completely neglecting the contribution of Ce electrons, which requires a negligible coupling between Te and Ce electrons (a significant hybridization with Ce $4f$, Ce $5d$ or Te p_z electrons would all

result in a *larger* size of *outer* FS, inconsistent with our data).

The other important information that one can extract from the ARPES data is the size and location of the CDW gap. A lower intensity on the FS map is usually correlated with a gap opening, which partially or totally removes the bands from the integration window around E_F . However, it is necessary to check simultaneously the gap opening on a map of the measurement of the full electronic structure as a function of energy, because ARPES intensity is modulated by matrix-element effects that can introduce extrinsic intensity variations. For example, the intensity appears stronger for both maps in the upper part of the *outer* FS ($k_y > 0.5$), but this is a change of the whole band intensity, the band dispersion and shape at E_F remain the same. Similarly, the intensities at the different corners of the CeTe_2 map are slightly different but they all correspond to Fermi level crossings of bands with different absolute intensities.

As already mentioned, the small *inner* Fermi surface centered at the Γ point is not visible in either map, and inspection of the full electronic structure reveals a very large gap in both cases with $E_g=600\text{meV}$, nearly twice larger than in $R\text{Te}_3$, indicating a very strong coupling for the CDW. Another similarity between the two maps is their 4-fold symmetry (except for the extrinsic changes in intensity already discussed). This is at variance with $R\text{Te}_3$, for which the gap opens along one direction only, giving very different FS along k_x and k_y . This could be expected from the TEM patterns presented in section 4.2.1, which show coexistence of satellites in k_x and k_y direction, contrary to those in $R\text{Te}_3$, which have 2-fold symmetries.

The intensity along the *outer* FS is generally much larger than in the inner square, which indicates no gap or a much smaller gap, and the distribution of this intensity is dramatically different in the two compounds. In $\text{LaTe}_{1.95}$, most of the outer part is

ungapped and a small gap $E_g=100\text{meV}$ opens only at the corners (where the intensity is reduced in the map, it is clearly visible along k_x and, for the folded FS, along k_y). The contrary is observed in CeTe_2 , where the spectral weight is highest on the corners, with no gap, whereas in other regions there is a small gap $E_g=100\text{meV}$. This is again at variance with $R\text{Te}_3$, for which the gap decreases rapidly and monotonically from its maximum value to zero [18].

These extended regions of small/null gaps exist because of imperfect nesting of the FS, even when there is a very large CDW coupling as is the case here. Figure 4.2 (b) indicates a typical situation giving an approximate but not perfect nesting for a sizable part of the *outer* FS. This is in contrast with $R\text{Te}_3$ for which there is a well defined maximum in $\chi(q)$ and consequently regions of the Fermi surface are either very well nested or very poorly nested [35]. Not surprisingly, we observe that the more complicated nesting properties of $R\text{Te}_2$ directly yield more complicated FS topologies that become highly sensitive to changes of the CDW structure.

In principle, the size of the gap along the FS could be calculated from the combined knowledge of the CDW wave vectors and the shape of the original FS. This becomes quite complex here, because of the coexistence of many different CDW satellites. In many regions of the *outer* FS of both compounds, we observe a large gap similar to the one of the square (600 meV) coexisting with intensity near the Fermi level, suggesting domains with different CDW orientations and/or a complex super-structure of the CDW. It is therefore difficult to tell how many carriers are involved in the reconstructed FS. Nevertheless, ARPES firmly establishes that the incommensurate CDW is the driving force to shape the FS and predicts that any residual metallic properties associated with the ungapped regions of the FS will be highly sensitive to the details of the CDW structure. From the larger ungapped section of the FS

in $\text{LaTe}_{1.95}$, one can anticipate better metallic properties for this compound than for CeTe_2 , but it is necessary to rely on complementary measurements, such as heat capacity and resistivity, to characterize the nature of the electronic properties.²

4.2.3 Heat Capacity

The heat capacity of $\text{LaTe}_{1.95}$ is shown in Figure 4.4. That of CeTe_2 is dominated by the magnetic contribution at low temperatures, and has been discussed elsewhere [55, 58]. For comparison, we include similar data for LaTe_3 in Figure 4.4 (a). By 300 K, the heat capacity of both compounds has risen to approximately the Dulong-Petit value of $3R$ per mole of atoms. Below 5 K, C/T vs T^2 follows a straight line for both materials, and linear fits result in estimates for the electronic contribution to the heat capacity (y-axis intercept) of $\gamma = 0.3 \pm 0.06$ mJ/molK² for $\text{LaTe}_{1.95}$ and 1.1 ± 0.04 mJ/molK² for LaTe_3 . CDW formation in LaTe_3 does not gap the entire Fermi surface [18, 33], and based on the above estimate of γ the ungapped regions clearly contribute a reasonable density of states, consistent with the observation of metallic resistivity for this compound [17, 36, 59].

In comparison, the electronic contribution to the heat capacity in $\text{LaTe}_{1.95}$ is significantly smaller than in LaTe_3 . The measured value of $\gamma=0.3$ mJ/molK² corresponds to a DOS of approximately 0.13 [states/eV/f.u.]. This value is much smaller than the calculated value of 0.63 [states/eV/f.u.] obtained from first principle band structure

²Recent ARPES experiments from D. Garcia *et al.* [57] for LaTe_2 samples prepared by a different technique indicate the possibility of a small gap extending over the entire FS. Our own measurements, and additional optical conductivity results [15, 16] indicate this not to be the case for the crystals described in this thesis. The difference between these observations can presumably be attributed to differences in the Te deficiency of the samples. Samples used by D. Garcia *et al.* were prepared from a mineralization technique, in contrast to our slow cooling method (see Section 3.1.1).

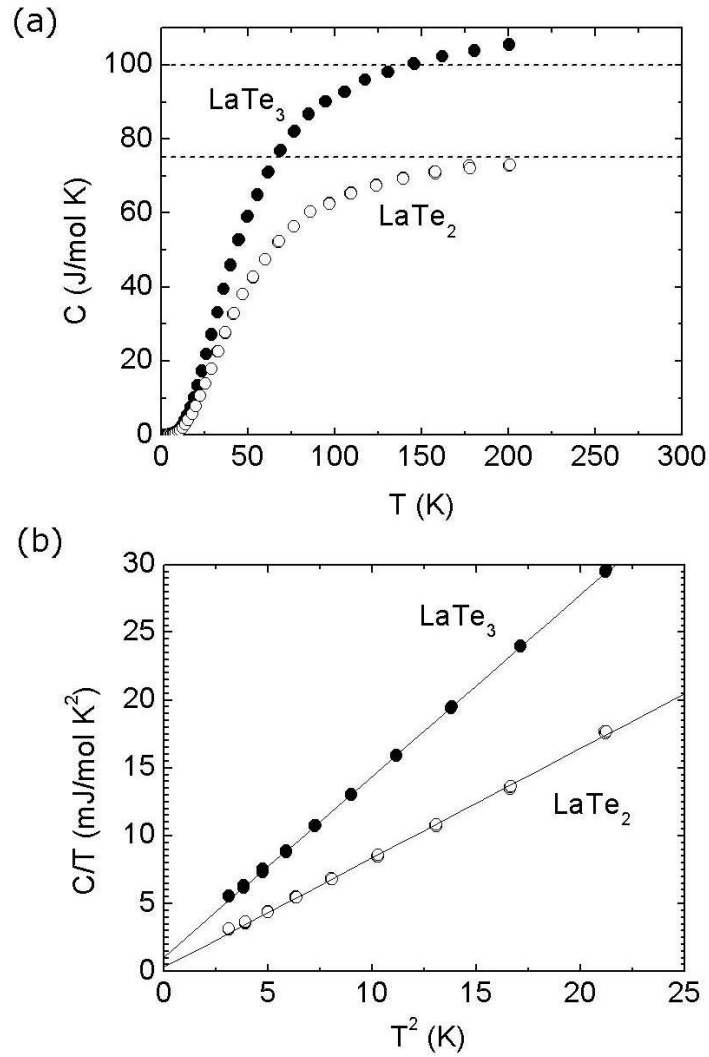


Figure 4.4: (a) Heat capacity of $\text{LaTe}_{1.95}$ (open symbols) and LaTe_3 (solid symbols). Dashed lines show the Dulong-Petit limit corresponding to $3R$ per mol of atoms. (b) Same data at low temperatures shown as C/T vs T^2 . Lines show linear fit. Mol refers to one formula unit.

calculation for the unmodulated structure of LaTe_2 [31,60], indicating that a substantial proportion of the Fermi surface has been gapped by the CDW. This picture is confirmed by electrical resistivity measurements in the following section, which show that $\text{LaTe}_{1.95}$ is far from being a good metal.

4.2.4 Resistivity

The temperature dependence of the electrical resistivity of the single crystal $\text{LaTe}_{1.95}$ and CeTe_2 samples are shown in Figures 4.5(a) and (b) respectively. The resistivity for both materials shows a strong anisotropy between the measurements in the ab -plane (ρ_{ab}) and along the c -axis (ρ_c), consistent with the layered crystal structure and with previous measurements [47,48,53]. At base temperature we find that ρ_c/ρ_{ab} is in the range of 50 ($\text{LaTe}_{1.95}$) to 100 (CeTe_2). The temperature dependence of the resistivity is rather complicated, reminiscent of either a doped small-gap semiconductor or possibly a semimetal, and is certainly far from that of a good metal. Likewise, the absolute value of the resistivity at base temperature is rather high, approximately 2 m Ω cm for currents flowing in the ab -plane. This is in contrast to the related bilayer material $R\text{Te}_3$, which exhibits very good metallic behavior associated with ungapped regions of the Fermi surface and a residual resistivity of only a few $\mu\Omega$ cm [18,36,59].

An additional feature of the resistivity of this material is that there is a sizable variation between crystals, even between samples taken from the same growth batch. For instance, the in-plane resistivity of $\text{LaTe}_{1.95}$ (Figure 7(a) left axis) shows semiconducting behavior at low temperatures for all samples, but at higher temperatures the slope of the resistivity is more variable - two extreme cases are shown. A similar range of behavior is observed for CeTe_2 . Representative data are shown in Figure 4.5(b) for crystals taken from two different growth conditions, corresponding to initial melt

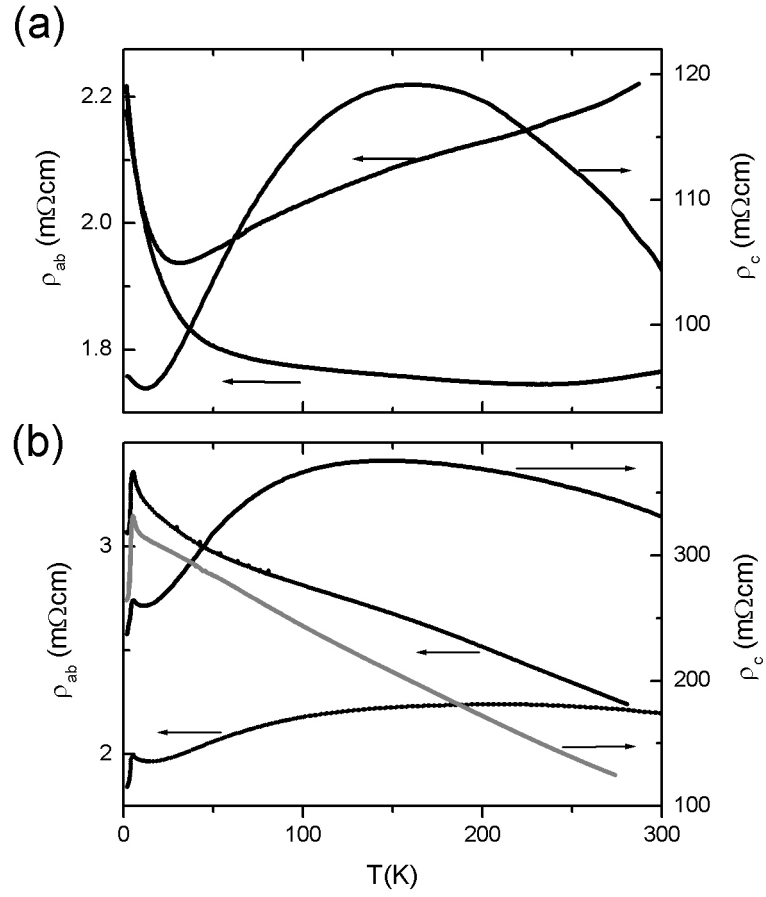


Figure 4.5: Representative resistivity data for (a) $\text{LaTe}_{1.95}$ and (b) CeTe_2 showing ρ_{ab} (left axis) and ρ_c (right axis). Data for $\text{LaTe}_{1.95}$ were taken for crystals from the same growth batch. Data for CeTe_2 are shown for crystals from two different growth batches (grey and black lines; see main text).

compositions of $\text{Ce}_{0.15}\text{Te}_{0.85}$ (black lines) and $\text{Ce}_{0.18}\text{Te}_{0.82}$ (grey lines). Both types of temperature dependence have been previously described in the published literature for this material [47, 48, 53]. This variation is presumably associated with subtle differences in Te content. Certainly our measurements imply that one should be careful reading too much in to the exact temperature dependence of any one particular resistivity curve for this material. In contrast, we find that there is no sample-to-sample variation in the resistivity of $R\text{Te}_3$, consistent both with the absence of Te deficiency in this compound and also with the more strongly metallic nature of the material.

Finally, we note that CeTe_2 samples have a sharp feature in the resistivity below 6 K, which is associated with magnetic ordering of the local 4f electrons. Neither the temperature of this feature, nor any other thermodynamic property associated with the magnetic ordering (susceptibility or heat capacity) show any sample-to-sample variation [35]. Hence, the magnetic properties of this material appear to be rather insensitive to the exact degree of Te deficiency.

4.3 Discussion

Despite considerable interest in the magnetic and electronic properties of $R\text{Te}_{2-\delta}$, few attempts have been made to determine the full crystal structure incorporating the effects of the lattice modulation. Experiments by DiMasi and coworkers, using crystals grown from an alkali-halide flux, indicated a $(2\times 1\times 1)$ supercell for LaTe_2 [2]. Subsequently Stowe, using crystals grown via chemical vapor transport, suggested $(2\times 2\times 1)$ and $(2\times 2\times 2)$ supercells for LaTe_2 and CeTe_2 respectively [45, 46]. Our own experiments, using crystals grown via a self-flux, indicate that the modulation is not precisely commensurate with the lattice for either compound. These differences between crystals grown via different methods are likely real, and reflect the fact that the synthesis technique can affect both Te content and other extrinsic parameters such as strain. DiMasi has already shown that the CDW distortion is sensitive to band filling by varying the Sb content in $\text{LaTe}_{2-x}\text{Sb}_x$ [2], and our data strongly suggest that Te vacancies will also affect the CDW. Our first conclusion is therefore that the lattice modulation in $R\text{Te}_{2-\delta}$ is very sensitive to subtle extrinsic effects, including small differences in Te content or differences induced by the change in rare earth element.

Our model tight-binding calculation indicates that the observed modulation wave vectors in $\text{LaTe}_{1.95}$ and CeTe_2 can be related to nesting conditions of the Fermi surface. Calculations of $\chi(q)$ for this model Fermi surface do not show a single peak, but rather a series of broad maxima, along which the observed modulation wavevectors are found to lie. Presumably details of the real electronic structure associated with Te deficiency, strain and the choice of rare earth, will favor certain specific modulation wavevectors, consistent with the above conclusion.

ARPES measurements clearly show that large portions of the Fermi surface of both

$\text{LaTe}_{1.95}$ and CeTe_2 are gapped. The maximum value of the gap is very large, around 600meV in both cases, implying strong electron-phonon coupling. However, most regions of the FS exhibit a smaller gap of approximately 100 meV, characteristic of imperfect nesting. The position of these regions with small gaps will be very sensitive to details of the CDW and they are consequently found to be quite different for CeTe_2 and $\text{LaTe}_{1.95}$, in good agreement with the different CDW structure already revealed by TEM. This situation is clearly more complex than for $R\text{Te}_3$, for which there is a well defined unidirectional CDW wave vector that does not change significantly all the way across the rare earth series [34]. Nevertheless, it is clear from this measurement that the ditellurides are not homogeneously gapped and cannot be considered as simple insulators.

How do the ungapped regions of Fermi surface contribute to the conductivity? This is not a simple question to answer, but we can make a few observations. It is clear from heat capacity measurements that a significantly larger portion of the Fermi surface has been gapped for $\text{LaTe}_{1.95}$ than for LaTe_3 . At first sight, this appears to contradict the ARPES data, which suggest a rather large residual FS, at least in $\text{LaTe}_{1.95}$ (in CeTe_2 , the FS pockets are certainly very small). However, as we have explained, care must be taken in the interpretation of this FS, because we observe in our data *coexistence* of gaps of different magnitude at the same positions in k-space, so that it is not straightforward to tell how many carriers contribute to the reconstructed FS. These multiple gaps can be associated with the multiple CDW satellites observed by TEM. This situation is considerably more complex than the case of $R\text{Te}_3$, for which the homogeneous behavior of the CDW gap made determination of the reconstructed FS unambiguous [18]. The presence of only a very small number of carriers in the reconstructed bands near E_F would reconcile ARPES measurements with the bad

metallicity observed by heat capacity and electrical conductivity. Furthermore, since there is a large distribution of small amplitude gaps, we cannot rule out the possibility that there might be, on parts of the remaining FS, a gap smaller than the experimental resolution (about 10meV) that would subtract yet more carriers. Given this low carrier concentration, it is understandable that resistivity data for both compounds are far from those of a good metal, in clear contrast to the tritellurides. Moreover, the CDW gap itself is substantially larger in $\text{LaTe}_{1.95}$ (~ 600 meV) than for LaTe_3 (~ 300 meV), implying a significant electron-phonon coupling even for the remaining ungapped regions of the FS. Finally, we note that there is substantial disorder in $\text{LaTe}_{1.95}$ arising from the Te vacancies - an effect all but absent in the stoichiometric tritelluride compound LaTe_3 . Taken together these observations imply that polaronic and / or localization effects may also play a significant role in substantially reducing the conductivity of this material.

4.4 Conclusion

In summary, we have described an alternative self-flux technique to grow single crystals of $R\text{Te}_{2-\delta}$ which results in samples with very small Te deficiency ($\delta = 0.00$ and 0.05 for $R = \text{Ce}$ and La respectively). TEM measurements show that the lattice modulation is different for the two materials, and that in both cases it is incommensurate with the underlying lattice. The CDW distortion is different to previously published structures for crystals produced by different techniques, indicating that the lattice modulation is very sensitive to subtle differences caused by either varying the rare earth or changing the Te deficiency. ARPES measurements indicate that large regions of the Fermi surface are gapped for both compounds, consistent with description of

the lattice modulation in terms of CDW formation driven by Fermi surface nesting. The gap varies around the Fermi surface differently for the two compounds, reflecting the difference in lattice distortion. Heat capacity measurements for $R = \text{La}$ indicate that the material has a very small density of states at the Fermi level, and resistivity measurements for both compounds show that they are far from being good metals.

³ Given this background, it is perhaps all the more surprising to find that $\text{CeTe}_{1.82}$ superconducts under pressure [51]. Our observations show that the nesting wave vectors are somewhat poorly defined for this material, and as such the CDW is rather sensitive to perturbation, for example from tellurium vacancies, at least in comparison to the related tritellurides $R\text{Te}_3$. It remains to be seen exactly how pressure affects the electronic structure and CDW modulation of this material, but our observations suggest that the CDW will be very sensitive to such external changes. Certainly the substantial CDW gap at ambient pressure implies that there is the potential for a sizable electron-phonon coupling, a key ingredient for conventional superconductivity.

³Subsequent optical conductivity experiments performed in collaboration with M. Lavagnini *et al.* [15, 16] demonstrated that LaTe_2 is indeed metallic in the CDW state, but with a significantly reduced number of carriers in comparison to the ungapped normal state.

Chapter 5

Charge Density Waves in $R_2\text{Te}_5$ ($R=\text{Nd, Sm, Gd}$)

The rare earth (R) tellurides $R_2\text{Te}_5$ have a crystal structure intermediate between that of $R\text{Te}_2$ and $R\text{Te}_3$, and we have successfully grown single crystals of the representative compounds Nd_2Te_5 , Sm_2Te_5 and Gd_2Te_5 from a self flux. In this chapter, I describe the first evidence for charge density wave formation in these materials. The superlattice patterns for all three compounds are relatively complex, consisting at room temperature of at least two independent wavevectors. Consideration of the electronic structure indicates that to a large extent these wavevectors are separately associated with sheets of the Fermi surface which are principally derived from the single and double Te layers. These results appear in Ref. [13]. Results of additional collaborative experiments not described in this thesis appear in Ref. [5].

5.1 Introduction

The electronic structure for RTe_2 and RTe_3 (R =rare earth elements) is especially simple, being determined by Te p_x and p_y orbitals in the nominally square Te planar layers [31]. In the case of RTe_3 , the quasi-2D electronic structure results in a sharp peak in the general susceptibility, $\chi(q)$ [26, 29, 31], which drives the CDW formation with T_c values depending sensitively on R due to the lanthanide contraction [17, 61]. In contrast, the maximum in $\chi(q)$ for the related single layer compounds RTe_2 ($R = La, Ce$) is less well defined (Figure 4.2), and the resulting superlattice modulation varies between rare earths as shown in Chapter 4.

The title compound R_2Te_5 has an orthorhombic structure (Cmcm) as illustrated in Figure 2.2.¹ The material is intermediate between the two better-known families RTe_2 and RTe_3 described above, consisting of alternating single and double Te layers, separated by the same RTe blocks (Figure 2.2). As shown in Figure 2.7, the electronic structure of this material is reminiscent of the single and double layer variants, essentially comprising sheets associated with each of the Te layers separately. The existence of this compound raises the question of whether separate modulation wavevectors might exist on the single and double Te planes separately, and if so how these wavevectors might interact or compete with each other.

Although crystals of R_2Te_5 have previously been grown from an alkali halide flux and their average structure reported [36], to date no superlattice modulation has been identified for this material. In this chapter, we describe the results of transmission electron microscopy (TEM) experiments on single crystals of Nd_2Te_5 , Sm_2Te_5 and Gd_2Te_5 grown from a self flux, as described in section 3.1.2. We find

¹Note that for this space group setting, the long b axis is *perpendicular* to the Te planes, while the shorter a and c lattice parameters lie in the Te planes and are almost equal in length [62].

that all three compounds exhibit a modulation wavevector oriented along the c^* axis with a magnitude close ($R=\text{Nd,Gd}$) or equal ($R=\text{Sm}$) to $(2/3)c^*$, similar to that of the tritelluride compounds. In addition, each compound exhibits at least one further set of superlattice peaks oriented away from the c^* axis. Calculations of the Lindhard susceptibility show that contributions to $\chi(\vec{q})$ enhancements arise from sections of the Fermi surface associated separately with the single and double Te planes and indicate that these different wavevectors, at least for $R=\text{Sm}$ and Gd , originate from CDW formation in the double and single Te planes respectively.

5.2 Experimental Results: TEM

A high resolution TEM image of Gd_2Te_5 at room temperature is shown in Figure 5.1. Large crystalline regions were separated by residual flux inclusions that appears continuous along the micaceous planes. Nonetheless, the HRTEM image of the Gd_2Te_5 single crystal show a highly perfect crystal structure over a large area ($\sim 400 \text{ nm}^2$, Figure 5.1). Image matching to the simulations of the $[101]$ image (Figure 2.2) suggest that the isolated bright spots are columns of Te atoms which make up the single and double layers of Te planes along the c -axis direction. The elongated bright dumbbell features are the Gd-Te pairs in the Gd-Te block layers.

Electron beam diffraction was also measured at room temperature using a Philips CM20 FEG-TEM operating at 200kV in vacuum in order to determine the ac -plane modulation structure in k space. All three compounds studied exhibit a complex set of superlattice peaks in the ac plane (Figure 5.2). As previously observed in other families of rare earth tellurides, the satellite peaks in the quadrant defined by the Bragg peaks for $h + l = \text{even}$ translate equivalently by reciprocal lattice wavevectors

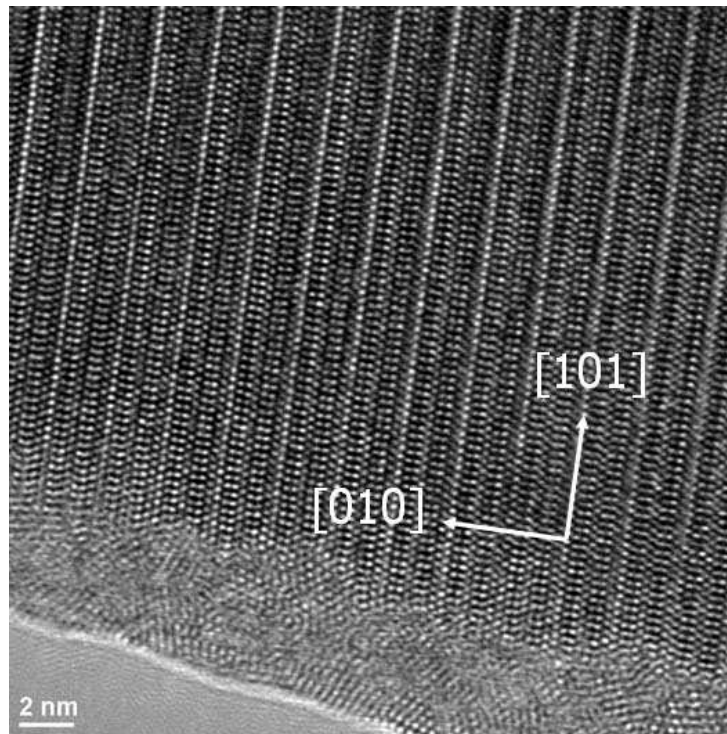


Figure 5.1: High resolution TEM image of Gd_2Te_5 at room temperature looking down the $[101]$ direction. The image shows regular crystal structure over a macroscopic length scale (more than 25nm) without intercalation or stacking faults in the layering along the b -direction.

Crystal	Q	α	β
Nd ₂ Te ₅	q ₀ (on-axis)	0.000±0.003	0.688±0.002
	q ₁ (off-axis)	0.366±0.003	0.269±0.003
	q ₂ (off-axis)	0.269±0.003	0.366±0.003
Sm ₂ Te ₅	q ₀ (on-axis)	0.000±0.004	0.667±0.004
	q ₁ (off-axis)	0.521±0.004	0.000±0.003
Gd ₂ Te ₅	q ₀ (on-axis)	0.0000±0.003	0.6871±0.002
	q ₁ (off-axis)	0.417±0.003	0.083±0.003
	q ₂ (off-axis)	0.083±0.003	0.417±0.003

Table 5.1: CDW wavevectors $\vec{q} = \alpha\vec{a}^* + \beta\vec{c}^*$.

$\vec{G} = (h, k, l)$, $h + l = \text{even}$ [2, 12, 34, 36, 63]. The relative satellite peak positions in the first quadrant are listed in Table 5.1 in units of the reciprocal lattice parameters.

The SADPs for Nd₂Te₅, Sm₂Te₅ and Gd₂Te₅ are all different, but nevertheless have some common features. In particular, all three compounds exhibit an ‘on-axis’ superlattice reflection \vec{q}_0 oriented along either the a^* or c^* direction. Within the resolution of TEM, we cannot distinguish a and c lattice parameters. However, high resolution X-ray diffraction on Gd₂Te₅ (see section 6.2.2) indicates that \vec{q}_0 is, in fact, oriented along the c^* direction [64]. For simplicity, we have also listed this lattice modulation as being along c^* for Nd₂Te₅ and Sm₂Te₅ in Table 5.1, although this remains to be confirmed. This on-axis modulation wavevector is incommensurate for Nd₂Te₅ and Gd₂Te₅ with $\vec{q}_0 = 0.688 \vec{c}^*$ and $0.687 \vec{c}^*$ for the two compounds respectively (Figure 5.2(a),(c)). In contrast, the on-axis wavevector for Sm₂Te₅ is commensurate within the resolution of the measurement, with $\vec{q}_0 = 0.667\vec{c}^* = (2/3)\vec{c}^*$ (Figure 5.2(b)).

In addition to the on-axis CDW, each of the compounds has a distinct and unique

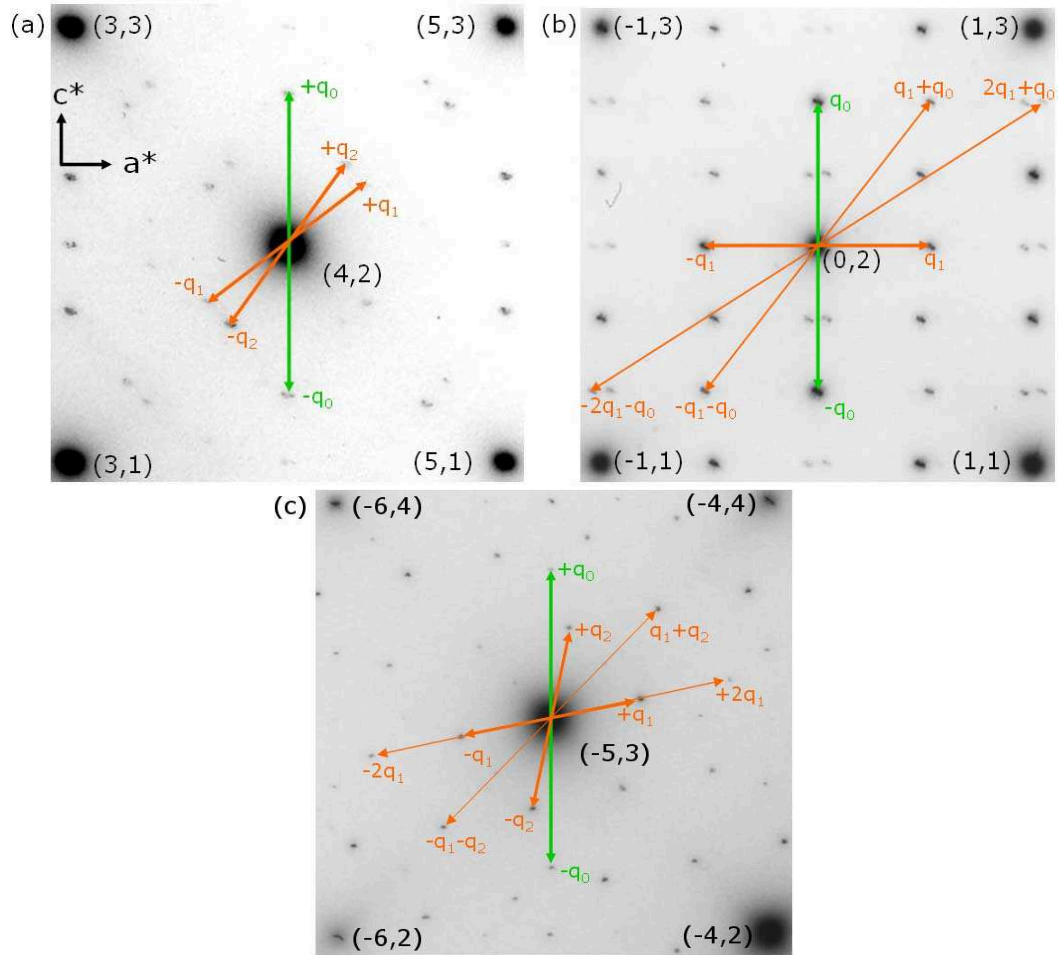


Figure 5.2: SADPs along (010) zone axis at room temperature for (a) Nd_2Te_5 (b) Sm_2Te_5 , and (c) Gd_2Te_5 . Bragg peaks are labeled by (hl) . Systematic modulation wavevectors are listed in Table 5.1.

off-axis CDW structure.

Neglecting the small difference in a and c lattice parameters, which is below the resolution of this measurement, the off-axis CDW in Nd_2Te_5 seems to have four fold rotational symmetry and the lattice modulation can be simply characterized by a single wavevector \vec{q}_1 . The second equivalent wavevector \vec{q}_2 is generated by reflection symmetry about the a^* and c^* axes. Similar symmetry mapping has been reported for the off-axis superlattice peak $\vec{q} = 0.6a^* + 0.2c^*$ in LaTe_2 [12].

The off-axis CDW in Sm_2Te_5 is unique among the three compounds studied in that \vec{q}_0 and \vec{q}_1 generate the off-axis higher harmonics $\vec{q}_1 + \vec{q}_0$ and $2\vec{q}_1 + \vec{q}_0$ which are *incommensurate* in the a -direction and *commensurate* in the c -direction. All the other peaks can be expressed in terms of linear combinations of q_0 and q_1 as indicated in Figure 5.2(b), which means that the remaining other peaks are higher harmonics of these two q vectors. Correspondingly, $\vec{q}_0 = (2/3)c^* = 0.667c^*$ and $\vec{q}_1 = 0.521a^*$ are stronger in intensity than the higher harmonics $\vec{q}_1 + \vec{q}_0$ and $2\vec{q}_1 + \vec{q}_0$. A similar higher harmonic CDW structure formed by linear combination of two distinct incommensurate q vectors was also recently found in ErTe_3 by high resolution X-ray diffraction measurements [17].

In contrast to Nd_2Te_5 and Sm_2Te_5 , the off axis CDW in Gd_2Te_5 is fully commensurate in both a^* and c^* . High resolution X-ray diffraction measurements at Stanford Synchrotron Radiation Laboratory(SSRL) [64] confirm that all peaks can be indexed by linear combinations of the two wavevectors $\vec{q}_1 = (5/12)a^* + (1/12)c^*$ and $\vec{q}_2 = (1/12)a^* + (5/12)c^*$, although it is not immediately clear that these are really the two fundamental wavevectors since other linear combinations are also possible in such a fully commensurate satellite peak structure.

5.3 Discussion

5.3.1 Electron-Phonon Coupling, Lindhard susceptibility and CDW Formation

The electronic structure for $R_2\text{Te}_5$ is two dimensional and has minimal dispersion perpendicular to the Te planes(Figure 2.8 (c)). CDW formation can be described by the second quantized Fröhlich Hamiltonian,

$$\begin{aligned}
 H = & \sum_{n,k} \epsilon_k a_{n,k}^\dagger a_{n,k} + \sum_{m,k} \hbar\omega_{m,q} b_{m,k}^\dagger b_{m,k} \\
 & + \sum_{n,m,k,q} g_{n,m,q} a_{n,k+q}^\dagger a_{n,k} (b_{m,-q}^\dagger + b_{m,q})
 \end{aligned} \tag{5.1}$$

where $a_{n,k}^\dagger$ and $b_{m,q}^\dagger$ are the electron creation operator in the n_{th} band, and phonon creation operator in the m_{th} mode respectively [1]. The electron-phonon interaction is tuned by the coupling $g_{n,m,q}$ between the n_{th} electron band and the m_{th} phonon mode and the effect on the lattice distortions can be shown by obtaining the renormalized phonon mode and the dispersion relation from Equation 5.2:

$$\begin{aligned}
\hbar^2 \ddot{Q}_{m,q} &= -[[Q_{m,q}, H], H] \\
\ddot{Q}_{m,q} &\approx -\omega_{m,q}^2 Q_{m,q} - \sum_n g_{n,m,q} \left(\frac{2\omega_{m,q}}{M\hbar} \right)^{1/2} \rho_{n,q} \\
\rho_{n,q} &= -\chi_n(q) \sum_{m'} g_{n,m',q} \left(\frac{2\omega_{m',q}}{M\hbar} \right)^{1/2} Q_{m',q} \\
\ddot{Q}_{m,q} &= -\omega_{m,q}^2 Q_{m,q} \\
&+ \sum_{n,m'} \frac{2g_{n,m,q}g_{n,m',q}(\omega_{m,q}\omega_{m',q})^{1/2}}{M\hbar} \chi_n(q) Q_{m',q}
\end{aligned} \tag{5.2}$$

where $\omega_{m,q}$ and $Q_{m,q}$ refer to the oscillation energy frequency and the Fourier component of the non-interacting normal coordinate of the m_{th} phonon mode respectively and $\rho_{n,q}$ indicates electron density in the n_{th} electron energy band.

The resultant phonon mode softening strongly depends on the strength of $g_{n,m,q}$ and $\chi_n(q)$. While the coupling strength $g_{n,m,q}$ singles out the electron bands and phonon modes relevant to lattice distortions, the distortion wavevectors are selected by the peak structure in $\chi_n(q)$, which is mainly decided by FS nesting:

$$\begin{aligned}
\chi_n(\vec{q}) &= \sum_{n' \in \{n\}} \chi_{nn'}(\vec{q}) + \sum_{n' \notin \{n\}} \chi_{nn'}(\vec{q}) \\
\chi_{nn'}(\vec{q}) &= -\frac{1}{(2\pi)^d} \int_{1BZ} d\vec{k} \frac{f_{n'}(\vec{k} + \vec{q}) - f_n(\vec{k})}{\epsilon_{n',\vec{k}+\vec{q}} - \epsilon_{n,\vec{k}}}
\end{aligned} \tag{5.3}$$

where $f_n(\vec{k})$ and $\epsilon_{n,\vec{k}}$ refer to Fermi-Dirac function and the energy of the electron in n_{th} band.

Although it has never been easy to obtain the exact m, n and q dependence of the coupling strength g theoretically or experimentally, $\chi_n(q)$ is relatively accessible from band structure calculations, and indeed several authors have argued the origin of CDW formation in both RTe_2 and RTe_3 in terms of simple FS nesting conditions using tight binding band calculations [2, 12, 18, 31, 34, 36, 63]. This model was successful in identifying the sections of FS which drives the CDW modulation in these compounds, and the details of the nesting was found to be dependent mainly on the *topology* of the FS at the Fermi level rather than of the whole band structure.

We have used the same approach for R_2Te_5 , calculating the Lindhard susceptibility $\chi(\vec{q})$ of the LMTO band structure illustrated in Figures 2.7(c) and Figure 2.8 (c) in order to examine the origin of the *on-* and *off-axis* CDW super lattices observed for this family of compounds. For computational simplicity, the two dimensional band structure at $k_y=0$ was considered for the summation in the 1st Brillouin zone (Equation 5.3).

However, if we assume an isotropic coupling strength $g_{n,m,q}=g$ and consequently calculate $\chi(\vec{q})$ by summing over all bands including inter single-double layer contributions, this quantity is found to be relatively uninformative. Broad maxima are found centered around $0.5a^*$ and $0.5c^*$ (Figure 5.3(a)), but otherwise there is not a well-developed peak structure that would lead one to anticipate one particular wavevector to be favored over another.

Deeper insight can be gained when more general coupling strength g 's, varying for individual phonon modes and Te layers, are introduced. Motivated by the identification of distinct sections of the FS associated with the single and double Te square planes (Figure 2.8 (c)), we accordingly divide the six $5p$ bands crossing the Fermi level E_F into two relevant subgroups that form ditelluride-like FS sections from single Te

layers, and tritelluride-like FS sections from double Te layers. The contributions to the Lindhard susceptibility from each subgroup, $\chi_S(\vec{q})$ and $\chi_D(\vec{q})$, can be calculated as shown in Equation 5.4, where S, S' and D, D' refer to single and double layers respectively:

$$\begin{aligned}
\chi_{double}(\vec{q}) &= \chi_D(\vec{q}) + \sum_S \chi_{DS}(\vec{q}) \\
\chi_{single}(\vec{q}) &= \chi_S(\vec{q}) + \sum_D \chi_{SD}(\vec{q}) \\
\chi_D(\vec{q}) &= \sum_{DD'} \chi_{DD'}(\vec{q}) \\
\chi_S(\vec{q}) &= \sum_{SS'} \chi_{SS'}(\vec{q})
\end{aligned} \tag{5.4}$$

Results of these calculations are shown in Figures 5.3(b) and (c). Inspection of these figures indicates that $\chi_S(\vec{q})$ and $\chi_D(\vec{q})$ have a more finely peaked structure than the total $\chi(\vec{q})$ (Figure 5.3(a)).

Using this division, and following Equation 5.2, the resulting renormalized phonon mode dispersion is given by:

$$\begin{aligned}
\omega_{ren,m}^2(q) &\approx \omega_{m,q}^2 - \frac{2g_{<D>,m,q}^2 \omega_{m,q}}{M\hbar} \chi_D(\vec{q}) \\
&- \frac{2g_{<S>,m,q}^2 \omega_{m,q}}{M\hbar} \chi_S(\vec{q}) - \frac{2g_{<DS>,m,q}^2 \omega_{m,q}}{M\hbar} \sum_{DS} \chi_{DS}(\vec{q})
\end{aligned} \tag{5.5}$$

This dispersion relation (Equation 5.5) explicitly shows how the phonon mode

softening depends on the average coupling strengths $g_{\langle S \rangle}$, $g_{\langle D \rangle}$ and $g_{\langle SD \rangle}$, and the Lindhard susceptibility contributions $\chi_S(q)$, $\chi_D(q)$ and $\chi_{SD}(q)$, from the single, double and inter single-double layer contributions respectively. This division makes it possible, at least in principle, to identify the relative coupling strength as well as the most relevant electron bands from the observed lattice distortions. In the following two sections, we address the origin of the *on-* and *off-axis* lattice modulation with reference to these contributions.

5.3.2 Origin of the *On-axis* Lattice Modulation

All three compounds exhibit an on-axis lattice modulation with wavevector oriented along either the a^* or c^* axis. As noted in section 5.2, TEM cannot distinguish these two lattice parameters, but high resolution x-ray diffraction experiments for Gd_2Te_5 have determined that q_0 is in fact oriented along the c^* direction for this compound. The orientation of the on-axis wavevector for Nd_2Te_5 and Sm_2Te_5 remains to be determined, but for simplicity we have referred to these as also lying along the c^* direction. The magnitude of the on-axis wavevectors for the three compounds are very similar, being commensurate $q_0=(2/3)c^*=0.667c^*$ for Sm_2Te_5 , with very close incommensurate values for Nd_2Te_5 and Gd_2Te_5 (Table 5.1).

Significantly, the on-axis wavevectors for all three compounds correspond to a very well-defined sharp maximum in $\chi_D(\vec{q})$ calculated from the sections of the FS associated with the double Te layers (Figure 5.3(b)). A substantial fraction of the FS coming from these double layers are nested by this wavevector, as indicated by vertical arrows in Figure 2.8 (c). The actual modulation wavevectors are very close to the maximum in $\chi_D(\vec{q})$, and $\chi_D(\vec{q}_0)$ is smaller by less than 5% compared to the calculated *global* maximum. This striking correspondence is highly suggestive that

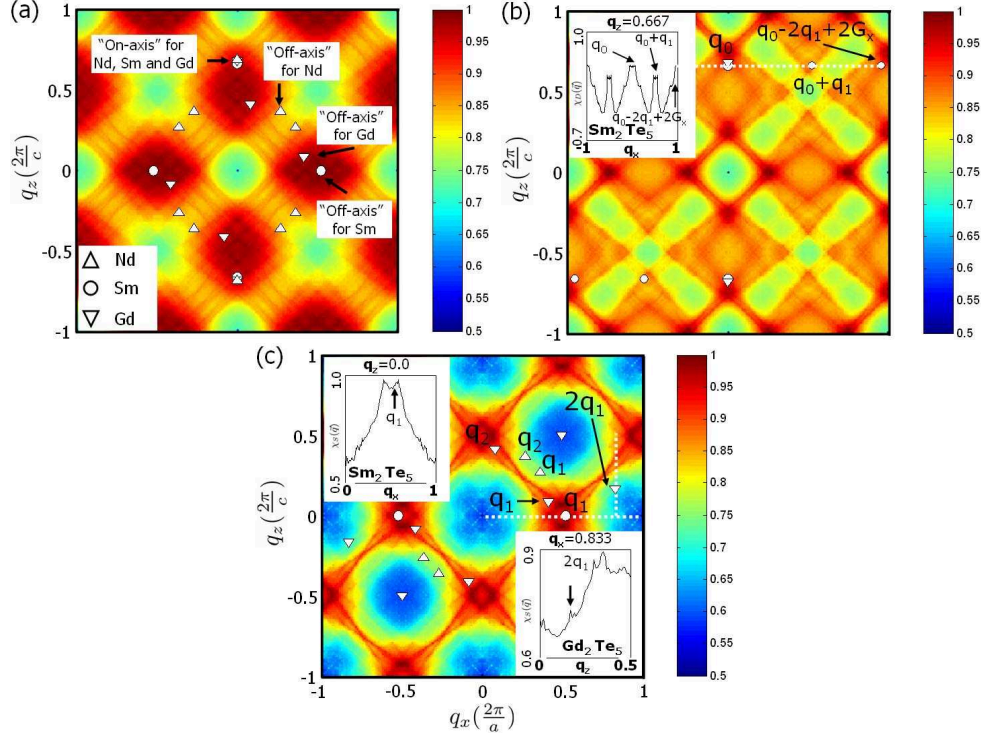


Figure 5.3: Color scale for all panels: red high, blue low. (a) The Lindhard susceptibility $\chi(\vec{q}) = \sum_{nn'} \chi_{nn'}(\vec{q})$ at $q_y=0$, summed for all the bands including inter single-double layer pairs. (b) $\chi_D(\vec{q})$: contribution to $\chi(\vec{q})$ from the double Te layers. *On-axis* wavevectors for all three compounds lie on the *global maximum*. Inset: a line cut following the dashed line, illustrating the resonant enhancement of the mixed harmonics $\vec{q}_0 + \vec{q}_1$ and $\vec{q}_0 - 2\vec{q}_1 + 2\vec{G}_x$ for Sm_2Te_5 . (c) $\chi_S(\vec{q})$: contribution to $\chi(\vec{q})$ from the single Te layers. Symbols represent first harmonics of the *off-axis* modulation vectors for all three compounds, and second harmonics for Gd_2Te_5 . Upper inset: a line cut following the horizontal dashed line. The *off-axis* modulation lies close to the *global maximum* of $\chi_S(\vec{q})$ for Sm_2Te_5 . Lower inset: a line cut following the vertical dashed line, showing the resonant enhancement of the commensurate *off-axis* lattice modulation for Gd_2Te_5 .

the double Te layers drive the *on-axis* CDW.

The simpler double-layer compound $R\text{Te}_3$ also exhibits an on-axis superlattice modulation, also corresponding to a similarly well-defined peak in the susceptibility. In that case, the wavevector $q_0 \sim (5/7)c^* = 0.71c^*$ over the entire range of the compounds ($R=\text{La-Tm}$) [17, 34, 36, 43, 61, 65], which is also very close to q_0 for $R_2\text{Te}_5$. The difference in q_0 values between the two families of compounds can be attributed to differences in band filling, as well as to the more complicated electronic structure in $R_2\text{Te}_5$. Nevertheless, the similarity in the nesting mechanism driving the *on-axis* modulation in the two compounds, and its stability across the rare earth series for both families, is remarkable.

5.3.3 Origin of the *Off-axis* Lattice Modulation

Given the clear correlation between the on-axis modulation wavevectors and $\chi_D(\vec{q})$, it is natural to reason that the off-axis wavevectors might be more closely associated with the single Te planes. Indeed, with the possible exception of Nd_2Te_5 , none of the three compounds studied exhibit any obvious correlation between the off-axis wavevectors and $\chi_D(\vec{q})$, whereas, as we show below, there is a close correlation with $\chi_S(\vec{q})$, at least for Sm_2Te_5 and Gd_2Te_5 . However, the off-axis modulation is not as simple to account for as the on-axis modulation. In particular, there is considerable variation in the off-axis wavevectors for the three compounds studied (Table 5.1), reminiscent of the variation in the lattice modulation for the simpler single-layer compound $R\text{Te}_2$ ($R = \text{La} - \text{Ce}$) [2, 12]. Consequently, we consider each of the three compounds separately below.

First, Sm_2Te_5 . For this compound, the off-axis modulation lies along the a -axis, with an incommensurate wavevector $\vec{q}_1 = 0.521a^* \approx 0.5a^*$ (here we preserve the

notation “*off-axis*” to indicate that \vec{q}_1 is not oriented parallel to \vec{q}_0 , even though, in this case, \vec{q}_1 lies along a high symmetry direction). As can be seen from the inset to Figure 5.3(c), this wavevector lies very near to the *global* maximum in $\chi_S(\vec{q})$, indicating that the single Te layers do indeed play a significant role in driving this off-axis CDW. The behavior is also reminiscent of the unit cell doubling associated with the CDW superlattice found in some of the rare earth ditellurides $R\text{Te}_2$ [2, 12].

As described in section 5.2, Sm_2Te_5 is unique among the three compounds studied in that the mixed harmonics of the CDW modulations $\vec{q}_0 \pm \vec{q}_1$ and $\vec{q}_0 \pm 2\vec{q}_1$ are evident in SADP patterns. Close inspection of the inset to Figure 5.3(b) reveals that these wavevectors, which have a different incommensurate/commensurate structure in the a and c directions, are in fact closely associated with noticeably significant peak structures in $\chi_D(\vec{q})$. The same figure also shows that $\vec{q}_0 - 2\vec{q}_1 + 2\vec{G}_{(100)}$, equivalent to $\vec{q}_0 - 2\vec{q}_1$, is actually very near to another global maximum in $\chi_D(\vec{q})$ adjacent to (101). This maximum is equivalent to that which is close to \vec{q}_0 by a simple reciprocal lattice translation, suggestive of a resonance in the interaction due to the crystal symmetry:

$$\begin{aligned} & \frac{2g_{\langle D \rangle, m, \vec{q}=\vec{q}_0-2\vec{q}_1}^2 \omega_{m, \vec{q}=\vec{q}_0-2\vec{q}_1}}{M\hbar} \chi_D(\vec{q}_0 - 2\vec{q}_1) \\ = & \frac{2g_{\langle D \rangle, m, \vec{q}=\vec{q}_0-2\vec{q}_1}^2 \omega_{m, \vec{q}=\vec{q}_0-2\vec{q}_1}}{M\hbar} \chi_D(\vec{q}_0 - 2\vec{q}_1 + 2\vec{G}_{(100)}), \\ & \chi_D(\vec{q}_0 - 2\vec{q}_1 + 2\vec{G}_{(100)}) \approx \chi_D(\vec{q}_0) \end{aligned} \quad (5.6)$$

These observations suggest a significant coupling between the two wavevectors \vec{q}_0 and \vec{q}_1 in Sm_2Te_5 . Even though the off-axis modulation is principally driven by the single Te-planes (i.e. \vec{q}_1 is very close to the global maximum in $\chi_S(\vec{q})$) nevertheless, it is not insensitive to the double layers. In contrast, the on- and off-axis CDW

modulations in Nd_2Te_5 and Gd_2Te_5 seem to be independent or minimally coupled to each other, without any commensurate/incommensurate mixing.

In contrast to Sm_2Te_5 , the off-axis CDW in Gd_2Te_5 is fully commensurate. Although the modulation wavevectors \vec{q}_1 and \vec{q}_2 for Gd_2Te_5 are different to that observed in Sm_2Te_5 , both lie close to global maxima in $\chi_S(\vec{q})$, suggesting that the single Te planes play the dominant role in driving the off-axis CDW for this compound, too. It is worth noting, however, that the peak structure in $\chi_S(\vec{q})$ (Figure 5.3(c)) is far less well developed than that in $\chi_D(\vec{q})$ (Figure 5.3(b)). Rather than a single *global* maximum with little in the way of additional features, $\chi_S(\vec{q})$ exhibits a broad range of maxima along sharp “ridges” (dark red regions in Figure 5.3(c)) connecting four relatively sharp local peaks centered close to $\vec{q}=(0\ 0\ 0.5), (0.5\ 0\ 0), (-0.5\ 0\ 0)$ and $(0\ 0\ -0.5)$. The resulting figure is reminiscent of similar calculations for the simpler single layer compound RTe_2 , which also lack a well-defined single peak, and for which the superlattice modulation vectors also vary across the rare earth series [12]. We will return to the variation in the off axis wavevectors later.

The two commensurate CDW vectors, \vec{q}_1 and \vec{q}_2 , in Gd_2Te_5 span the entire commensurate CDW super lattice peaks in \vec{k} space. Such an extensive commensurate modulation structure may not allow a simple explanation in terms of perturbative higher harmonics. However, it is interesting to note that $2\vec{q}_1$, a second harmonic of \vec{q}_1 , lies exactly on top of an additional weak local maximum in $\chi_S(\vec{q})$, which may give some hint as to the origin of this extensive commensurate structure (inset to Figure 5.3(c)-the strength of this feature depends sensitively on details of the calculation, but appears to be robust). Specifically, rather than just a simple perturbation of \vec{q}_1 , $2\vec{q}_1$ itself also seems to be directly coupled to the relevant electronic structure through the *local maximum peak* at $\chi_S(2\vec{q}_1)$. This effect coherently enhances the

CDW instabilities at $\vec{q}=2\vec{q}_1$ and seems to help the commensuration mechanism of the off-axis CDW to extend to higher n harmonics or integral multiple of \vec{q}_1 , while it is, in contrast, weakly or minimally coupled to the on-axis CDW leaving that incommensurate. This behavior is in distinct contrast to that of the other two compounds studied, neither of which exhibits higher harmonics of the off-axis modulation vectors. By way of comparison with Sm_2Te_5 , it is also worth noting that the off-axis CDW peaks in Gd_2Te_5 lie in a high but flat region, without any sharp peak features, when mapped onto $\chi_D(\vec{q})$ of the ditelluride-like double Te layers. As such, and in contrast to the case of Sm_2Te_5 , the off-axis CDW wavevectors observed in Gd_2Te_5 appear to get enhanced mainly within the Te single layer by this subtle interaction and develop an extensive commensurate CDW structure.

Although the off-axis lattice modulation is different for Sm_2Te_5 and Gd_2Te_5 , and although they each exhibit different resonant mechanisms which enhance the off-axis CDW based on interaction with the double or single Te planes respectively, nevertheless, the off-axis CDW for both compounds appears to be principally driven by the single Te planes. In sharp contrast, Nd_2Te_5 appears to defy this simple model. Specifically, the off-axis modulation wavevectors for this compound do not lie close to the global maximum in $\chi_S(\vec{q})$ (triangular points in Figure 5.3(c)). Instead, they are found near *local* maxima which have values about 20% less than the *global* maximum in both $\chi_S(\vec{q})$ and $\chi_D(\vec{q})$, although these features are very weak. Taken at face value, it appears that both single and double planes contribute towards the off-axis CDW in Nd_2Te_5 , although it is impossible from this analysis to determine whether one or the other plays a dominant role.

One of the principle defining features of the off-axis lattice modulation is the huge variation between the three compounds studied, especially given the minimal

differences observed in the on-axis wavevector. Given that the electronic structure is essentially identical for all three compounds, this large variation suggests that differences in the phonon mode characteristics play an important role. The atomic masses of Nd, Sm and Gd differ by up to 10%, affecting the lattice instability through Equation 5.5. Presumably, the very well-defined peak feature in $\chi_D(\vec{q})$ (Figure 5.3(b)) ensures that the on-axis wavevector remains tied to the wavevector at which this quantity peaks, even as the phonon modes and electron-phonon coupling change. However, the more poorly defined maximum in $\chi_S(\vec{q})$ (Figure 5.3(c)) is apparently not strong enough to completely dominate the electron-phonon coupling to the extent that variation in the phonon characteristics are able to affect the lattice modulation. This behavior is consistent with that of the single and double layer compounds RTe_2 and RTe_3 - the former having a poorly defined peak in $\chi(\vec{q})$ and a lattice modulation very sensitive to changes in rare earth [12], the latter having a very well-defined peak in $\chi(\vec{q})$ [26], and a lattice modulation that hardly changes across the entire rare earth series [17, 34, 36, 61, 65].

5.4 Conclusion

In summary, we have presented an alternative method to prepare large, high-quality single crystals of $R_2\text{Te}_5$ ($R=\text{Nd}$, Sm and Gd) via a binary self flux method, and have presented the first evidence for charge density wave formation in this material. All three compounds exhibit an *on-axis* modulation with $\vec{q}_0 \approx 0.68c^*$, in combination with an *off-axis* superlattice which varies significantly between the three compounds studied. Based on a consideration of contributions to the Lindhard susceptibility from the single and double Te planes of the layered structure, it appears that the on-axis CDW is driven by the double Te planes, whereas the off-axis CDW is principally driven by the single Te planes. Resonant effects associated with coupling of higher harmonics of these modulation wavevectors to local features in the susceptibility of the double and single Te planes appear to be relevant for Sm_2Te_5 and Gd_2Te_5 respectively, stabilizing in the first case mixed commensurate/incommensurate off-axis harmonics, and in the second an extensive commensurate structure associated with just the single Te layers, decoupled from the on-axis modulation.

Chapter 6

Multiple charge density wave transitions in Gd_2Te_5

Diffraction measurements performed via transmission electron microscopy and high resolution X-ray scattering reveal two distinct charge density wave transitions in Gd_2Te_5 at $T_{c1} = 410(3)$ and $T_{c2} = 532(3)$ K, associated with the *on*-axis incommensurate lattice modulation and *off*-axis commensurate lattice modulation respectively. Analysis of the temperature dependence of the order parameters indicates a non-vanishing coupling between these two distinct CDW states. These results appear in Ref. [14]

6.1 Introduction

The basic premise in CDW formation is that a large electronic susceptibility at finite wavevector q , such as can be generated by Fermi surface nesting in low dimensional materials, can lead to a coupled electronic/lattice instability if the electron-phonon

coupling is strong enough. In the previous chapter and Ref. [66], the family of compounds $R_2\text{Te}_5$ have been shown to host CDW modulations and the analysis indicated that CDWs originated independently on the single and double Te planes, driven by separate contributions to the susceptibility. This material raises the very interesting question of how CDW formation on the different Te planes coexists, or even competes.

The study in this chapter aims at furthering the understanding of the thermodynamic properties of the CDW states via Transmission Electron Microscopy (TEM) and high resolution x-ray diffraction at the elevated temperatures. The measurements were performed on Gd_2Te_5 single crystals, which have a particularly interesting distortion structure with ‘incommensurate’ and ‘commensurate’ CDWs, independently formed on and off the c^* axis respectively [13]. By probing the CDW satellite peaks in the broader regions of the reciprocal lattice space, we establish that the two sets of CDW wave vectors observed in Gd_2Te_5 , one of which is incommensurate ($q_0 \sim 0.69c^*$), and the other of which is fully commensurate ($q_1 = 5/12a^* + 1/12c^*$, $q_2 = 1/12a^* + 5/12c^*$), do indeed undergo separate CDW transitions, but that the two CDW condensates are not completely independent.

6.2 Experimental Results

6.2.1 Transmission Electron Microscopy at High Temperatures

TEM diffraction images were taken at various temperatures along the (010) zone axis, i.e. perpendicular to the Te planes. Selected area diffraction patterns (SADPs) were taken using a Philips CM 30 up to 540K, utilizing double copper washers to improve thermal contact. The equipment was optimized at the nominal camera length 900

mm and images were taken at varied exposure stops to obtain enough sensitivity for the weak superlattice reflections.

SADPs taken at room temperature both before and after heating to 536 K are shown in Figure 6.1, where the CDW wave vectors q_0 , q_1 and q_2 are labeled around $(h0l)=(101)$. Figure 6.1(a) shows that the initial diffraction pattern before heating is actually a mirror image of the satellite peaks previously observed in Figure 5.2 (c) and Ref. [13] and we label the diffraction peaks accordingly $q'_1 = -5/12a^* + 1/12c^*$ and $q'_2 = -1/12a^* + 5/12c^*$. After heating and subsequent cooling to room temperature (Figure 6.1(b)), the diffraction pattern shows weak circular streaks, caused by irreversible surface recrystallization at high temperatures. The diffraction pattern has also suffered a mirror reflection about the c^* axis, ascribed to a reversal of the CDW domain orientation.

Representative SADPs taken at 343 K, 446 K and 536 K are shown in Figure 6.2 in a sequential order of temperature changes. Both domains of the commensurate CDW (i.e. q_1 and q_2 oriented to the right and to the left) were observed for temperatures above 313K (see for example Figure 6.2 (a)). Compared to the commensurate *off*-axis CDW peaks, the incommensurate CDW along the c^* axis did not show a similar effect, due to the inequivalence of the a and c axes.

The diffraction intensities for q_0 were tremendously reduced by 343 K (green arrows in Figure 6.2 (a)) and had disappeared by 446 K (Figure 6.2 (b)). The transition temperature for the incommensurate CDW, therefore, seems to lie between these temperature ranges, while the commensurate *off*-axis CDW still remained with strong intensities. In contrast, the intensities for the *off*-axis CDW remained strong until much higher temperatures, eventually almost vanishing at the highest temperatures (536 K, Figure 6.2 (c)).

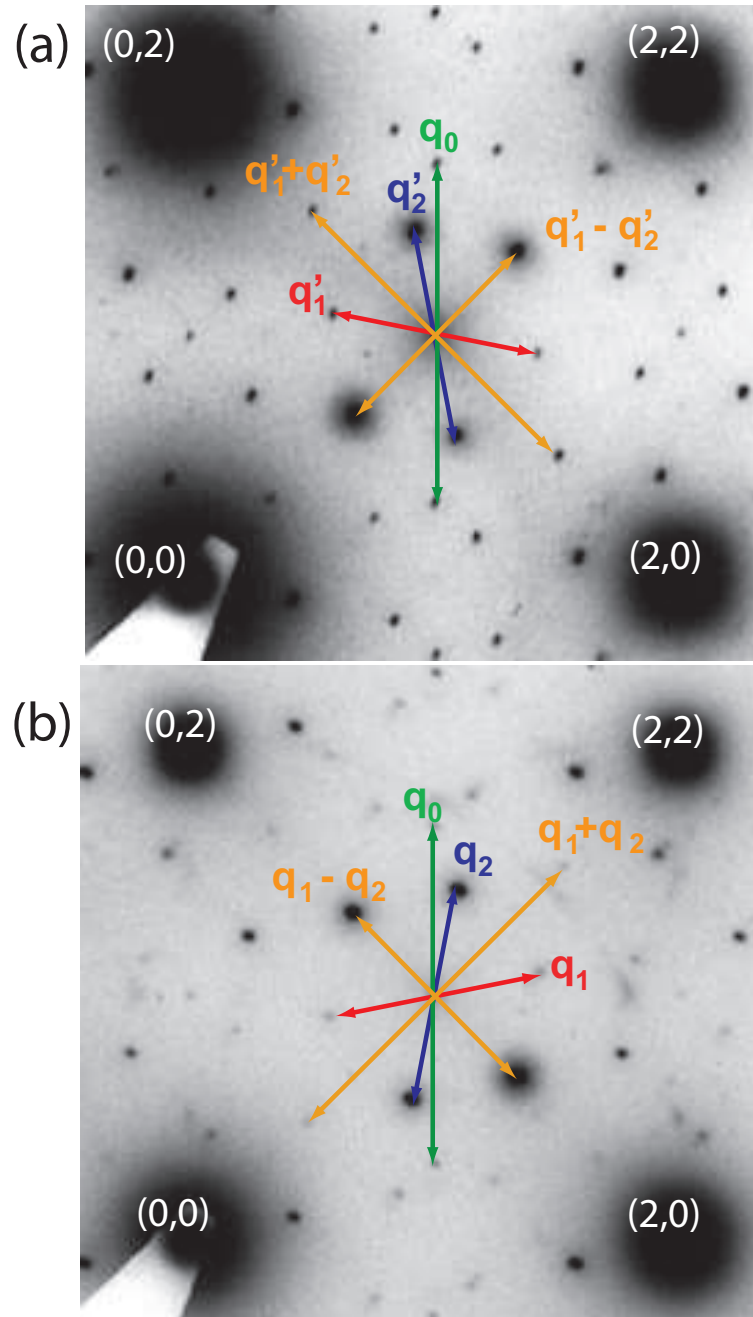


Figure 6.1: (a) Selected area TEM diffraction pattern in $(h0l)$ plane at room temperature (a) before and (b) after heating to 536K and subsequently cooling to room temperature. CDW wavevectors are labeled following our initial convention described in Chapter 4 and Ref. [13]. Before heating, the *off-axis* CDW vectors were initially $q'_1 = -5/12a^* + 1/12c^*$ and $q'_2 = -1/12a^* + 5/12c^*$. After heating, they have changed to $q_1 = 5/12a^* + 1/12c^*$ and $q_2 = 1/12a^* + 5/12c^*$.

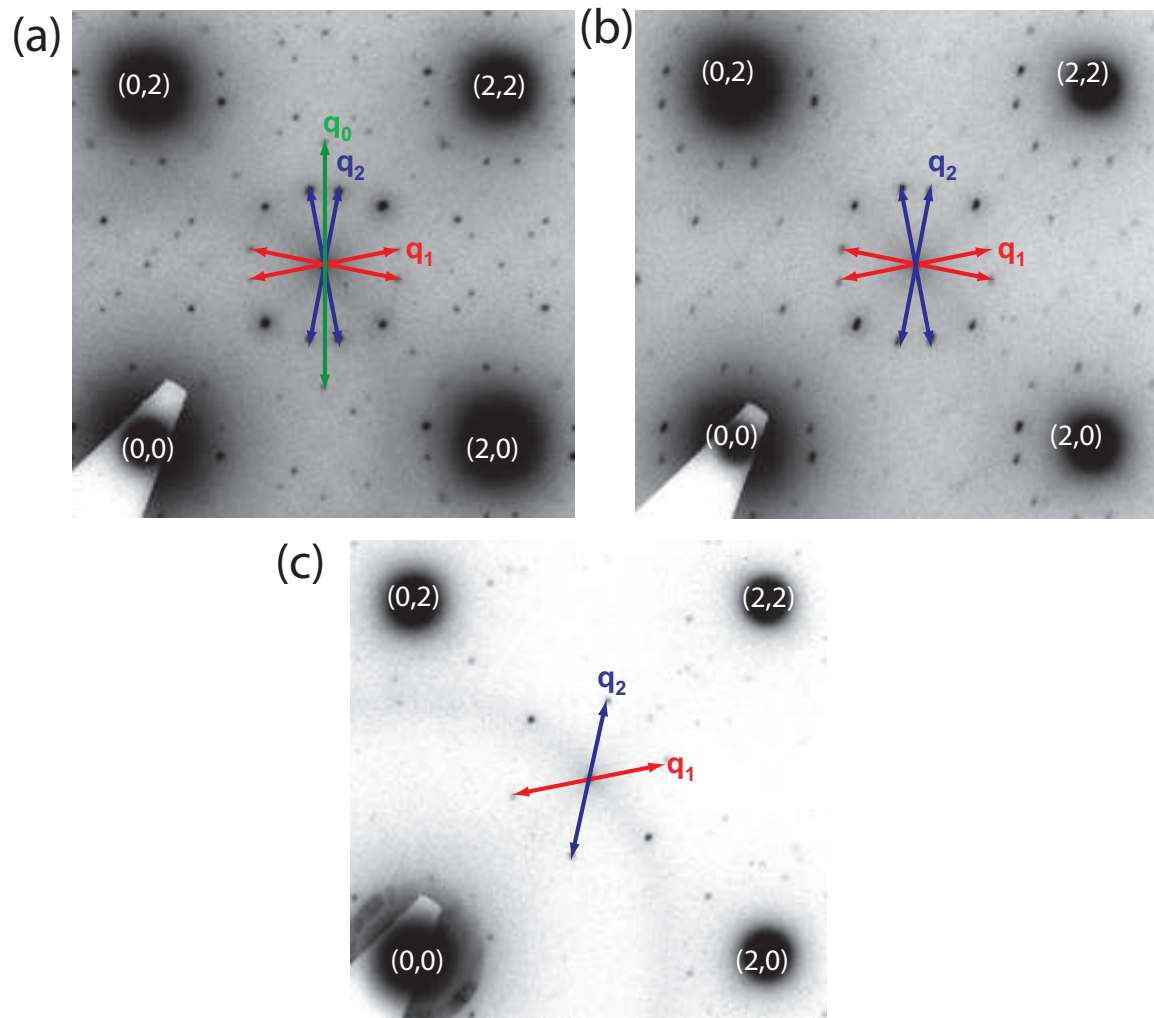


Figure 6.2: SADPs at (a) 343 K (b) 446 K and (c) 536 K. Wave vectors are labeled as described in the main text. The incommensurate CDW with $q_0 \sim 0.69 c^*$ has disappeared by 446 K, suggestive of a CDW transition below this temperature.

6.2.2 High Resolution X-ray Diffraction at High Temperatures

The CDW transitions were investigated in greater detail via high resolution x-ray diffraction. CDW peaks are sharply peaked (inset to Figure 6.3 (a)) and from the full width at half maximum (FWHM), we obtain a lower bound for the CDW correlation length of $\sim 0.5\mu\text{m}$ in the ac plane and $\sim 0.05\mu\text{m}$ along the b -axis for both *on*- and *off*-axis CDWs at 300 K (Figure C.1 in Appendix C).

The temperature dependence of the incommensurate CDW peaks for $(hkl)=(3\ 38\ 1-q_0)$, $(5\ 38\ 1-q_0)$ and $(4\ 39\ q_0)$ is shown in Figure 6.3. A rapid increase in FWHM above the resolution limit (shown in Figure 6.3 (a) for the specific peak $(4\ 39\ q_0)$ in the ac plane) signals a CDW transition at $T_{c1} = 410(3)$ K, consistent with TEM data described above.¹

The square root of the integrated intensity, proportional to the order parameter for weakly coupled systems, is shown in Figure 6.3 (b) for all three peaks, together with the mean field BCS curve drawn for $T_{c1} = 410$ K. Data have been normalized to the BCS curve at 300 K. Residual scattering intensity above T_{c1} , ascribed to fluctuations due to the large FWHM we observe, was observed up to 463 K, above which the satellite peaks became too broad to be distinguished from background.

The absolute value of q_0 changes with temperature, increasing by approximately 1.5% from T_{c1} to room temperature (Figure 6.3(c)), and indicating a fully incommensurate CDW. Above T_{c1} , q_0 does not appear to vary as strongly with temperature, but the accuracy of the measurement was limited by the significant broadening of the CDW peak.

¹In comparison, the correlation length in the closely related compound TbTe_3 was measured to be $1.8\mu\text{m}$ and $0.5\mu\text{m}$ in and perpendicular to the basal plane respectively. The increase in the FWHM above T_c was also observed for TbTe_3 [17].

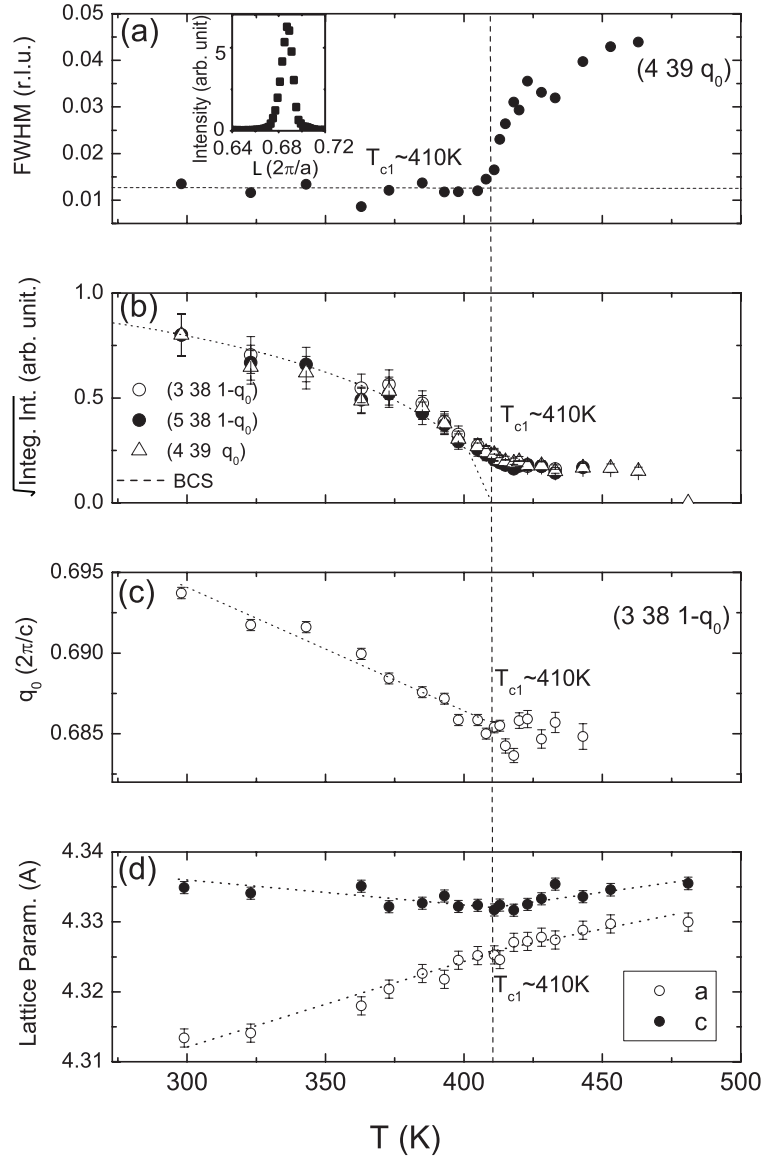


Figure 6.3: Temperature dependence of the *on*-axis incommensurate CDW state. (a) FWHM of the CDW peak at $(4\ 39\ q_0)$ in the *ac* plane. Inset shows *L* scan at 300 K. The sudden increase in FWHM at $T_{c1} = 410(3)$ K indicates a CDW phase transition. (b) Square root of the integrated intensity for peaks at $(3\ 38\ 1-q_0)$, $(5\ 38\ 1-q_0)$ and $(4\ 39\ q_0)$, normalized to the BCS curve at 300 K. (c) CDW wave vector q_0 as a function of temperature measured from the CDW peak at $(3\ 38\ 1-q_0)$. (d) In-plane lattice parameters *a* and *c* as a function of temperature. The dashed vertical line for all panels indicates the nominal transition temperature $T_{c1} = 410$ K.

The CDW transition is also apparent in the lattice parameters (Figure 6.3(d)). Above T_{c1} , there is only a small difference (approximately 0.15%) in the in-plane lattice parameters a and c . On cooling below T_{c1} , there is a marked change in the thermal expansion coefficients, with the a -axis lattice parameter decreasing more rapidly with reducing temperature, while the c -axis lattice parameter actually increases with reducing temperature, at least in the range from 410 down to 300 K. By room temperature, the c -axis lattice parameter is fully 0.60% larger than the a -axis. A similar “stretching” of the c -axis upon CDW formation was also observed for the unidirectional incommensurate CDW in TbTe_3 [17].

The temperature dependence of the *off*-axis commensurate CDW diffraction peaks was also measured. Data were collected for many peaks and representative measurements for five specific wavevectors are shown in Figure 6.4. The diffraction intensities for $(4\frac{1}{12} \ 41 \ \frac{5}{12})$, $(3\frac{8}{12} \ 41 \ \frac{4}{12})$, $(4\frac{5}{12} \ 44 \ \frac{1}{12})$ and $(3\frac{3}{12} \ 39 \ \frac{3}{12})$ decreased upon heating and almost disappeared at 533K (Figure 6.4 (a)). Oxidation at these elevated temperatures, even in the flowing He atmosphere, meant that data had to be collected rapidly. Consequently, measurements of the FWHM were limited to temperatures below 533 K and, in contrast to the *on*-axis CDW described above, it was difficult to systematically determine a sharp increase of the peak width associated with the ultimate CDW transition. However, comparison of the temperature dependence of the square roots of the integrated intensities of $(4\frac{1}{12} \ 41 \ \frac{5}{12})$ and $(3\frac{8}{12} \ 41 \ \frac{4}{12})$ and the 4th roots of the integrated intensities of $(4\frac{5}{12} \ 44 \ \frac{1}{12})$ and $(3\frac{3}{12} \ 39 \ \frac{3}{12})$ with the classical BCS order parameter (Figure 6.4 (b)) allows an estimate of $T_{c2} = 532(3)$ K for these peaks, in reasonable agreement with the trend observed in TEM.

Inspection of the data in Figures 6.4 (a) and (b) indicates that the intensity of these commensurate superlattice reflections might be slightly affected at the onset

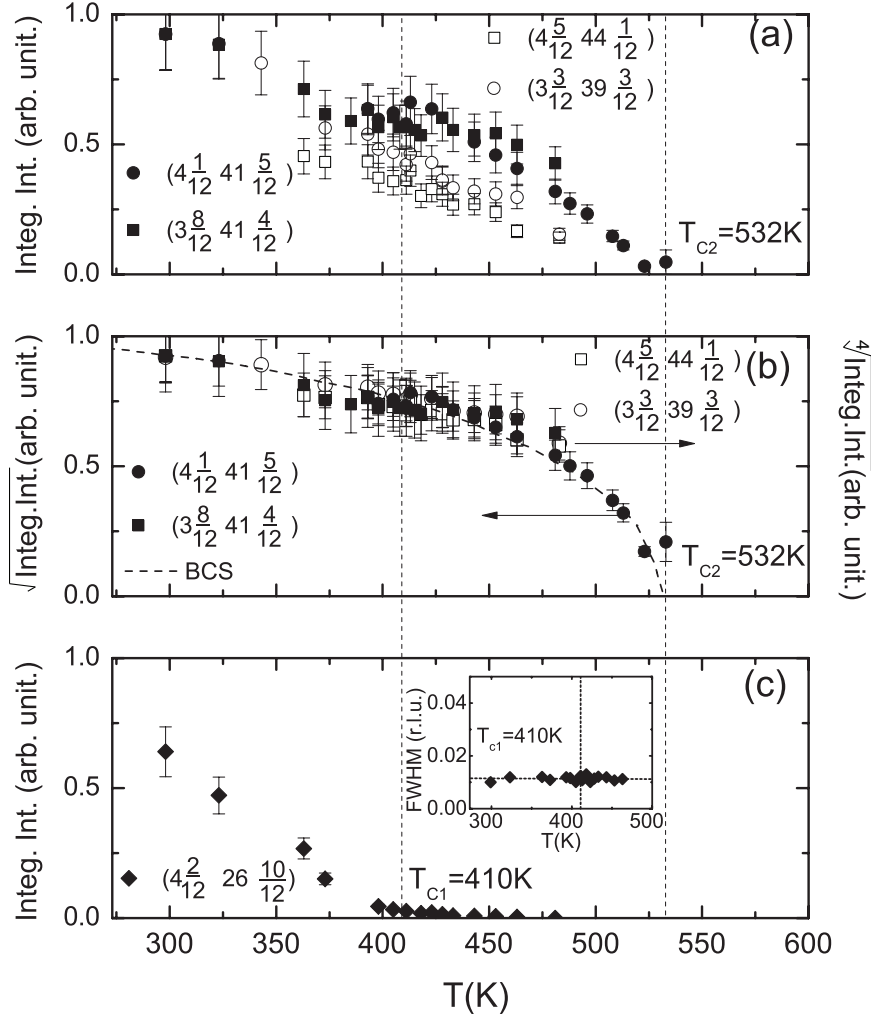


Figure 6.4: Temperature dependence of the *off*-axis commensurate CDW state. (a) Integrated intensities of CDW peaks at $(4 \frac{1}{12}, 41 \frac{5}{12})$, $(3 \frac{8}{12}, 41 \frac{4}{12})$, $(4 \frac{5}{12}, 44 \frac{1}{12})$ and $(3 \frac{3}{12}, 39 \frac{3}{12})$. (b) Square roots of the integrated intensities of $(4 \frac{1}{12}, 41 \frac{5}{12})$ and $(3 \frac{8}{12}, 41 \frac{4}{12})$ (left axis) and 4th roots of the integrated intensities of $(4 \frac{5}{12}, 44 \frac{1}{12})$ and $(3 \frac{3}{12}, 39 \frac{3}{12})$ (right axis). (c) Integrated intensity of the CDW peak at $(4 \frac{2}{12}, 26 \frac{10}{12})$. Inset shows FWHM of the CDW peak at $(4 \frac{2}{12}, 26 \frac{10}{12})$ in the *ac* plane. The intensity decreases significantly at $T \sim T_{c1}$, suggestive of interaction between the *on*- and *off*-axis CDWs. The BCS order parameter is shown by a dashed line in panel (b), and vertical dashed lines indicate $T_{c1} = 410$ K and $T_{c2} = 532$ K.

of the incommensurate *on*-axis CDW at T_{c1} , but this effect is clearly at the limit of our resolution for these peaks. However, other commensurate CDW peaks exhibit a stronger effect. For example, the strongest suppression of the reflections for the commensurate superlattice at T_{c1} occurred for the CDW peak at $(4\frac{2}{12} \ 26\frac{10}{12})$, where the intensity was suppressed almost to zero without increase in the FWHM up to much higher temperatures.

6.3 Discussion

SADP measurements on Gd_2Te_5 single crystals were effective in providing qualitative visual representations of overall diffraction patterns near the (010) zone axis. Figures 6.1 and 6.2 successfully demonstrated that diffraction patterns from *on*- and *off*-axis CDWs vary, in fact, distinctively with temperature and two symmetric mirror image patterns of the *off*-axis CDWs even coexist above room temperature. Defects in a crystal such as twinning or stacking disorder can generate additional peaks. However, in the case of Gd_2Te_5 , the SADPs for the *on*-axis CDW did not develop any additional peaks along the perpendicular axis above room temperature.² Furthermore, TEM measurements were performed in a microscopic length scale on the regions carefully selected without such defects and, hence, the mirror image pattern is likely to originate from purely thermodynamic effects associated with CDW formation, rather than from crystallographic defects. The mirror image patterns have an equivalent symmetry relative to the underlying lattice and seem to thermodynamically compete with each other when the temperature is reduced.

X-ray diffraction data for the satellite peaks gave quantitative estimates of transition temperatures at $T_{c1}=410\text{K}$ and $T_{c2}=532\text{K}$ for the *on*-axis and *off*-axis CDWs

²This can be attributed to the inequivalence of the *a* and *c* axes in the *Cmcm* crystal structure.

respectively. The *on*-axis CDW from the Te double layers can be compared with the CDW in $TbTe_3$ in Ref. [17]. The divergence of FWHM at $T_{c1}=410K$ and the agreement with BCS curve for the *on*-axis CDW (Figure 6.3) are quite similar to the second order phase transition in $TbTe_3$, where the CDW is in the weak coupling BCS limit. However, the change of the modulation vector $\Delta q_0 \sim 0.010(\text{r.l.u.})$ between the room temperature and T_{c1} is significantly large in Gd_2Te_5 .³

In addition, the thermal expansion for Gd_2Te_5 can be compared quantitatively with $TbTe_3$ by using the fractional differences of the lattice parameters a and c . As shown in Figure 6.3 (d), the lattice parameter was actually contracted along the c -axis when heated from 300K to $T_{c1}=410K$, and it began to expand only after the CDW disappeared above $T_{c1}=410$ K. The fractional difference $(c-a)/\frac{1}{2}(c+a)$ was 0.35% at $0.9T_{c1}$ and 0.15% at T_{c1} respectively for Gd_2Te_5 , while it was 0.13% at $0.9T_{CDW}$ and 0.06% at T_{CDW} for $TbTe_3$, where $T_{CDW}=332.8$ K [17]. Hence, the *on*-axis CDW formation also seems to stretch the crystal lattice along the c axis below T_{c1} and this is a substantially stronger effect compared to $TbTe_3$.

The order parameter for the first and second harmonic diffraction is proportional to the square and the 4th root of the integrated intensity respectively [17,67], although contributions from non-sinusoidal modulations, if they exist, might not be ignored in some cases. The second harmonic diffraction peaks were observed in the tritellurides at the wavevectors given by the linear combination of the first harmonics, $q' = 2q$ for $TbTe_3$ and $q_1 + q_2$ for $ErTe_3$ [17]. In contrast, it is not trivial to discern the first or higher harmonic contributions in the *off*-axis CDW diffraction pattern for Gd_2Te_5 due to the extensive ‘commensurate’ structure, but the order parameter can be used to have some insights. The *off*-axis CDW peaks remained up to $T_{c2}=533K$ (Figure

³ $\Delta q < 0.002(\text{r.l.u.})$ between the room temperature and T_{CDW} in $TbTe_3$.

6.4 (a)). The comparison of the temperature dependence of the square roots and the 4th roots of the integrated intensities with the classical BCS order parameter in Figure 6.4 (b) implies that the satellite peaks at $(4\frac{1}{12} \ 41 \ \frac{5}{12})$ and $(3\frac{8}{12} \ 41 \ \frac{4}{12})$, corresponding to q_2 and q_2-q_1 respectively are from the fundamental, whereas peaks at $(4\frac{5}{12} \ 44 \ \frac{1}{12})$, corresponding to q_1 and $(3\frac{3}{12} \ 39 \ \frac{3}{12})$, corresponding to q_2-2q_1 are second harmonics, and hence that the fundamental wavevectors associated with the *off*-axis CDW are actually $q_2 = \frac{1}{12}a^* + \frac{5}{12}c^*$ and $q_2-q_1 = -\frac{4}{12}a^* + \frac{4}{12}c^*$. This assignation might be consistent with the relative intensities of the superlattice peaks seen in Figure 6.1, but it is still not clear that this is the ‘only’ interpretation for such a fully commensurate lattice modulation.

In addition, the suppression of the commensurate CDW peak for $(4\frac{2}{12} \ 26 \ \frac{10}{12})$ near $T_{c1}=410\text{K}$ (Figure 6.4(c)) is distinctive and suggests that the existence of the *on*-axis CDW significantly affects the *off*-axis CDW states, although they are independently formed in single and double Te layers respectively. In contrast to the incommensurate CDW peaks, the suppression of this satellite reflection at and above T_{c1} happened without peak broadening due to the fluctuations and, hence, the peak remained coherent, indicating the absence of an actual phase transition associated with this specific wavevector (Figure 6.4(c) and the inset therein). This behavior could not be accounted for by any order of harmonic generation, and suggests a non-trivial coupling of the commensurate and incommensurate CDW order parameters. It will require further experiments to elucidate the nature of this coupling, and the extent to which it affects the underlying electronic structure.

6.4 Conclusion

In summary, we have established that the *on*-axis incommensurate and *off*-axis commensurate lattice modulations in Gd_2Te_5 have different CDW transitions.

Diffraction measurements showed that the phase transitions seem to be similar to the second order phase transition in $TbTe_3$ [17], although Gd_2Te_5 has two successive transitions at $T_{c1}=410(3)K$ and $T_{c2}=532(3)K$ for the *on*-axis and *off*-axis CDWs respectively. Comparison of the temperature dependence of the peak intensities with the BCS curve indicates that the superlattice peaks from the *off*-axis CDWs mostly come from either first or second harmonics of diffraction, while the significant reduction in intensity for an *off*-axis CDW peak at $(4\frac{2}{12} \ 26 \ \frac{10}{12})$ at $T_{c1}=410K$ strongly suggests a non-trivial coupling between *on*- and *off*-axis CDWs.

Chapter 7

Conclusion

Although the $R\text{Te}_2$ and $R\text{Te}_3$ have been known to host charge density waves for several years [2,36,47], systematic experimental studies on the CDWs in these materials have been a big challenge, particularly in $R\text{Te}_2$ and $R_2\text{Te}_5$, mainly due to the difficulties in controlling the Te deficiencies ($R\text{Te}_{2-\delta}$) and even in the growth of the single crystals itself ($R_2\text{Te}_5$). In this thesis, the results of experimental studies of CDW formation were presented for representative members of these two rare earth telluride families, $R\text{Te}_2$ ($R=\text{La}, \text{Ce}$) and $R_2\text{Te}_5$ ($R=\text{Nd}, \text{Sm}, \text{Gd}$) prepared with an alternative self flux technique, and it was shown that the CDWs in these materials are driven by Fermi surface nesting and instabilities in the electronic structure.

While the differences in electronic structures could be understood quite simply in terms of different band fillings in the Te p orbitals, details of CDW formation in each family of the rare earth tellurides demonstrated a wide variety of features. CDW superlattice diffraction patterns in $\text{LaTe}_{1.95}$ and $\text{CeTe}_{2.00}$ discussed in this thesis have shown very distinct *off*-axis patterns with four fold symmetry, which were not previously perceived in crystals produced by different techniques. In contrast, although the

CDW patterns remained robust for many samples of $\text{LaTe}_{1.95}$ and $\text{CeTe}_{2.00}$, resistivity data were rather sensitive to the sample-to-sample variation, presumably due to the tiny change in the Te vacancy which is beyond the experimental resolution. ARPES measurements also revealed that the sections of the Fermi surfaces are gapped inhomogeneously and distinct spectroscopy results can be compared between the crystals with different Te deficiencies in $\text{LaTe}_{2-\delta}$ [12, 57]. As such, in the case of $R\text{Te}_{2-\delta}$, the variation in Te deficiency δ seem to affect the CDW formation by changing band fillings and charge carrier concentration in the CDW state.

The CDWs in $R_2\text{Te}_5$ were also observed for the first time in single crystals of Nd_2Te_5 , Sm_2Te_5 and Gd_2Te_5 via transmission electron microscopy(TEM) and high resolution X-ray diffraction. The family of $R_2\text{Te}_5$ has an extended crystal structure with alternating single and double Te layers and CDWs in these materials exhibited more complicated multiple wavevectors on and off the c^* axis. The *on*-axis CDW has a lattice modulation $q_0 \sim (2/3)c^*$ for each compound, which is similar in magnitude to that of the tritellurides ($q \sim (5/7)c^*$), while the *off*-axis CDWs were seen to vary significantly between these three compounds.

Consideration of the band structure contribution to the Lindhard susceptibility $\chi(q)$, was very useful in identifying the origin of the CDWs in each family of compounds. Our calculations show that E_F is closer to the top of the conduction bands in $R\text{Te}_{2-\delta}$ and, thus, $\chi(q)$ has broad peak with somewhat poorly defined nesting wavevectors, while $R\text{Te}_3$ has a very well developed sharp peak in $\chi(q)$. It implies that the CDWs in $R\text{Te}_{2-\delta}$ are rather sensitive to the perturbations, for example from tellurium vacancies and small changes of the Fermi level. In addition, the family of $R_2\text{Te}_5$ was found to have several sheets of Fermi surface, being essentially a composite

of those found in $R\text{Te}_2$ and $R\text{Te}_3$. Separate contributions to the Lindhard susceptibility arising from the double and single Te planes can, to a large extent, be associated with the observed *on*- and *off*-axis lattice modulations respectively.

The diffraction intensities of the CDW satellite peaks in Gd_2Te_5 were investigated using high resolution X-ray diffraction and TEM as a function of temperature and it was seen that Gd_2Te_5 has two successive transitions at $T_{c1}=410(3)\text{K}$ and $T_{c2}=532(3)\text{K}$ for the *on*-axis incommensurate and *off*-axis commensurate CDWs respectively. The CDW transitions are very similar to the second order phase transition previously observed for TbTe_3 [17]. The observation of two distinct CDW transitions in this compound supports the hypothesis that the *on*- and *off*-axis CDWs have separate origins. In addition, the temperature dependence of the peak intensities compared with the classical BCS curve indicates that the superlattice peaks from the *off*-axis CDWs mostly come from either first or second harmonics of diffraction. Furthermore, the anomaly in temperature dependence of intensities for *off*-axis CDW peaks and a significant intensity reduction particularly for the peak at $(4\frac{2}{12} \ 26\frac{10}{12})$ at the onset of the *on*-axis CDW transition strongly suggests that the *on*- and *off*-axis CDWs are not totally independent and there exists a non-trivial coupling between the CDWs formed separately in the single and double Te layers.

The very rich “tunability” of the system attracted the extensive research interest on the families of $R\text{Te}_2$ and $R\text{Te}_3$. The family of $R_2\text{Te}_5$ was successfully added as a new CDW model system by my research work and there is still ample room for exciting future investigations, in particular probing the interplay between the *on*- and *off*-axis CDW states in this material. It remains to be seen whether a similar set of systematic trends associated with CDW formation as the rare earth ion is varied will be found in this more complex material as have previously been observed in

$R\text{Te}_3$, but the work described in this thesis provides a suitable framework in which to understand the qualitative features.

Appendix A

Magnetic properties of $R_2\text{Te}_5$

In our discussion of CDW formation in $R_2\text{Te}_5$, we have restricted the role played by the rare earth ions to that of their size (i.e. chemical pressure courtesy of the lanthanide contraction) and mass (i.e. effect on phonon frequencies). We can safely neglect the magnetic properties of these ions since, as we show below, the magnetic ordering transitions occur several orders of magnitude lower in temperature than the CDW transitions.

Complementary measurements of magnetic properties were performed down to 1.8 K using the Quantum Design MPMS SQUID magnetometer for magnetic property measurements and PPMS for specific heat measurements. Antiferromagnetic ordering was observed below 10 K for each of the compounds and the values of the Néel temperature T_N were obtained from heat capacity measurements (Figure A.1). The Néel temperatures for $R_2\text{Te}_5$ ($R=\text{Nd, Sm, Gd}$) are plotted against the de Gennes factor, $(g_J - 1)^2 J(J + 1)$ in Figure A.2, where g_J is the Landé-g factor. Unfortunately, since La_2Te_5 does not form, at least according to the published binary alloy phase diagram [37], the lattice contribution to the specific heat could not be separately

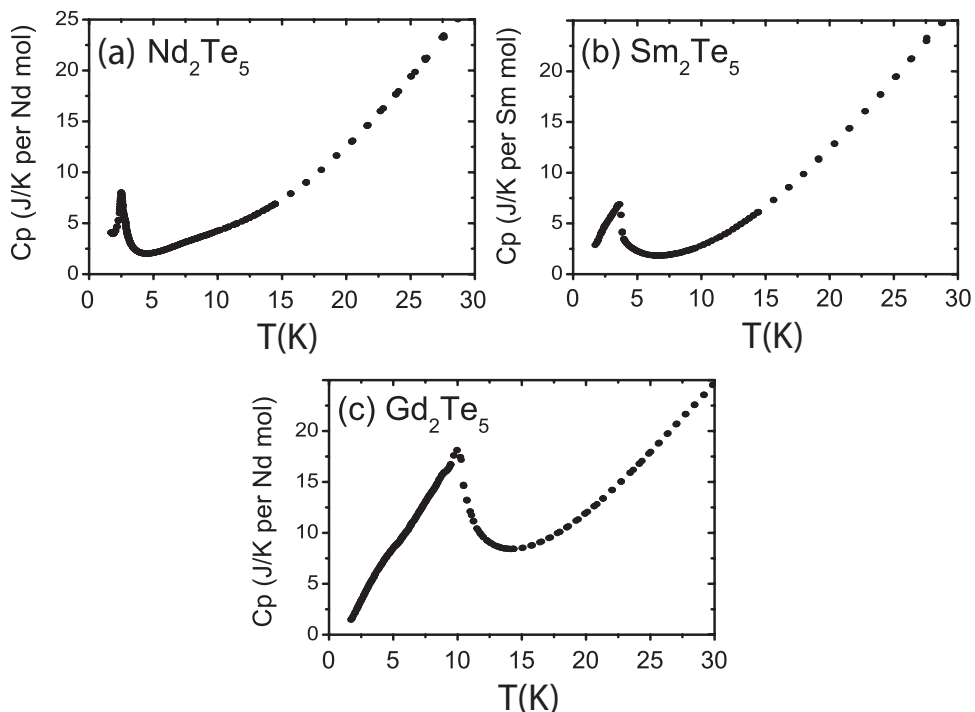


Figure A.1: Specific heat for (a) Nd_2Te_5 (b) Sm_2Te_5 and (c) Gd_2Te_5 for temperatures below 30 K, showing the Néel transitions associated with antiferromagnetic ordering of the local rare earth moments at temperatures below 10 K.

determined and consequently the magnetic contribution to the entropy could not be estimated.

The magnetization and the inverse of susceptibility for Nd_2Te_5 and Gd_2Te_5 were measured in an applied magnetic field of 1000 Oe and representative results for temperatures below room temperature down to 1.8 K are shown in Figure A.3. In the measurement, magnetic fields were oriented either parallel or perpendicular to the b -axis direction. Figure A.3 (b) illustrates an anisotropic magnetization for Nd_2Te_5 with an easy axis along the b -direction. The anisotropy in Nd_2Te_5 can be attributed to the crystal field effect (CEF) splitting of the Hund's rule ground state, while Gd_2Te_5 does not have the same effect since $L=0$ for Gd.

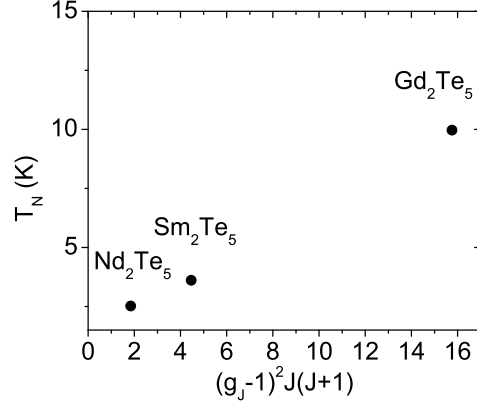


Figure A.2: The Néel temperatures plotted against the de Gennes factor $(g_J - 1)^2 J(J + 1)$. $T_N = 2.52$ K for Nd_2Te_5 , 3.62 K for Sm_2Te_5 and 9.97 K for Gd_2Te_5 .

R	θ^{\parallel}	θ^{\perp}	p_{eff}^{\parallel}	p_{eff}^{\perp}	$p_{R^{3+}}$
Nd	-11.10	-23.57	3.87	3.81	3.62
Gd	-17.05	-13.48	8.03	7.97	7.94

Table A.1: Magnetic properties for Nd_2Te_5 and Gd_2Te_5 . θ and p_{eff} are obtained from the linear fit to the Curie-Weiss model for magnetic fields applied parallel (θ^{\parallel} and p_{eff}^{\parallel}) and perpendicular (θ^{\perp} and p_{eff}^{\perp}) to the b -axis. Values of $p_{R^{3+}} = (g_J - 1)^2 J(J + 1)$ for isolated Nd^{3+} and Gd^{3+} ions are also listed.

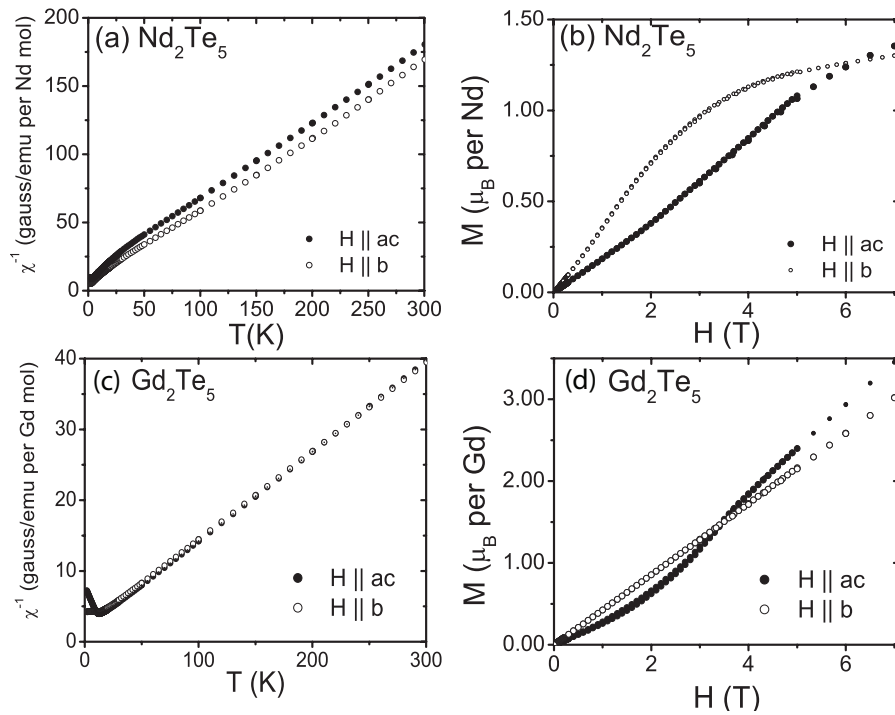


Figure A.3: Susceptibility and magnetization for Nd_2Te_5 (panels (a) and (b) respectively) and Gd_2Te_5 (panels (c) and (d) respectively). The susceptibility, shown as $1/\chi$, was measured in an applied field of 1000 Oe. The magnetization was measured at 1.8 K.

The Weiss temperature and the effective moments were calculated from a linear fit above $T=40$ K and are listed in Table A.1. As anticipated, the experimental estimates of p_{eff}^{\parallel} and p_{eff}^{\perp} are very close to the theoretical estimate of $p_{R^{3+}}$ for isolated Nd^{3+} and Gd^{3+} ions.

Appendix B

Transport property of $R_2\text{Te}_5$

Previous resistivity measurements of $R\text{Te}_3$ clearly indicate the various CDW transitions observed in that family of compounds. The higher CDW transitions in $R_2\text{Te}_5$ preclude the use of resistivity measurements to determine the transition temperatures, at least using the equipment available to our laboratory at the time of writing. Nevertheless, preliminary measurements yield evidence for a CDW transition in Gd_2Te_5 slightly above 400 K, consistent with diffraction data, and, perhaps more strikingly, incoherent transport for currents aligned along the b -axis.

Resistivities for Gd_2Te_5 and Nd_2Te_5 were measured up to 400K and 300K respectively for currents perpendicular and parallel to the b -axis(i.e. in and out of the Te plane) and the representative data are exhibited in Figure B.1 (the measurement was performed in the Quantum Design MPMS system and the temperature range was limited by the experimental setup).

Figure B.1 shows that both compounds are metallic below 200K, consistent with a partially gapped FS. Nd_2Te_5 has a stronger anisotropy (ρ_b/ρ_{ac} is ~ 400 for Nd_2Te_5

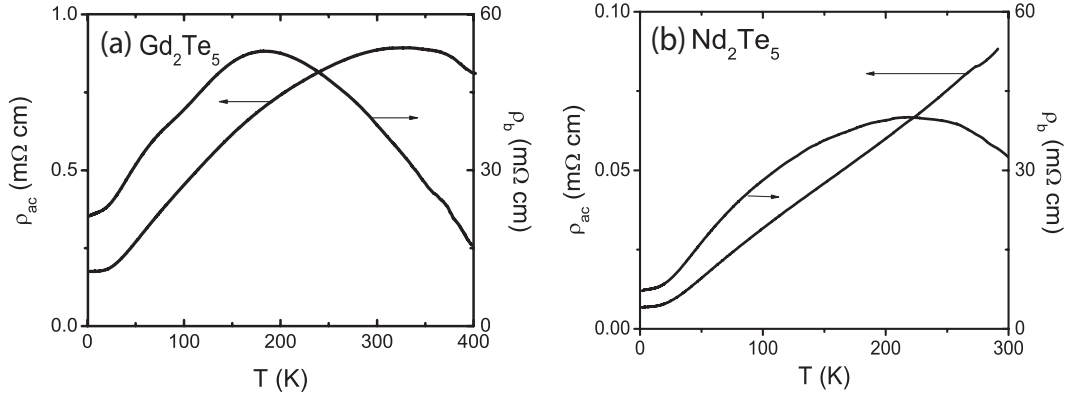


Figure B.1: Resistivity data for (a) Gd_2Te_5 and (b) Nd_2Te_5 .

and ~ 50 for Gd_2Te_5), which might be due to the very different superlattice modulations observed in these two materials affecting the geometry of their respective reconstructed FSs. The in-plane resistivity ρ_{ac} clearly shows that Nd_2Te_5 is metallic up to 300 K, while ρ_{ac} for Gd_2Te_5 changes slope by 300 K and there is an anomaly above 350 K. It was observed that such an anomaly in the resistivity data is associated with the CDW transition in the family of rare earth tritellurides above room temperature [17]. Although the data of ρ_{ac} presented in Figure B.1 (a) does not show this effect enough to clarify the CDW transition in Gd_2Te_5 , mainly due to the experimental temperature limits, the phase transition for the incommensurate CDW in Gd_2Te_5 was, indeed, identified at $T_{c1}=410\text{K}$ in the transmission electron microscopy and the high resolution X-ray diffraction experiments (Chapter 6). Future resistivity experiments to slightly higher temperatures should clarify the origin of this feature in the in-plane resistivity. Ref. [17] also illustrated that the lighter rare earth tritelluride compounds have a higher CDW transition temperature and the absence of the slope change in ρ_{ac} for Nd_2Te_5 seems to be consistent with this trend.

Meanwhile, the out-of-plane resistivity ρ_b is metallic at low temperature, but a

saturation occurs at ~ 170 K for Gd_2Te_5 and at ~ 210 K for Nd_2Te_5 . $d\rho_b/dT < 0$ indicates that the crossover to incoherent conduction occurs at these temperatures. Although we cannot calculate a mean free path, the large value of the b -axis resistivity above these temperatures indicates that above these temperatures, the mean free path l along the b -direction must be less than the distance d between the planes (The Mott-Ioffe-Regel Limit).

Appendix C

X-ray Diffraction for Gd_2Te_5 at room temperature

Extensive X-ray diffraction measurements at room temperature revealed a series of trends associated with the superlattice diffraction peaks. Although these data are insufficient to provide information about atomic displacements, they are included here in order to assist with future experimental crystallographic studies.

Firstly, the lower bound on the correlation length of the CDW states can be obtained from the FWHM and the room temperature data for the commensurate CDW peaks near the Bragg peaks at $(0k\bar{2})$ and $(\bar{2}k\bar{2})$ are shown in Figure C.1.¹ The large error bars in the estimates for some peaks are mainly due to the mosaic structure. The lower bounds of the CDW correlation length ξ were approximately estimated to be $0.5\mu\text{m}$ in the ac plane and $0.05\mu\text{m}$ along the b -axis in most of the peaks. It suggests that the strong CDW correlation extends more than 1000 unit cells in the ac plane, while the CDW condensates are weakly correlated along the layer

¹Neglecting the instrumental response, the approximation to the correlation length ξ is given by π/FWHM . This value provides a lower bound on the actual correlation length.

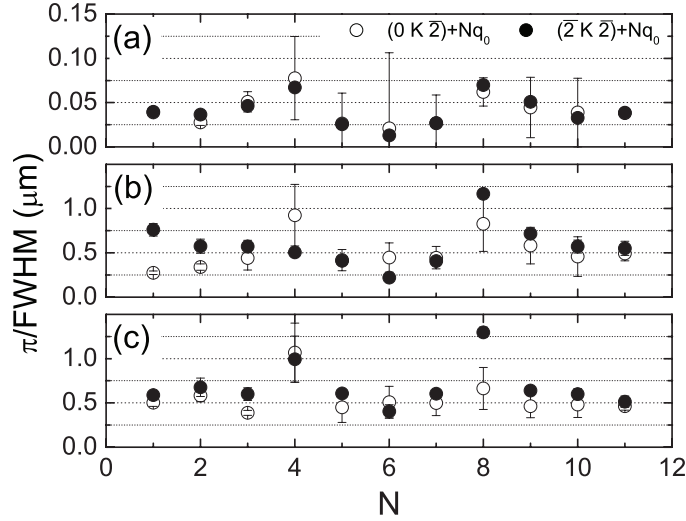


Figure C.1: π/FWHM from (a) K scans (b) L scans and (c) H scans for the CDW peaks near the Bragg peaks at $(0k\bar{2})$ and $(\bar{2}k\bar{2})$. Data provide lower bounds on the actual correlation length ξ for each commensurate CDW peak. $q_0 = \frac{5}{12}a^* + \frac{1}{12}c^*$

stacking direction, extending only upto 10 unit cells. In comparison, the correlation length along the b direction in $TbTe_3$ is $0.5\mu m$ [17] and much longer than that of Gd_2Te_5 . This is somewhat expected from the elongated crystal structure along the b -axis in Gd_2Te_5 .

In addition to the correlation length, the raw data of K scans for the commensurate CDW peaks at $(2\frac{5}{12}K\frac{1}{12})$ and $(1\frac{3}{12}K\frac{3}{12})$ and for the incommensurate CDW peaks at $(1K1-q_0)$ and $(2K0+q_0)$ are shown in Figure C.2. CDW peaks at $(2\frac{5}{12}K\frac{1}{12})$ and $(1K1-q_0)$ are present for even k values, while the intensities for other two peaks are shown to exist only for odd k values. Extensive data collected for other satellite peaks showed that each CDW satellite peak exists only for either *even* or *odd* k values in the K scan. It is quite similar to the extinction condition of the Bragg peaks, which are present at (hkl) for either $k=\text{even}$ or $k=\text{odd}$ along the b^* direction when $k \neq 0$, and Figure C.3 represents a schematic diagram of the k dependence of such conditions for

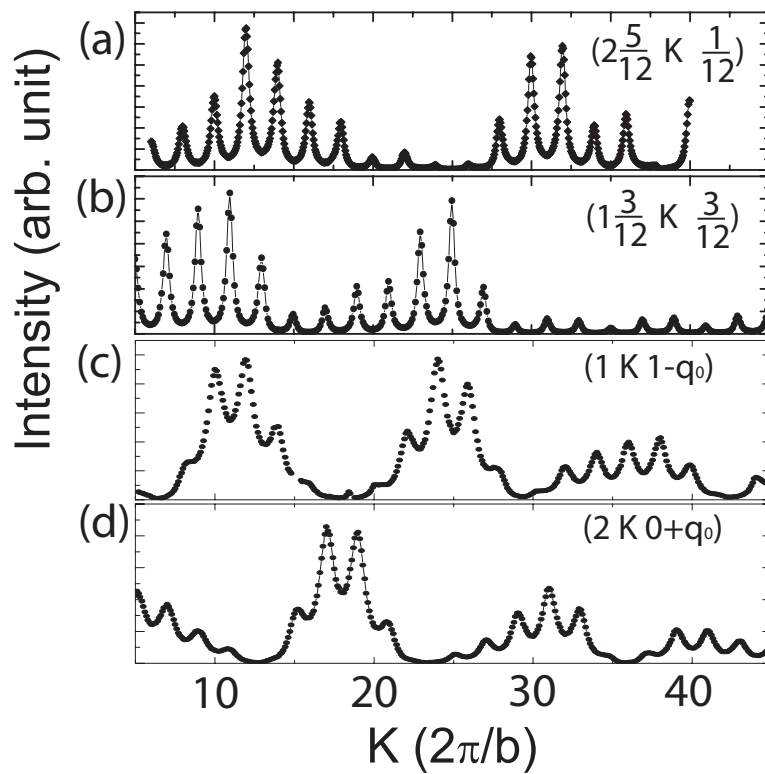


Figure C.2: K scan data at room temperature for the commensurate CDW peaks at (a) $(2 \frac{5}{12} K \frac{1}{12})$ and (b) $(1 \frac{3}{12} K \frac{3}{12})$ and for the incommensurate CDW peaks at (c) $(1 k 1-q_0)$ and (d) $(2 k 0+q_0)$ are shown for $k = 5 \sim 45$. $q_0 \sim 0.69c^*$.

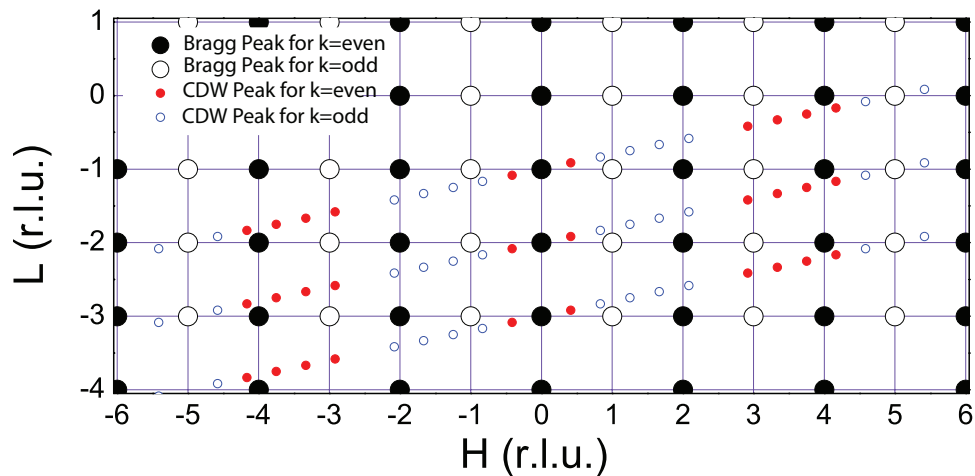


Figure C.3: Schematic diagram of the k dependence of the extinction condition for the Bragg peaks and the commensurate CDW peaks in the $(h l)$ plane. \bullet and \circ marks indicate the diffraction peaks present for $k = \text{even}$ and $k = \text{odd}$ respectively.

the *off*-axis CDWs and the Bragg peaks in the $(h l)$ plane.

The CDW diffraction intensity has a beating envelope along the b^* -axis with a periodicity of $\Delta k \sim 14$. The intensity beating for the incommensurate CDWs has envelopes alternating out of phase by $\Delta k \sim 7$ (Figure C.2 (c) and (d)) and it seems to be associated with the extinction condition of the Bragg peaks close to each of the incommensurate CDW peak.

Bibliography

- [1] G. Grüner, *Density waves in solids*, Perseus publishing, 1994.
- [2] E. DiMasi, B. Foran, M. C. Aronson, and S. Lee, Phys. Rev. B **54**, 13 587 (1996).
- [3] A. Sacchetti, L. Degiorgi, T. Giamarchi, N. Ru, and I. Fisher, Phys. Rev. B **74**, 125115 (2006).
- [4] A. Sacchetti, E. Arcangeletti, A. Perucchi, L. Baldassarre, P. Postorino, S. Lupi, N. Ru, I. Fisher, and L. Degiorgi, Phys. Rev. Lett. **98**, 026401 (2007).
- [5] F. Pfuner, L. Degiorgi, K. Shin, and I. Fisher, Eur. Phys. J. B **63**, 11–16 (2008).
- [6] P. Brüesch, S. Strässler, and H. R. Zeller, Phys. Rev. B **12**(1), 219 (1975).
- [7] L. Degiorgi, B. Alavi, G. Mihály, and G. Grüner, Phys. Rev. B **44**(15), 7808–7819 (Oct 1991).
- [8] L. Degiorgi, S. Thieme, B. Alavi, G. Grüner, R. H. McKenzie, K. Kim, and F. Levy, Phys. Rev. B **52**(8), 5603–5610 (Aug 1995).
- [9] J. McCarten, D. A. DiCarlo, M. P. Maher, T. L. Adelman, and R. E. Thorne, Phys. Rev. B **46**(8), 4456–4482 (1992).

-
- [10] A. Schwartz, M. Dressel, B. Alavi, A. Blank, S. Dubois, G. Grüner, B. P. Gorshunov, A. A. Volkov, G. V. Kozlov, S. Thieme, L. Degiorgi, and F. Lévy, *Phys. Rev. B* **52**(8), 5643 (1995).
- [11] W. Fogle and J. H. Perlstein, *Phys. Rev. B* **6**(4), 1402 (1972).
- [12] K. Y. Shin, V. Brouet, N. Ru, Z. X. Shen, and I. R. Fisher, *Phys. Rev. B* **72**, 085132 (2005).
- [13] K. Y. Shin, J. Laverock, Y. Wu, C. Condrón, M. Toney, S. Dugdale, M. Kramer, and I. Fisher, *Phys. Rev. B* **77**, 165101 (2008).
- [14] K. Y. Shin, N. Ru, C. L. Condrón, Y. Q. Wu, M. J. Kramer, M. F. Toney, and I. R. Fisher, *cond-matt arXiv:0808.2106v1* (2008).
- [15] M. Lavagnini, A. Sacchetti, L. Degiorgi, E. Arcangeletti, L. Baldassarre, P. Postorino, S. Lupi, A. Perucchi, K. Shin, and I. Fisher, *Phys. Rev. B* **77**, 165132 (2008).
- [16] M. Lavagnini, A. Sacchetti, L. Degiorgi, K. Shin, and I. Fisher, *Phys. Rev. B* **75**, 205113 (2007).
- [17] N. Ru, C. L. Condrón, G. Y. Margulis, K. Y. Shin, J. Laverock, S. B. Dugdale, M. F. Toney, and I. R. Fisher, *Phys. Rev. B* **77**, 035114 (2008).
- [18] V. Brouet, W. L. Yang, X. J. Zhou, Z. Hussain, N. Ru, K. Y. Shin, I. R. Fisher, and Z. X. Shen, *Phys. Rev. Lett.* **93**, 126405–1 (2004).
- [19] H. Frölich, *Proc. Roy. Soc. London Ser.* **A223**, 296 (1954).
- [20] R. Peierls, *Quantum Theory of Solids*, Oxford University Press, New York, 1955.

-
- [21] C. Battaglia, H. Cercellier, F. Clerc, L. Despont, M. Garnier, C. Koitzsch, P. Aebi, H. Berger, L. Forro, and C. Ambrosch-Draxl, *Phys. Rev. B* **72**, 195114 (2005).
- [22] M. Bovet, S. van Smaalen, H. Berger, R. Gaal, L. Forró, L. Schlapbach, and P. Aebi, *Phys. Rev. B* **67**, 125105 (2003).
- [23] E. Sola, A. Polls, and F. Mazzanti, *J. Low Temp. Phys.* **127**(112), 29–49 (2002).
- [24] R. A. Christian and H. Hartmut, *Phys. Rev. Lett.* **90**, 116403–1 (2003).
- [25] N. Ru and I. R. Fisher, *Phys. Rev. B* **73**, 033101 (2006).
- [26] M. D. Johannes and I. I. Mazin, *Phys. Rev. B* **77**, 165135 (2008).
- [27] M. H. Whangbo, E. Canadell, P. Foury, and J. P. Pouget, *Science* **252**, 96 (1991).
- [28] B. Norling and H. Steinfink, *Inorg. Chem.* **5**, 1488 (1966).
- [29] H. Yao, J. A. Robertson, E.-A. Kim, and S. A. Kivelson, *Phys. Rev. B* **74**, 245126 (2006).
- [30] A. Kikuchi, *J. Phys. Soc. Jpn* **67**, 1308 (1998).
- [31] J. Laverock, S. B. Dugdale, Z. Major, M. A. Alam, N. Ru, I. R. Fisher, G. Santi, and E. Bruno, *Phys. Rev. B* **71**, 085114 (2005).
- [32] B. Barbiellini, S. B. Dugdale, and T. Jarlbog, *Comput. Mater. Sci.* **28**, 287 (2003).
- [33] G.-H. Gweon, J. D. Denlinger, J. A. Clack, J. W. Allen, C. G. Olson, E. DiMasi, M. C. Aronson, B. Foran, and S. Lee, *Phys. Rev. Lett.* **81**, 886 (1998).

-
- [34] E. DiMasi, M. C. Aronson, J. F. Mansfield, B. Foran, and S. Lee, *Phys. Rev. B* **52**, 14 516 (1995).
- [35] K. Y. Shin, (unpublished).
- [36] E. DiMasi, B. Foran, M. C. Aronson, and S. Lee, *Chem. Mater.* **6**, 1867–1874 (1994).
- [37] T. B. Massalski, editor, *Binary Alloy Phase Diagrams*, ASM International, 1996.
- [38] B. Foran, S. Lee, and M. C. Aronson, *Chem. Mater.* **5**, 974–978 (1993).
- [39] S. M. Park, S. J. Park, and S. J. Kim, *J. Solid State Chem.* **140**, 300 (1998).
- [40] E. Bucher, K. Andres, F. di Salvo, J. Maita, A. Gossard, A. Cooper, and G. Hull Jr., *Phys. Rev. B* **11**(1), 500–513 (1975).
- [41] N. Ru, R. A. Borzi, A. Rost, A. P. Mackenzie, J. Laverock, S. B. Dugdale, and I. R. Fisher, *Phys. Rev. B* **78**, 045123 (2008).
- [42] V. Brouet, W. L. Yang, X. J. Zhou, Z. Hussain, R. G. Moore, R. He, D. H. Lu, Z. X. Shen, J. Laverock, S. B. Dugdale, N. Ru, and I. R. Fisher, *Phys. Rev. B* **77**, 235104 (2008).
- [43] A. Fang, N. Ru, I. Fisher, and A. Kapitulnik, *Phys. Rev. Lett.* **99**, 046401 (2007).
- [44] P. Canfield and Z. Fisk, *Philosophical Magazine B* **65**(6) (1992).
- [45] K. Stowe, *J. Solid State Chem.* **149**, 155–166 (2000).
- [46] K. Stowe, *J. Alloys and Compounds* **307**, 101–110 (2000).

- [47] M.-H. Jung, B.-H. Min, Y.-S. Kwon, I. Oguro, F. Iga, T. Fujita, T. Ekino, T. Kasuya, and T. Takabatake, *J. Phys. Soc. Jpn* **69**, 937–944 (2000).
- [48] Y. S. Kwon and B. H. Min, *Physica B* **281 & 282**, 120–121 (2000).
- [49] B. H. Min, H. Y. Choi, and Y. S. Kwon, *Physica B* **312 & 313**, 203–204 (2002).
- [50] Z. Fisk and J. Remeika, *Handbook on the Physics and Chemistry of Rare Earths, vol 12. Chapter 81. Growth of single crystals from molten metal fluxes*, North-Holland, 1989.
- [51] M. H. Jung, A. Alsmadi, H. C. Kim, Y. Bang, K. H. Ahn, K. Umeo, A. H. Lacerda, H. Nakotte, H. C. Ri, and T. Takabatake, *Phys. Rev. B* **67**, 212504 (2003).
- [52] M. H. Jung, T. Ekino, Y. S. Kwon, and T. Takabatake, *Phys. Rev. B* **63**, 035101 (2000).
- [53] B. H. Min, E. D. Moon, H. J. Im, S. O. Hong, Y. S. Kwon, D. L. Kim, and H.-C. Ri, *Physica B* **312 & 313**, 205–207 (2002).
- [54] J.-S. Kang, C. G. Olson, Y. S. Kwon, S. W. Han, K. H. Kim, A. Sekiyama, S. Kasai, S. Suga, and B. I. Min, *J. Phys.:Condens. Matter* **16**, 9163–9168 (2004).
- [55] M. H. Jung, K. Umeo, T. Fujita, and T. Takabatake, *Phys. Rev. B* **62**, 11 609 (2000).
- [56] J. H. Shim, J.-S. Kang, and B. I. Min, *Phys. Rev. Lett.* **93**, 156406 (2004).
- [57] D. R. Garcia, G. H. Gweon, S. Y. Zhou, C. M. Graf, M. H. Jung, Y. S. Kwon, and A. Lanzara, *Phys. Rev. Lett.* **98**, 166403 (2007).

-
- [58] B. H. Min, J. H. Cho, H. J. Lee, C. W. Han, D. L. Kim, and Y. S. Kwon, *Physica B* **281 & 282**, 118–119 (2000).
- [59] Y. Iyeiri, T. Okumura, C. Michioka, and K. Suzuki, *Phys. Rev. B* **67**, 144417 (2003).
- [60] S. B. Dugdale, private communication, 2005.
- [61] C. Malliakas and M. Kanatzidis, *J. Am. Chem. Soc.* **128**, 12612 (2006).
- [62] ICDD PDF Number: 04-004-1155.
- [63] E. DiMasi, M. C. Aronson, B. Foran, and S. Lee, *Physica B* **206 & 207**, 386–388 (1995).
- [64] K. Y. Shin, N. Ru, C. L. Condron, M. F. Toney, and I. R. Fisher, 2007.
- [65] C. Malliakas, S. Billinge, H. Kim, and M. Kanatzidis, *J. Am. Chem. Soc.* **127**, 6510 (2005).
- [66] C. D. Malliakas, M. Iavarone, J. Fedor, and M. G. Kanatzidis, *J. Am. Chem. Soc.* **130**, 3310 (2008).
- [67] A. Guinier, editor, *X-Ray Diffraction: In Crystals, Imperfect Crystals, and Amorphous Bodies*, Dover Publications, Inc., New York, 1994.